

Unquenched Meson Spectroscopy

Susana Patrícia Simões Coito

Supervisor: Doctor Georges Rupp

Co-Supervisor: Doctor Everardus Johannes Hubertus van Beveren

Thesis approved in public session to obtain the PhD Degree in Physics

Jury final classification: Pass with Merit

Jury

Chairperson: Chairman of the IST Scientific Board

Members of the Committee:

Doctor Brigitte Anabelle Vaz de Abreu Hiller

Doctor Alex Heinz Ladislaus Blin

Doctor Maria Paula Frazão Bordalo e Sá

Doctor Everardus Johannes Hubertus van Beveren

Doctor Georges Rupp

Doctor Pedro José de Almeida Bicudo

2013

Unquenched Meson Spectroscopy

Susana Patrícia Simões Coito

Supervisor: Doctor Georges Rupp

Co-Supervisor: Doctor Everardus Johannes Hubertus van Beveren

Thesis approved in public session to obtain the PhD Degree in Physics

Jury final classification: Pass with Merit

Jury

Chairperson: Chairman of the IST Scientific Board

Members of the Committee:

Doctor Brigitte Anabelle Vaz de Abreu Hiller, Investigadora Coordenadora (com Agregação) da Universidade de Coimbra

Doctor Alex Heinz Ladislaus Blin, Investigador Coordenador (com Agregação) da Universidade de Coimbra

Doctor Maria Paula Frazão Bordalo e Sá, Professora Associada (com Agregação) do Instituto Superior Técnico, da Universidade de Lisboa

Doctor Everardus Johannes Hubertus van Beveren, Professor Associado, Faculdade de Ciências e Tecnologia, da Universidade de Coimbra

Doctor Georges Rupp, Investigador Principal, Centro de Física das Interações Fundamentais do Instituto Superior Técnico, da Universidade de Lisboa

Doctor Pedro José de Almeida Bicudo, Professor Auxiliar (com Agregação) Instituto Superior Técnico, da Universidade de Lisboa

Funding Institutions

Fundação para a Ciência e Tecnologia
Centro de Física das Interações Fundamentais

2013

Preface

In October 2007, fifteen days after my graduation, I was very grateful to begin to work with George Rupp, who offered me a scholarship, in a research project entitled “Non-Perturbative Hadron Spectroscopy”. However, it was not until 2011 that I decided to go ahead towards a PhD, a delay which was mainly due to the lack of appropriate funding, after several failed applications to obtain a PhD fellowship.

At first, I was mainly motivated by the title. I knew that hadrons are related to the strong interactions and I was acquainted with the word “spectroscopy” from atomic physics, but did not really know what it was in connection with the strong interaction, which made me curious. But mostly, I liked the exclusive expression “non-perturbative”. Non-perturbative, as opposed to perturbative, aims at a unitary description of reality which should be simpler, although eventually more complex, from the conceptual point of view.

The first six months of my studies were to familiarize myself with the model which is the basis of most of the research work I present in this thesis. Then I was interrupted by the lack of funding for five months, a time in which I worked as a secretary and as a guitar teacher. My uninterrupted research started finally by January 2009, until the fall of 2011, when I had to interrupt it again to fulfill the mandatory PhD courses. At last, I was forced to write the present thesis in only one month and a few days, due to an application to a Postdoc fellowship which requires the PhD completed until the end of this civil year. Therefore, I must ask apologies to the reader for the brevity of some explanations.

My research work as well as the PhD courses were developed at *Centro de Física das Interações Fundamentais*, at *Instituto Superior Técnico*, Lisboa, with Dr. George Rupp and always in straight collaboration with Prof. Eef van Beveren. It also included two stays at *Universidade de Coimbra*, one plus two weeks, where I had the opportunity to collaborate directly with Prof. Eef van Beveren. In the course of my research I was also supported to participate in six workshops concerning Hadronic

Physics: “Scadron70”, IST, 2007; “Excited QCD 2009”, Zakopane (Poland); “Excited QCD 2010”, Stara Lesna (Slovakia); 33rd International School of Nuclear Physics, Erice (Italy), 2011; IWHSS’12, Lisboa, 2012, and “Excited QCD 2012”, Peniche. In all the three “Excited QCD” workshops, I presented a plenary talk.

All my research results, except for some extra details, and unfinished work, have been published in international journals subject to a scientific refereeing system. These papers are the basis of the writing of this thesis. In each paper where I am the first author I contributed in the development of the models, performed all the computational work, plotted all the figures and tables, organized the papers, wrote the first draft and followed all the subsequent improvements.

List of publications:

1. S. Coito, G. Rupp, E. van Beveren, *The Nature of the $X(2175)$* , Acta Phys. Polon. Suppl. **2**, 431 (2009).
2. S. Coito, G. Rupp, E. van Beveren, *Multichannel calculation of excited vector ϕ resonances and the $\phi(2170)$* , Phys. Rev. D **80**, 094011 (2009). **(3rd Chapter)**
3. Susana Coito, George Rupp, Eef van Beveren, *Delicate interplay between the $D^0 - D^{*0}$, $\rho_0 - J/\psi$, and $\omega - J/\psi$ channels in the $X(3872)$ resonance*, Eur. Phys. J. C **71**, 1762 (2011). **(5th Chapter)**
4. S. Coito, G. Rupp, E. van Beveren, *Coupled-channel analysis of the $X(3872)$* , Acta Phys. Polon. Suppl. **3**, 983 (2010).
5. Susana Coito, George Rupp, Eef van Beveren, *Quasi-bound states in the continuum: a dynamical coupled-channel calculation of axial-vector charmed mesons*, Phys. Rev. D **84**, 094020 (2011). **(4th Chapter)**
6. S. Coito, G. Rupp, E. van Beveren, *Is the $X(3872)$ a molecule?*, Acta Phys. Polon. Suppl. **5**, 1015 (2012).
7. Susana Coito, George Rupp, Eef van Beveren, *$X(3872)$ is not a true molecule*, Eur. Phys. J. C **73**, 2531 (2013). **(6th Chapter)**
8. G. Rupp, S. Coito, E. van Beveren, *Light and Not So Light Scalar Mesons*, Acta Phys. Polon. Suppl. **2**, 437 (2009).
9. G. Rupp, S. Coito, E. van Beveren, *Complex masses in the S -matrix*, Acta Phys. Polon. Suppl. **3**, 931 (2010).

10. G. Rupp, S. Coito, E. van Beveren, *Towards Meson Spectroscopy Instead of Bump Hunting*, Prog. in Part. and Nucl. Phys. **67**, 449 (2012).
11. G. Rupp, S. Coito, E. van Beveren, *Meson Spectroscopy: Too Much Excitement and Too Few Excitations*, Acta Phys. Polon. Suppl. **5**, 1007 (2012).
12. Eef van Beveren, Susana Coito, George Rupp, *Substructures from weak interactions in light of possible threshold signals at LEP and LHC*, arXiv:1304.7711 [hep-ph].

Financial support:

- 9 Oct. 2007 – 8 Apr. 2008: *Non-Perturbative Hadron Spectroscopy*, PDCT/FP/63907/2005.
- 1 Aug. 2008 – 31 Oct. 2008: *Non-Perturbative Methods and Phenomena in the Standard Model*, POCI/FP/81913/2007.
- 1 Jan. 2009 – 31 Jul. 2009: *Hadron Production, Scattering and Spectroscopy*, CERN/FP/83502/2008.
- 1 Aug. 2009 – 31 Jan. 2010: SFA-2-91/CFIF.
- 3 Feb. 2010 – 2 Oct. 2010: *Hadronic Resonances and Confinement*, CERN/FP/109307/2009.
- 3 Oct. 2010 – 2 Feb. 2011: SFA-2-91/CFIF.
- 3 Feb. 2011 – 2 Nov. 2011: *Hadronic Resonances and Non-Resonances*, CERN/FP/116333/2010.
- 3 Nov. 2011 – 2 May 2012: SFA-2-91/CFIF.
- 3 May 2012 – 31 Dec. 2013: *Genuine Hadron Spectroscopy instead of Mere Bump Hunting*, CERN/FP/123576/2011.

Agradecimentos

Em primeiro lugar agradeço ao Senhor, a Sabedoria Infinita, por me ter conduzido por este caminho, e por ter providenciado sempre com tudo quanto necessitei. Em particular pelo dom da inteligência e ciência, e pelos frutos da paciência e perseverança, por entre todas as dificuldades, interiores e exteriores.

Em segundo lugar agradeço ao meu “boss”, George Rupp, que foi a pedra angular de todo este meu percurso, pelo seu apoio em todas as circunstâncias. O George foi para mim um orientador sempre presente, sempre optimista e motivador. Acreditou em mim, mesmo tendo em conta a minha modesta média de licenciatura, e incentivou-me a realizar este doutoramento. Por outro lado, encontrou sempre maneira de me financiar com bolsas de investigação, sem as quais não teria sido possível concluir esta etapa. Para além disso, ajudou-me sempre com todas as burocracias e problemas vários que foram surgindo ao longo do percurso. Finalmente, agradeço-lhe também o especial facto de nunca me ter mandado trabalhar!

Em terceiro lugar agradeço ao meu co-orientador, Eef van Beveren, o mestre. Por um lado, por me ter recebido sempre muito bem em Coimbra. Por outro lado, pela sua originalidade e excentricidade, e capacidade de atenção aos detalhes.

Agradeço também aos membros do Centro de Física das Interações Fundamentais por me terem apoiado na concessão das bolsas e das instalações, e ao pessoal da secretaria, pela sua simpatia e disponibilidade.

Aos meus colegas das pausas, especialmente ao Nuno Cardoso, Dmitri Antonov e Carlos Zarro, também pela sua amizade, e aos outros que me ajudaram e apoiaram como colegas em diversas circunstâncias. Agradeço também à Cristina, responsável pela limpeza do meu gabinete, pela sua amizade e compreensão. E aos meus colegas de corredor, porque me deixaram sempre tocar guitarra sem se queixarem.

Aos meus amigos que foram o meu báculo nos momentos mais complicados, e que partilharam a alegria dos momentos bons, em particular a Ana Rita Seita, Elsa Silva, Abílio Pequeno, Firmino Batista, Inês Costa, Marcos e Elena Borges de Pinho. E a

outros que, vivendo presentes no meu coração, não puderam acompanhar-me mais de perto durante este tempo.

Agradeço ainda, de coração, a toda a Congregação das Servas de Nossa Senhora de Fátima, que me acompanhou sempre no meu crescimento humano e espiritual, e, em particular, à comunidade da Casa Geral, que me recebeu na sua casa durante este último mês e meio, a fim de que eu pudesse escrever a tese na melhor paz. E de modo muito especial à irmã Mafalda Leitão, que me acompanhou ao longo de todo este tempo, mostrando-se sempre disponível e de coração aberto.

Por último, agradeço à minha família, aos meus pais e irmãos, por o amor ser sempre mais forte do que todas as incompreensões. E também aos meus avós, que já partiram deste mundo, que viveram do trabalho das suas mãos através do culto da terra, por serem os alicerces.

“A ciência humana mais aguda é ignorância cega ante a divina.”

in Liturgia das Horas, do Hino “Que salmos ou que versos”

in *Várias Rimas ao Bom Jesus*, Diogo Bernardes

Abstract

Quantum chromodynamics (QCD), the quantum field theory of strong interactions, is highly nonperturbative in the low-energy sector, where confinement dominates and resonance phenomena are observed. Therefore, phenomenological unquenched models based on the old ideas of the \mathcal{S} -matrix theory give a fundamental contribution to understand the complex pattern of masses, widths and shapes of experimentally observed meson resonances.

In the present thesis we employ the Resonance-Spectrum-Expansion coupled-channel model to study two enigmatic meson states, the isoscalar vector $\phi(2170)$ and the charmonium-like axial-vector $X(3872)$. The same model is applied to describe the peculiar pattern of masses and widths of the open-charm axial-vectors – pseudovectors $D_1(2420)$ and $D_1(2430)$, and $D_{s1}(2460)$ and $D_{s1}(2536)$. Furthermore, a simplified Schrödinger model is used to study the dominant wave-function components of $X(3872)$ near its resonance mass.

Both models successfully describe the whole variety of special features observed in experiment, which are not so easily explained in QCD-inspired quenched models.

Keywords: meson spectroscopy, unquenched, unitarity, coupled-channels, confinement, \mathcal{S} -matrix poles, Schrödinger models, dynamical resonances, hidden and open charm, axial-vectors.

Resumo

A teoria de campo para as interacções fortes, conhecida como Cromodinâmica Quântica (QCD), é altamente não perturbativa no regime de baixas energias, onde domina o confinamento de quarks, e onde são observados os fenómenos de ressonância de hádrões. Por conseguinte, os modelos fenomenológicos baseados nas ideias antigas da teoria da matriz \mathcal{S} podem contribuir, de modo fundamental, para a compreensão do padrão complexo de massas, larguras e formas de secção eficaz, das ressonâncias mesão observadas experimentalmente.

Na presente tese aplica-se um modelo “unquenched” de canais acoplados, denominado “Expansão do Espectro de Ressonâncias”, para estudar dois estados mesão enigmáticos, o vector isoscalar $\phi(2170)$ e o vector-axial do tipo charmónio $X(3872)$. O mesmo modelo é utilizado para descrever o padrão peculiar de massas e larguras dos vectores-axiais – pseudovectores com charm aberto $D_1(2420)$ e $D_1(2430)$, e $D_{s1}(2460)$ e $D_{s1}(2536)$. Desenvolve-se ainda um modelo simplificado de Schrödinger, para estudar as componentes dominantes da função de onda de $X(3872)$, junto ao limiar da sua massa de ressonância.

Ambos os modelos descrevem com sucesso toda a variedade de traços especiais destes mesões, observados na experiência, e que não são explicados tão facilmente através dos modelos “quenched” inspirados pela QCD.

Palavras-chave: espectroscopia de mesões, “unquenched”, unitariedade, canais acoplados, confinamento, polos da matriz \mathcal{S} , modelos de Schrödinger, ressonâncias dinâmicas, charm escondido e aberto, vectores-axiais.

Contents

Preface	i
Agradecimientos	v
Abstract	ix
Resumo	xi
1 Introduction	1
1.1 Historical Overview	1
1.2 The constituent quark model	2
1.3 Quantum Chromodynamics	4
1.4 \mathcal{S} -matrix theory	6
1.5 Phenomenological Models	8
1.6 Experimental Data	10
2 The Models	13
2.1 Some scattering formalism	13
2.2 The Resonance-Spectrum-Expansion (RSE) model	16
2.2.1 Redefining the S -matrix	18
2.3 Two-coupled-channel Schrödinger model	19
2.3.1 Solving the coupled-channel Schrödinger equation	20
2.4 Special functions, numerical methods, and kinematics	22
3 Strangeonium: ϕ's and the $\phi(2170)$	25
3.1 The RSE applied to ϕ recurrences	26
3.2 Experimental status of ϕ states	27
3.3 Hunting after poles	29
3.4 Cross sections	33

3.5	Summary and conclusions	35
4	Axials with open-charm	39
4.1	OZI-allowed channels for AV charmed mesons	40
4.2	Quasi-bound states in the continuum and other poles	42
4.3	Three-meson couplings	46
4.4	Summary and conclusions	47
5	The charmonium $X(3872)$	49
5.1	The RSE applied to charmonium 1^{++}	50
5.2	$X(3872)$ poles and amplitudes vs. data	53
5.3	Summary and conclusions	57
6	$X(3872)$ is not a true molecule	59
6.1	The coupled $c\bar{c}$ - D^0D^{*0} system	60
6.2	Poles	61
6.3	Wave function	64
6.4	Probabilities and r.m.s. radii	65
6.5	Stability of results and nature of poles	67
6.6	Summary and conclusions	70
	Summary and Conclusions	73

List of Figures

1.1	$\psi(3770)$, BES Collab. [35].	10
2.1	Born Expansion, ref. [41].	16
3.1	Trajectory of first continuum pole, for $2.26 \leq \lambda \leq 5.99$ ($\text{GeV}^{-3/2}$), from left to right. Bullet represents $\lambda = 4 \text{ GeV}^{-3/2}$, while dashed line indicates unphysical Riemann sheet.	28
3.2	1^3S_1 confinement pole for $4.31 \geq \lambda \geq 0$ ($\text{GeV}^{-3/2}$). Bullet represents $\lambda = 4 \text{ GeV}^{-3/2}$	29
3.3	2^3S_1 (lower) and 1^3D_1 (upper) confinement poles for $5.0 \geq \lambda \geq 0$ ($\text{GeV}^{-3/2}$) and $4.76 \geq \lambda \geq 0$ ($\text{GeV}^{-3/2}$), respectively. Bullets repre- sent $\lambda = 4 \text{ GeV}^{-3/2}$, while dotted and dashed lines indicate unphysical Riemann sheets.	30
3.4	3^3S_1 (lower) and 2^3D_1 (upper) confinement poles for $4.2 \geq \lambda \geq 0$ ($\text{GeV}^{-3/2}$) and $5.99 \geq \lambda \geq 0$ ($\text{GeV}^{-3/2}$), respectively. Bullets repre- sent $\lambda = 4 \text{ GeV}^{-3/2}$, while dotted and dashed lines indicate unphysical Riemann sheets.	32
3.5	Natural logarithm of the ratio of the elastic KK^* and KK cross sections.	33
3.6	Elastic D -wave (solid line) and S -wave (dashed line) $\phi(1020)f_0(980)$ cross section. Dotted line: S -wave cross section for 3S_1 channel only. .	34
3.7	Natural logarithm of the ratios of the elastic S -wave $\phi(1020)f_0(980)$ cross section and the elastic K^*K^* (solid line), $\phi(1020)\eta'$ (dotted line), and $K^*K_1(1270)$ (dashed line) cross sections.	35
3.8	Elastic P -wave KK cross section. Full line: both 3S_1 and 3D_1 $s\bar{s}$ channels included; dashed line: only 3S_1	36

4.1	$D_1(2430)$ pole trajectories as a function of λ , for $r_0 = 3.2\text{--}3.5 \text{ GeV}^{-1}$ (left to right). Solid curve and bullets correspond to $r_0 = 3.40 \text{ GeV}^{-1}$ and $\lambda = 1.30$, respectively.	43
4.2	$D_1(2420)$ pole trajectories as a function of λ , for $r_0 = 3.3\text{--}3.5 \text{ GeV}^{-1}$ (left to right). Solid curve and bullets correspond to $r_0 = 3.40 \text{ GeV}^{-1}$ and $\lambda = 1.30$, respectively.	44
4.3	$D_{s1}(2460)$ (dashed) and $D_{s1}(2536)$ (solid) pole trajectories as a function of λ , for $r_0 = 3.12 \text{ GeV}^{-1}$. Bullets correspond to $\lambda = 1.19$; vertical line shows D^*K threshold.	45
5.1	Pole trajectories for $r_1=3.0 \text{ GeV}^{-1}$ (solid curves) and $r_1=2.0 \text{ GeV}^{-1}$ (dotted curves); $g_{\rho^0 J/\psi}/g_{D^0 D^{*0}} = 0.07$ and $g_{\omega J/\psi}/g_{D^0 D^{*0}} = 0.21$ (upper two curves), $g_{\rho^0 J/\psi}/g_{D^0 D^{*0}} = 0.14$ and $g_{\omega J/\psi}/g_{D^0 D^{*0}} = 0.42$ (lower two curves). Note that the CM energy E is relative to the $D^0 D^{*0}$ threshold in all figures. Also see Table 5.2.	53
5.2	$D^0 D^{*0}$ elastic amplitude for poles 1, 2, 3 in Table 5.2 and Fig. 5.1; arbitrarily normalized data are from Ref. [117]. Elastic T -matrix elements follow from Eqs. (2.29–2.28); k is on-shell relative momentum. (b)for poles a, b, c.	54
5.3	$\rho^0 J/\psi$ (left) and $\omega J/\psi$ (right) elastic amplitudes for poles 1, 2, 3. Also see Fig. 5.1 and Table 5.2.	55
5.4	$\rho^0 J/\psi$ and $\omega J/\psi$ elastic amplitudes, for poles 2 (left) and 3 (right). Also see Fig. 5.1 and Table 5.2.	56
5.5	$\rho^0 J/\psi$ elastic amplitude for reduced ρ^0 width. Left: 0% (dots), 1% (dashes), 5% (full); right: 10% (dots), 50% (dashes), 100% (full). Studied case: pole 2 in Table 5.2. Also see Fig. 5.1.	57
6.1	Pole trajectories of dynamical (left) and confinement (right) poles as a function of g , for $a=2.0 \text{ GeV}^{-1}$ (top), 3.0 GeV^{-1} (middle), and 3.5 GeV^{-1} (bottom), respectively. In the last case, there is no bound state near threshold. Note: (i) poles in Table. 6.3 are here marked by *; (ii) arrows along curves indicate increasing g	63
6.2	Normalized two-component radial wave function $R(r)$ for three BEs, corresponding to labels A, X, D in Table 6.4, and two a values. Upper curves: $R_f(r)$; lower curves: $R_c(r)$. Left: $a = 2 \text{ GeV}^{-1}$; right: $a = 3 \text{ GeV}^{-1}$	65

- 6.3 Trajectories of dynamical and confinement poles. The bold curves represent cases *I* (top graph) and *II* (bottom graph) defined in Table 6.7, and the others the standard case of Fig. 6.1; the solid (dashed) lines stand for normal (below-threshold) resonances. All trajectories lie on the second Riemann sheet. The pole positions for the g values in Table 6.7 are marked by *. 68
- 6.4 Normalized two-component radial wave function $R(r)$, for cases *II* and "standard", corresponding to parameters in Table 6.7. Bold curves refer to case *II*, normal curve to R_c for standard case. Note: R_f is indistinguishable within graphical accuracy for the two cases. . . 70

List of Tables

1.1	Quantum Numbers of $q\bar{q}$. 5th column: spectroscopic notation.	3
1.2	Pseudoscalar and Vector Mesons	4
3.1	Included two-meson channels, their internal and relative angular momenta and spins, couplings squared for $n = 0$, and thresholds. See Ref. [65] for properties of listed mesons, except for the $K_0^*(800)$, discussed in the text.	27
3.2	Dependence of couplings squared on recurrency n	29
3.3	Masses of bare $s\bar{s}$ states in MeV, for HO potential with $\omega = 190$ MeV and $m_s = 508$ MeV (see Eqs. (2.31) and (2.32)).	30
3.4	Listed $J^{PC} = 1^{--}$ ϕ resonances, with masses and widths [65] (values for $\phi(1680)$ are estimates [65]).	31
3.5	Complex-energy poles in MeV, for 3S_1 $s\bar{s}$ channel only, and for both 3S_1 and 3D_1 . See text for further details.	31
4.1	Included meson-meson channels for $D_1(2420)$ and $D_1(2430)$, with ground-state couplings squared, Sec. 2.2, orbital angular momenta, and thresholds in MeV. For η and η' , a pseudoscalar mixing angle of 37.3° is used, as in Chapter. 3.	41
4.2	As Table 4.1, but now for $D_{s1}(2536)$ and $D_{s1}(2460)$	42
4.3	Poles of ground-state ($n = 0$) and first radially-excited ($n = 1$) AV charmed mesons. Parameters: $\lambda = 1.30$ (1.19) and $r_0 = 3.40$ (3.12) GeV^{-1} , for $c\bar{q}$ ($c\bar{s}$) states.	46
4.4	Poles of AV $c\bar{q}$ mesons, for different sets of included channels. Parameters: $\lambda = 1.30$, $r_0 = 3.40$ GeV^{-1}	46
4.5	Squared isospin recouplings for the 3-meson process $M_A \rightarrow M_B + M_C$, with $M_A = c\bar{s}$ or $c\bar{q}$	46

4.6	Squared ground-state coupling constants for the 3-meson process $M_A \rightarrow M_B + M_C$, with $J^{PC}(M_A) = 1^{+\pm}$, and M_A, M_B belonging to the lowest pseudoscalar or vector nonet.	47
5.1	Included meson-meson channels, with thresholds and ground-state couplings. For simplicity, we omit the bars over the anti-charm mesons; also note that D^*D^* stands for the corresponding mass-averaged charged and uncharged channels.	51
5.2	Pole positions of the dots and stars in Fig. 5.1. In all cases, $r_1 = 3.0 \text{ GeV}^{-1}$. Note that the OZIS couplings $\tilde{g}_{\rho^0 J/\psi}$ and $\tilde{g}_{\omega J/\psi}$ are given relative to the coupling of the OZIA $D^0 D^{*0}$ channel.	53
6.1	Fixed parameters.	60
6.2	Bound states (BS), virtual bound states (VBS), and resonances closest to threshold, for various g and a combinations.	62
6.3	Pole doubling: pairs of poles (in MeV) for some sets of a and g values, chosen such that the dynamical pole settles at the $X(3872)$ PDG [39] mass.	62
6.4	Five chosen binding energies (BE) in the $D^0 D^{*0}$ channel, for two different a values and the corresponding couplings g	64
6.5	Probabilities (in %) of the two wave-function components, for the cases specified in Table 6.4 (a in GeV^{-1}).	65
6.6	R.m.s. radii of the wave function, expressed in fm, for the cases specified in Table 6.4.	66
6.7	Probability of $c\bar{c}$ component and $X(3872)$ r.m.s. radius for varying ω, m_c , with bare E_0 fixed at 3599 MeV, $X(3872)$ pole at 3871.68 MeV, and $a = 2.0 \text{ GeV}^{-1}$	67

Chapter 1

Introduction

1.1 Historical Overview

In 1935 Hideki Yukawa proposed a field that should be responsible for the short-range force between the neutron and the proton, where the quanta would be bosons (integer spin) with charge $\pm e$ and mass about 200 times the mass of the electron [1]. Homi Bhabha introduced a similar particle but uncharged to account for the interaction between two protons [2]. This new particle, proposed as the mediator of the field, was named *meson*, for having a mass intermediate between the electron and the proton. It was discovered from cosmic rays in 1947, by Cecil Powell in collaboration with Giuseppe Occhialini [3]. In the same year, also with César Lattes, the same authors identified another “meson”, the already discovered *muon*, which does not interact strongly, and distinguished it from the former meson which was called *pion* [4]. This was followed by the discovery of a panoply of strongly interacting particles, both baryons, with mass above the proton mass and half-integer spin (fermions), and mesons. The term “meson” was then redefined to designate solely particles with intermediate mass which interact strongly, thus excluding the *muon*. In 1961 Murray Gell-Mann proposed “The Eightfold Way”, a scheme of classification of baryons and mesons based on symmetries and on the already discovered states, where the eight known baryons were grouped in a supermultiplet, and the mesons in two octets of pseudoscalars and vectors, plus two singlets [5]. A similar representation was independently proposed by Yuval Ne’eman in the same year [6]. Inquiring about the origin of the internal symmetries of isospin or hypercharge, the mechanism of *bootstrap* was introduced, which states that the internal symmetries can be expressed as equalities among certain masses and couplings, whose values are not put in by hand but emerge from self-consistency [7]. However, a different scheme

was proposed in 1964 by Gell-Mann, which postulates that the baryons and mesons are composite systems of *quarks* q and *antiquarks* \bar{q} , where baryons are combinations (qqq) , $(qqqq\bar{q})$, etc., and mesons $(q\bar{q})$, $(qq\bar{q}\bar{q})$, etc., within $SU(3)$ flavor symmetry [8]. A similar picture was proposed independently by George Zweig, which used the term *aces* instead of quarks [9]. Evidence of a composite proton came out in 1969, in experiments of deep inelastic scattering performed by E. Bloom *et al.* and by M. Breidenbach *et al.* [10]. James Bjorken and Sidney Drell contributed significantly to this discovery by proposing experimental methods to study the proton pointlike constituents, the “partons”, after Feynman, relating further *partons* to quarks [11]. As mentioned above, there were two known internal symmetries of the mesons and baryons, viz. *isospin* and the *hypercharge*, a sum over *baryon number* and *strangeness*. A new internal symmetry was revealed after the discovery of the meson J/ψ in 1974 [12], namely *charm*, which adds to hypercharge.

Finally, a new quantum group associated with the strong interaction was postulated in 1973 by David Gross and Frank Wilczek, the *color* gauge group, in the context of non-Abelian field theories [13].

1.2 The constituent quark model

The constituent quark model is based on all the discoveries mentioned above, in particular the “eightfold way”, and some further developments. It offers the most complete classification scheme of mesons and baryons. Generically, we define *hadrons* as all particles and states that are subject to the strong interaction. Within the quark model, a meson is a hadron composed of a quark-antiquark pair $q\bar{q}$, while the baryon is a hadron composed of three quarks qqq . No other hadrons were contemplated in the original model. The name “constituent” is used, because the postulated elementary quarks have never been observed in isolation, which implies that their mass must be estimated from the composite hadrons, as an effective, constituent mass. As far as we know, from experiment and Standard Model predictions, there are six different quark *flavors*, namely *up* – u and *down* – d , associated with isospin symmetry, *strange* – s associated with the strangeness quantum number, *charm* – c , *bottom* – b and *top* – t .

The symmetries considered in the quark model are the flavor group $SU(3)$, or $SU(4)$, the spin group $SU(2)$, electric charge, parity, C -parity and G -parity. The flavor group is not an exact symmetry due to differences among the masses of the quarks. Yet $SU(3)$, with $q = u, d, s$, is a reasonably good symmetry, whereas $SU(4)$, with

		J^{PC}	J	L	S	$^{2S+1}L_J$
Pseudoscalar	P	0^{-+}	0	0	0	1S_0
Vector	V	1^{--}	1	0, 2	1	$^3S_1, ^3D_1$
Scalar	S	0^{++}	0	1	1	3P_0
Axial Vector	A^+	1^{++}	1	1	1	3P_1
Pseudovector	A^-	1^{+-}	1	1	0	1P_1
Tensor	T	2^{++}	2	1, 3	1	$^3P_2, ^3F_2$
Tensor	T	2^{-+}	2	2	0	1D_2
Tensor	T	2^{--}	2	2	1	3D_2

Table 1.1: Quantum Numbers of $q\bar{q}$. 5th column: spectroscopic notation.

$q = u, d, s, c$, is badly broken due to the considerably larger charm mass. Quarks are fermions with spin $1/2$ and $SU(2)$ is an exact symmetry. Baryons may have spin $S = 1/2, 3/2$ while mesons have $S = 0, 1$. Henceforth only mesons will be described, as they are the subject of this thesis. Parity is defined as $P = (-1)^{L+1}$, where L is the orbital angular momentum and the additional factor -1 is due to the intrinsic parity of the fermion-antifermion pair $q\bar{q}$. Charge-conjugation or C -parity is an operator given by $C = (-1)^{L+S}$, being applicable only to particles which are their own antiparticles. Also, the G -parity operator is defined by $G = (-1)^IC$, where I is the isospin. Parity, C -parity, G -parity and J are conserved under strong interactions. In Table 1.1 the lowest angular excitations of the quark-model mesons are summarized. The flavor multiplets are constructed as follows:

$$SU(3) \rightarrow 3 \otimes \bar{3} = 8 \oplus 1$$

$$\text{Isovectors: } I = 1, I_3 = 1, 0, -1 \rightarrow \left(u\bar{d}, \frac{1}{\sqrt{2}}(u\bar{u} - d\bar{d}), d\bar{u} \right)$$

$$\text{Isodoublets: } I = 1/2, I_3 = 1/2, -1/2 \rightarrow \left(u\bar{s}, s\bar{d}, d\bar{s}, s\bar{u} \right)$$

$$\text{Isoscalars: } I = 0 \rightarrow |8\rangle = \frac{1}{\sqrt{6}}(u\bar{u} + d\bar{d} - 2s\bar{s}), |1\rangle = \frac{1}{\sqrt{3}}(u\bar{u} + d\bar{d} + s\bar{s})$$

Here, all states within the nonet are orthogonal. In addition,

$$SU(4) \rightarrow 4 \otimes \bar{4} = 15 \oplus 1$$

$$\text{Open charm: } C = 1, C_3 = 1, -1 \rightarrow \left(c\bar{u}, c\bar{d}, c\bar{s}, u\bar{c}, d\bar{c}, s\bar{c} \right)$$

$$\text{Unflavored: } |15\rangle = \frac{1}{\sqrt{12}}(u\bar{u} + d\bar{d} + s\bar{s} - 3c\bar{c}), |1\rangle_{SU(4)} = \frac{1}{\sqrt{4}}(u\bar{u} + d\bar{d} + s\bar{s} + c\bar{c})$$

However, the $c\bar{c}$ component decouples from the $|15\rangle$ and $|1\rangle_{SU(4)}$ states and in practice the unflavored states of the broken group will be $|8\rangle$, $|1\rangle$, and $|c\bar{c}\rangle$, i.e., *charmonium*. Within $SU(3)$ there is some mixing between the *strangeonium* $|s\bar{s}\rangle$ and the

$q\bar{q}$	P	V
$u\bar{d}, \frac{1}{\sqrt{2}}(u\bar{u} - d\bar{d}), d\bar{u}$	π^+, π^0, π^-	ρ^+, ρ^0, ρ^-
$u\bar{s}, s\bar{d}, d\bar{s}, s\bar{u}$	K^+, \bar{K}^0, K^0, K^-	$K^{*+}, \bar{K}^{*0}, K^{*0}, K^{*-}$
$ 8\rangle$	$\cos \theta_P \eta\rangle + \sin \theta_P \eta'\rangle$	$\cos \theta_V \omega\rangle + \sin \theta_V \phi\rangle$
$ 1\rangle$	$-\sin \theta_P \eta\rangle + \cos \theta_P \eta'\rangle$	$-\sin \theta_V \omega\rangle + \cos \theta_V \phi\rangle$
$c\bar{u}, c\bar{d}, c\bar{s}, u\bar{c}, d\bar{c}, s\bar{c}$	$D^0, D^+, D_s^+, \bar{D}^0, D^-, D_s^-$	$D^{*0}, D^{*+}, D_s^{*+}, \bar{D}^{*0}, D^{*-}, D_s^{*-}$
$c\bar{c}$	η_c	J/ψ

Table 1.2: Pseudoscalar and Vector Mesons

$|n\bar{n}\rangle := \frac{1}{\sqrt{2}}(u\bar{u} + d\bar{d})$ components. Table 1.2 lists the light-quark nonets, as well as the heavy-quark mesons with charm, for pseudoscalars and vectors. The octet and singlet states are mixtures of physical states which can be written as:

$$\begin{aligned}
|\psi\rangle &= \cos \theta |8\rangle - \sin \theta |1\rangle, \quad |\psi\rangle = \cos \phi |n\bar{n}\rangle - \sin \phi |s\bar{s}\rangle, \\
|\psi'\rangle &= \sin \theta |8\rangle + \cos \theta |1\rangle, \quad |\psi'\rangle = \sin \phi |n\bar{n}\rangle + \cos \phi |s\bar{s}\rangle,
\end{aligned} \tag{1.1}$$

where $\phi = \theta + 54.736^\circ$. The mixing angle, which is determined empirically, is only relevant for the pseudoscalars η , η' . Finally, the $q\bar{q}$ states within the quark model are the whole set of angular plus radial excitations, the latter associated with the quantum number n .

1.3 Quantum Chromodynamics

Although the constituent quark “model”, as outlined above, is a good starting point for spectroscopy work, it does not yet include any dynamics and so cannot explain all hadronic states nor resonance phenomena. Even within its quality of a classification scheme, it is a simplification of reality. In a physical quantum system, there are continuous creation and annihilation phenomena, which can be described through the method of second quantization. Therefore, a mesonic system should be a composition of a “permanent” $q\bar{q}$ component, the *valence* quarks, and a fluctuation component composed of $q\bar{q}$ pairs that are continuously being created and annihilated, the *sea* quarks. This is still a simplified scheme.

Quantum Chromodynamics (QCD) is a gauge-field theory developed upon the concept of *color* and based on the successful theory of quantum electrodynamics, which can be treated perturbatively [13, 14]. QCD introduces a new fundamental degree of freedom, which is the mediator of the strong interaction, called *gluon*, a massless

particle of spin 1, electrically neutral, but color charged and with the property of being self-interacting. The theory only allows colorless compositions of quarks in the final states, like the common mesons and baryons, but additionally $qq\bar{q}\bar{q}$ or $q\bar{q}q\bar{q}$ tetraquarks, $qqqq\bar{q}$ pentaquarks, etc., and also combinations between quarks and gluons as well, the *hybrids*, and compositions of gluons only, the *glueballs*. All these configurations are labeled *exotics*. The theory also predicts another internal degree of freedom without external “legs”, the *ghost* fields, to account for gauge invariance. Empirical observations of the strong interaction reveal two fundamental properties of the force, namely *confinement* and *asymptotic freedom*, both related to the spatial or, equivalently, momentum scale of the interaction. That is, quarks and gluons are always bound in colorless singlets at the femtometer scale, and behave as quasi-free below 1 fm, a region which can be probed at high momentum transfer. This is explained within QCD via the properties of the renormalized *coupling* strength of the interaction, which grows with the separation distance between the elementary quarks and gluons.

Although QCD might be an attractive theory for its conceptual simplicity, due to the highly *nonperturbative* character of the strong interaction this simplicity is deceiving. In practice the perturbation expansion can be performed only at very high energies, outside the physical regime of interest here, where confinement dominates and resonance phenomena are observed. Anyhow, the machinery of calculus is always very extensive, involving many details and techniques.

In what concerns the subject of hadron spectroscopy, QCD may contribute in two ways. The most direct approach is via *lattice QCD*, i.e., the heavy computational calculus of the full nonperturbative theory on a finite and discrete lattice. The indirect contribution is via models that are QCD inspired.

Finally, there is an empirical rule applicable to mesons, related to the dynamics of the interaction, viz. the *Okubo-Zweig-Iizuka* (OZI) rule [9, 15], which states that meson decay channels which require the creation of a new $q\bar{q}$ pair besides the original pair, by breaking the latter’s *string*, are strongly favored - *OZI-allowed*, whereas the decay channels that involve a pair creation from the vacuum without breaking the string of the original pair are highly suppressed - *OZI-suppressed*. In the latter type, intermediate gluons must carry energy enough to transform into a $q\bar{q}$ pair.

1.4 \mathcal{S} -matrix theory

There is another way to approach a physical problem without going into all details of a microscopic description, which is by reducing the parameters of the system to only a few, and then to calculate the dynamics fully. From a conceptual point of view it may be harder to understand, but the touchstone conferring reliability to these approaches is the comparison with experimental data. This is the spirit in which the *Scattering matrix* - \mathcal{S} -matrix - theory of strong interactions was built and developed. One of the reasons why field theories are often preferred is the claim of being built upon first principles. Henry Stapp discussed [16] the physical relevance of such principles on one side, and the possibility of constructing an \mathcal{S} -matrix theory over axioms on the other side. In what concerns field theories, he pointed out: (i) it is not known whether the principles admit any rigorous solutions, except for trivial ones; (ii) the principles depart from hypothetical space-time points, which are not observables; (iii) the specific principles of positive definiteness, nondegeneracy of the vacuum, completeness, locality, and energy spectrum are restrictive and arbitrary. In addition, he understood there is a disconnection between field theory and practical calculations, adding:

“Practical calculations are the heart of physics, and it is the job of physical axioms to specify a connection between experience and a well-defined mathematical scheme in which practical calculations have place.”

Then, he proposed seven postulates for \mathcal{S} -matrix theory:

1. There is a linear relation between the probabilities and the squares of amplitudes, according to basic quantum theory. This postulate leads to unitarity.
2. Certain sets of experiments are complete, e.g., the measurement of momentum, spin and particle type of all particles present are a complete set. Interference effects are observable.
3. The connection of momentum functions to space-time coordinates is given by a Fourier transformation.
4. Relativistic invariance.
5. The physical interpretation of the quantities of the theory be such that translational and rotational invariance imply conservation of energy-momentum and angular momentum.

6. From the above postulates one can construct a set of scattering functions which satisfy unitarity, and are analytic in the interior and on the boundary of their physical sheet, except for singularities required by unitarity, due to phase space.
7. All physical-type points of the physical sheet correspond to processes actually occurring in nature.

Geoffrey Chew added [17, a.] to these postulates three assumptions: (i) maximal smoothness, i.e., maximal analyticity; (ii) maximal strength, i.e., saturation of the unitary condition; and (iii) isospin, strangeness, baryon number, etc., conservation. In a different paper [17, b.], Chew and Steven Frautschi stressed the importance of the definition of “pure potential scattering” instead of scattering of “independent” particles, and they stated, after observing several experimental tests:

“It is plausible that none of the strongly interacting particles are completely independent but that each is a dynamical consequence of interactions between others.”

The theory of the scattering matrix was constructed on the basis of the principles of quantum mechanics and the pioneering work of John Wheeler [18]. He proposed the “method of resonating group structure” to nuclear physics, which he contrasted with the Hartree-Fock procedure, i.e., the method of building up a wave function for a whole problem out of partial wave functions that describe the close interactions within the individual groups, instead of directly building up a wave function for a system of many particles. He obtained the scattering matrix as a unitary relation which “connects the asymptotic behavior of an arbitrary particular solution with that of solutions possessing a standard asymptotic form”, cf. Eq. (48), which corresponds to $S_J = e^{i2\delta_J}$, where δ_J is the phase shift.

Another important precursor work [19] was due to Tullio Regge, who extended the analyticity of the radial Schrödinger equation to complex orbital momenta, relating potentials with scattering amplitudes, and further deriving pole positions from the transmitted momentum. These *Regge poles* were associated with bound states and resonances that can be viewed in the complex energy E plane for fixed angular momentum J or vice versa. The trajectory of a single pole in the J plane as E changes would correspond to a family of “particles” of different mass, thus defining a *Regge trajectory* [17, c.].

Some classical reading about *S*-matrix theory may be found in Ref. [20].

1.5 Phenomenological Models

Bound states calculated within the quark model essentially describe the valence-quark contribution, i.e., the *quenched* spectrum. Phenomenological models which treat the resonant spectrum of bare states without considering any other relevant hadron degrees of freedom are thus considered *quenched* approaches. This is the case of, e.g., the mainstream model of Stephan Godfrey and Nathan Isgur (GI), a QCD inspired model [21], where the meson spectrum is built up over a Coulomb-plus-linear “funnel” potential. Here, the authors distinguish between “soft” QCD - quenched, and “true QCD” - *unquenched*, which includes the whole QCD action. In the same spirit, also the exotic states should have a “quenched” spectrum which, in combination with the regular $q\bar{q}$ mesons, or qqq baryons, would give rise to the complex structures observed in the experiments.

Instead, unquenched descriptions state that, besides the important valence-quark contribution, a meson or baryon is dressed with other relevant hadron components which must be included in an appropriate description of the experimental data. This “dressing” comes from the strongly coupled nonlinear character of the interaction. In Ref. [22] the authors suggested two opposite unquenching methods, by either dressing quark-model states and comparing the outcome to the experiments, or by taking into account self-energy contributions, implicitly included in the measured scattering-matrix poles, through an “undressing” procedure and comparing the outcome to the quark model. This undressing may be performed through a coupled-channel model involving hadronic mass shifts, related to off-shell effects.

Nonperturbative microscopical approaches are employed to study the confinement problem. Within QCD, quarks and gluons interact via effective *strings* with a potential that grows linearly with the separation distance between two color particles, at the scale $1/\Lambda_{QCD} \sim 5 \text{ GeV}^{-1}$, where Λ_{QCD} is the QCD scale parameter, and the slope of the potential is given by the string tension, $\propto \Lambda_{QCD}^2$.

Another important nonperturbative phenomenon is the spontaneous breaking of *chiral* symmetry, which leads to the appearance of pseudoscalar Goldstone bosons, a role played by the pion. This symmetry corresponds to the $SU_L(N_f) \times SU_R(N_f)$ symmetry group, with L, R for left- and right-handed quark fields, respectively, and N_f the number of flavors of light quarks. A textbook concerning nonperturbative methods in gauge theories can be found in Ref. [23]. Effective approaches to spontaneous chiral-symmetry breaking are given by the nonrenormalizable Nambu-Jona-Lasinio model [24] and the linear sigma model [25]. A nonperturbative version of the latter

model, at the quark instead of nuclear level, was constructed by Delbourgo and Scadron, both for $N_f = 2$ and $N_f = 3$ [26], leading to accurate predictions of a host of low-energy observables. Another approach to dynamical chiral-symmetry breaking is by employing a current quark model with a chirally symmetric confining potential [27]. Related with chiral symmetry is the concept of *Adler zeros*, i.e., zero-mass pions which are emitted or absorbed in a strong interaction or first-order electromagnetic process [28].

A distinction is usually made among quark-mass assignments. The constituent quark masses, used in hadron spectroscopy, the dynamical quark masses, generated through chiral noninvariance of the QCD vacuum, and current quark masses, which correspond to the bare quarks and are associated with current divergences and higher momentum transfers [29].

In constituent quark models the meson spectrum is generally obtained by solving the Schrödinger equation using some effective potential, which includes a $q\bar{q}$ confining part and also spin-dependent components, such as spin-orbit and color hyperfine interactions. The free parameters are then tuned to give agreement with experiment [30]. Some models include relativistic effects [21] that should be comparable to the orbital splittings in the light-quark systems. The standard confining potential is the already mentioned “funnel” potential given by

$$V(\vec{r}_{ij}) = -\frac{4}{3} \frac{\alpha_s(r)}{r} + br + C, \quad (1.2)$$

where $\alpha_s(r)$ is the running coupling constant of the strong interactions and C is an integration constant. The Coulomb part is dominant for smaller radii, typically for heavy systems, while the linear component dominates at larger radii, characteristic of light-quark systems. Linear Regge trajectories are usually seen as a consequence of the linear part of the potential.

Meson decays involve creation of $q\bar{q}$ pairs. In some models a pair is formed through intermediate gluons in a 3S_1 state, with $J^{PC} = 1^{--}$. The most common assumption is pair creation with vacuum quantum numbers, i.e., in a 3P_0 state, with $J^{PC} = 0^{++}$. This can be formulated in terms of a harmonic-oscillator spatial $SU(6)$ basis [31]. Comparison with experimental decays highly favors the 3P_0 model [32]. It is possible that the mechanism of $q\bar{q}$ pair creation is strongly related to the OZI rule [33].

1.6 Experimental Data

Scattering-matrix poles may be studied via partial-wave analyses, typically by measuring experimental phase shifts, amplitudes, and cross sections. These quantities are always unquenched, by definition. A typical resonant cross section is usually described by a simple *Breit-Wigner* (BW) formula, original Ref. [34], for a process $1 + 2 \rightarrow 1' + 2'$:

$$\sigma = \frac{4\pi}{q^2} \frac{2J+1}{(2s_1+1)(2s_2+1)} |A|^2, \quad (1.3)$$

where s_1, s_2 are the spins of the incoming particles, J is the spin of the resonance, q is the c.m. momentum, and the BW scattering amplitude A is given by

$$A = \frac{x\Gamma/2}{M - \sqrt{s} - i\Gamma/2}. \quad (1.4)$$

where x is the branching fraction of a given decay channel, \sqrt{s} is the c.m. energy, M is the resonance mass, and Γ its total decay width. These kinds of bell-shaped structures usually define the mass and width of a resonance. However, resonance peaks may be very broad and the line shapes very deformed, in which cases the definition of both parameters is not clear at all. Figure 1.1, Ref. [35], illustrates one of these “deformed” signals viz., at the $\psi(3770)$ resonance. Although the BW

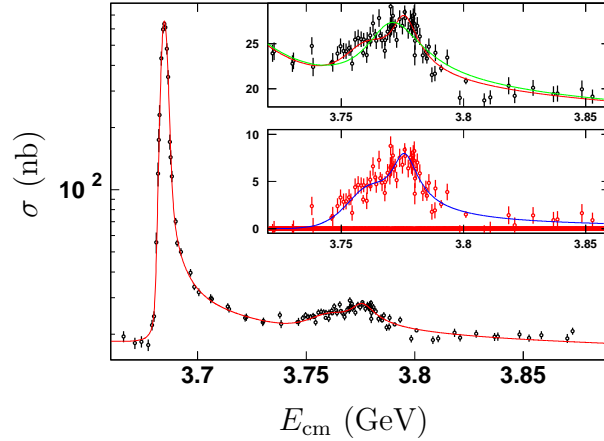


Figure 1.1: $\psi(3770)$, BES Collab. [35].

mass is assumed by some to be the proper physical property, the real part of the corresponding pole position in the complex energy plane may be also a good definition of resonance mass. These two definitions of mass are only equivalent for very narrow resonances. In a recent work [36] a modified BW formula, with a new phase parameter, adjusts to different resonance shapes in a model-independent way.

Thresholds play a key role in understanding resonances. Some mesons appear very close to a specific decay channel, such as the $X(3872)$, which we will discuss further on, but also the scalars $f_0(980)$, $a_0(980)$, $K_0(1430)$, and the tensor $f_2(1565)$. This kind of resonances often display a *cusp* like line shape. However, not all cusps are necessarily generated by resonant states, but may instead be produced by some inelastic mechanism, as has been discussed by David Bugg [37].

Other enhancements with resonant shapes observed in the decay channels may not correspond to true resonances, as suggested in [38] for the case of the $X(4260)$. Furthermore, a resonant state may produce a dip instead of a bump, due to the opening of competing decay channels.

Resonant phenomena associated with hadrons are not trivial to resolve from the experimental point of view. Signal distortions may be due to the superposition of partial waves, or inelasticities due to competing decay channels and nearby thresholds. Also contributing to the complexity of data analysis are the large widths of some resonances, and the opening of many decay channels, which diminishes the branching fraction of each channel, especially in the case of radial excitations. A careful look at the listings of the Particle Data Group [39] allows us to understand that many states predicted by the quark model are missing. In particular, the first and second radial excitations are not well established for all angular excitations in any flavor sector. Experimental research in the low-energy resonance region is far from being complete, for besides the need of a deeper understanding of the enhancements, which often requires more statistics, many more states are predicted than those that are observed. Moreover, the real existence of exotic hadrons is still not unequivocal. Phenomenological models, while trying to explain resonances and nonresonant structures from a theoretical point of view, depend entirely on the experimental data to be tested. In conclusion, more efforts are needed, especially experimental ones, in this very topical issue of hadron spectroscopy. For further reading, see Ref. [40].

Chapter 2

The Models

In this thesis two coupled-channel models are employed to study three types of mesonic resonances: the strangeonium vector $\phi(2170)$, the pseudovectors–axial-vectors $D_1(2420)$, $D_1(2430)$, $D_{s1}(2536)$ and $D_{s1}(2460)$, and the charmonium-type axial-vector $X(3872)$. All resonances are studied within the *Resonance-Spectrum-Expansion* (RSE) model. The $X(3872)$, alias $\chi_{c1}(2P)$, is additionally studied in a simple two-channel model where the wave function is fully determined. Both models are unquenched, are based on the simplified constituent quark model presented in Sec. 1.2, and rely on the spirit of \mathcal{S} -matrix theory discussed in Sec. 1.4.

2.1 Some scattering formalism

At instant $t = 0$ a freely moving wave packet, at distance r_0 from a target with radius a , where $r_0 \gg a$, is given by

$$\psi(\vec{r}, 0) = \frac{1}{(2\pi)^{3/2}} \int d^3k \, \varphi(\vec{k}) e^{i\vec{k} \cdot (\vec{r} - \vec{r}_0)}. \quad (2.1)$$

This plane wave may be replaced by

$$\psi(\vec{r}, 0) = \int d^3k \, \varphi(\vec{k}) e^{-i\vec{k} \cdot \vec{r}_0} \psi^{(+)}(\vec{k}, \vec{r}), \quad (2.2)$$

where the retarded wave function $\psi^{(+)}$ is a solution of the stationary Schrödinger equation (2.3) and an eigenfunction of the Hamiltonian with a short-range central potential

$$[-\nabla^2 + 2mV(\vec{r})]\psi^{(+)}(\vec{k}, \vec{r}) = k^2\psi^{(+)}(\vec{k}, \vec{r}). \quad (2.3)$$

The Green's function $G(\vec{r}, \vec{r}')$ is a propagator function defined as a solution of the differential equation

$$\frac{1}{2m}(\nabla^2 + k^2)G(\vec{r}, \vec{r}') = \delta^{(3)}(\vec{r} - \vec{r}'). \quad (2.4)$$

One particular solution is the retarded Green's function

$$G_+(\vec{r}, \vec{r}') = -\frac{m}{2\pi} \frac{e^{ik|\vec{r}-\vec{r}'|}}{|\vec{r}-\vec{r}'|}. \quad (2.5)$$

The *Lippman-Schwinger* (LS) equation is then written as

$$\psi^{(+)}(\vec{k}, \vec{r}) = \frac{e^{i\vec{k}\cdot\vec{r}}}{(2\pi)^{3/2}} + \int d^3r' G_+(\vec{r}, \vec{r}') V(\vec{r}') \psi^{(+)}(\vec{k}, \vec{r}'). \quad (2.6)$$

This integral equation, which includes the boundary conditions, is a formal solution of (2.3).

Substituting (2.5) in (2.6), the asymptotic expression for $\psi^{(+)}$ becomes

$$\psi^{(+)}(\vec{k}, \vec{r}) \approx \frac{1}{(2\pi)^{3/2}} \left(e^{i\vec{k}\cdot\vec{r}} + \frac{e^{ikr}}{r} f(\vec{k}, \hat{r}) \right) \quad (r \text{ large}), \quad (2.7)$$

where

$$f(\vec{k}, \hat{r}) = -(2\pi)^{1/2} m \int d^3r' e^{-ik\hat{r}\cdot\vec{r}'} V(\vec{r}') \psi^{(+)}(\vec{k}, \vec{r}'). \quad (2.8)$$

With the help of the Møller operator

$$\Omega^{(+)} = \lim_{t \rightarrow \infty} e^{iHt} e^{-iH_0 t}, \quad (2.9)$$

the definition $|\psi^{(+)}(\vec{k})\rangle = \Omega^{(+)} |\vec{k}\rangle$, and

$$G(z) = (z - H_0 - V)^{-1} = (z - H)^{-1}, \quad (2.10)$$

where z is an arbitrary complex variable, we get

$$|\psi^{(+)}(\vec{k})\rangle = \left[1 + \lim_{\epsilon \rightarrow 0} G(E(k') + i\epsilon)V \right] |\vec{k}\rangle. \quad (2.11)$$

The transition operator is defined by

$$T(z) = V + VG(z)V, \quad (2.12)$$

so that

$$\langle \vec{k}' | V | \psi^{(+)}(\vec{k}) \rangle = \lim_{\epsilon \rightarrow 0} \langle \vec{k}' | T(E(k) + i\epsilon) | \vec{k} \rangle. \quad (2.13)$$

In case of spherical symmetry let us assume

$$\langle \vec{k} | T(k^2 + i\epsilon) | \vec{k}' \rangle = \sum_{l=0}^{\infty} (2l+1) P_l(\hat{k} \cdot \hat{k}') T_l(k, k'), \quad (2.14)$$

where P_l are Legendre polynomials. Using $\psi^{(+)}(\vec{k}, \vec{r}) = \langle \vec{r} | \psi^{(+)}(\vec{k}) \rangle$, Eq. (2.14), and also a plane-wave expansion in spherical harmonics, the integration of Eq. (2.8) yields

$$f(\vec{k}, \hat{r}) = -4\pi^2 m \sum_{l=0}^{\infty} (2l+1) P_l(\hat{k} \cdot \hat{r}) T_l(k). \quad (2.15)$$

The scattering operator is defined by

$$S(\vec{k}', \vec{k}) = \langle \psi^{(-)}(\vec{k}') | \psi^{(+)}(\vec{k}) \rangle. \quad (2.16)$$

It can be proved that its relation to T is given by

$$S(\vec{k}', \vec{k}) = \delta^{(3)}(\vec{k}' - \vec{k}) - 2\pi i \delta(E(k') - E(k)) \langle \vec{k}' | T(E(k) + i\epsilon) | \vec{k} \rangle, \quad (2.17)$$

which equation explicitly shows that the matrix elements of S are *on-shell* while those of T may be *off-shell*.

As an example, consider the spherically symmetric potential

$$V(\vec{r}, \vec{r}') = \delta^{(3)}(\vec{r} - \vec{r}') V(r), \quad (2.18)$$

which in momentum space reads

$$V(\vec{k}, \vec{k}') = \frac{1}{2\pi^2} \sum_{l=0}^{\infty} (2l+1) P_l(\hat{k} \cdot \hat{k}') \int_0^{\infty} r^2 dr V(r) j_l(kr) j_l(k'r), \quad (2.19)$$

where j_l is a spherical Bessel function. If we define

$$V(r) = \frac{\lambda}{2\mu a} \delta(r - a), \quad (2.20)$$

Eq. (2.19) reduces to

$$V(\vec{k}, \vec{k}') = \frac{\lambda a}{4\pi^2 \mu} \sum_{l=0}^{\infty} (2l+1) P_l(\hat{k} \cdot \hat{k}') j_l(ka) j_l(k'a). \quad (2.21)$$

Finally, using Eq. (2.12) we get

$$\langle \vec{p} | T | \vec{p}' \rangle = \langle \vec{p} | V | \vec{p}' \rangle + \int d^3 k' \int d^3 k \langle \vec{p} | V | \vec{k}' \rangle \langle \vec{k}' | G_0(z) | \vec{k} \rangle \langle \vec{k} | T(z) | \vec{p}' \rangle, \quad (2.22)$$

$$G_0(\vec{k}', \vec{k}; z) = \langle \vec{k}' | (z - H_0)^{-1} | \vec{k} \rangle = \frac{2\mu}{2\mu z - k'^2} \langle \vec{k}' | \vec{k} \rangle. \quad (2.23)$$

The first term of the Born expansion of Eq. (2.22) gives

$$T_l^{(1)}(p, p') = \frac{\lambda a}{4\pi^2 \mu} j_l(pa) j_l(p'a), \quad (2.24)$$

the second order term

$$T_l^{(2)}(p, p') = -\frac{i\lambda^2 pa^2}{4\pi^2 \mu} j_l^2(pa) h_l^{(1)}(pa) j_l(p'a), \quad (2.25)$$

and the whole T operator becomes

$$T(\vec{p}, \vec{p}') = \frac{\lambda a}{4\pi^2 \mu} \sum_{l=0}^{\infty} (2l+1) P_l(\hat{p} \cdot \hat{p}') \frac{j_l(pa) j_l(p'a)}{1 + i\lambda pa j_l(pa) h_l^{(1)}(pa)}. \quad (2.26)$$

2.2 The Resonance-Spectrum-Expansion (RSE) model

The RSE coupled-channel model describes elastic scattering of the form $AB \rightarrow CD$, where A, B, C , and D may be in principle any hadrons. In all applications here, they are non-exotic mesons M . The transition operator, Eq. (2.22), is described by a matrix, where each row or column represents a different channel. Its Born expansion may be represented by the diagrams in Fig. 2.1. The effective meson-

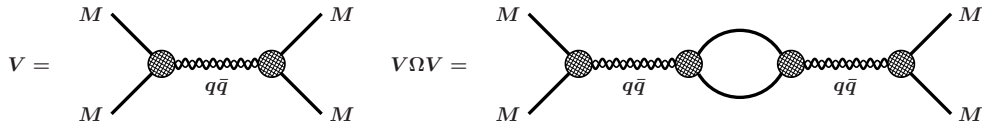


Figure 2.1: Born Expansion, ref. [41].

meson potential consists of an intermediate-state s -channel $q\bar{q}$ propagator between two $q\bar{q}$ -meson-meson vertex functions for the initial and final state, reading [41]

$$V_{ij}^{(L_i, L_j)}(p_i, p_j; E) = \lambda^2 j_{L_i}^i(p_i a) \mathcal{R} j_{L_j}^j(p_j a) \quad (2.27)$$

with

$$\mathcal{R}_{ij} = \sum_{l_c, S} \sum_{n=0}^{\infty} \frac{g_{nl_c S}^i g_{nl_c S}^j}{E - E_n^{(l_c)}} \quad (2.28)$$

where the *RSE* propagator contains an infinite tower of *s*-channel bare $q\bar{q}$ states, corresponding to the spectrum of an, in principle, arbitrary confining potential. Here, $E_n^{(l_c)}$ is the discrete energy of the n -th recurrency in the bare $q\bar{q}$ channel with orbital angular momentum l_c and spin S , and $g_{nl_c S}^i$ is the corresponding coupling to the i -th meson-meson channel. Furthermore, in Eq. (2.27), λ is an overall coupling, and $j_{L_i}^i(p_i)$ and p_i are the L_i -th order spherical Bessel function and the (relativistically defined) off-shell relative momentum in meson-meson channel i , respectively. The spherical Bessel function originates in our string-breaking picture of OZI-allowed decay, being just the Fourier transform of a spherical delta function of radius a ; see Eqs. (2.19) and (2.20). Together with the overall coupling constant λ , the radius a is a freely adjustable parameter here, though its range of allowed values turns out to be quite limited in practice. Because of the separable form of the effective meson-meson interaction in Eq. (2.27), the fully off-shell T -matrix can be solved in closed form with straightforward algebra, resulting in the expression

$$T_{ij}^{L_i, L_j}(p_i, p'_j; E) = -2a\lambda^2 \sqrt{\mu_i p_i} j_{L_i}^i(p_i a) \sum_{m=1}^N \mathcal{R}_{im} \{ [\mathbb{1} - \Omega \mathcal{R}]^{-1} \}_{mj} j_{L_j}^j(p'_j a) \sqrt{\mu_j p'_j}, \quad (2.29)$$

with

$$\Omega_{ij}(k_j) = -2ia\lambda^2 \mu_j k_j j_{L_j}^j(k_j a) h_{L_j}^{(1)j}(k_j a) \delta_{ij}, \quad (2.30)$$

where $h_{L_j}^{(1)j}(k_j a)$ is the spherical Hankel function of the first kind, k_j and μ_j are the on-shell relative momentum and reduced mass in meson-meson channel j , respectively, and the matrix $\mathcal{R}(E)$ is given by Eq. (2.28).

Although in principle any confinement potential can be employed for the spectrum of the $q\bar{q}$ states, in practical applications of RSE, a harmonic oscillator (HO) with constant frequency has been used, with excellent results. For more details and further references, see Refs. [41]-[46]. Therefore, it is used in all cases here as well. The HO spectrum is given by

$$E_n = m_q + m_{\bar{q}} + \omega(2n + l_c + 3/2), \quad n = 0, 1, 2, \dots, \quad (2.31)$$

where a constant frequency of ω is used, a value fixed long ago [47]. Both ω and the constituent quark masses, *ibid.*, are defined in Eq. (2.32), where $n = u, d$.

$$\begin{aligned}\omega &= 190 \text{ MeV}, \\ m_n &= 406 \text{ MeV}, \\ m_s &= 508 \text{ MeV}, \\ m_c &= 1562 \text{ MeV}.\end{aligned}\tag{2.32}$$

Relative Couplings

The relative couplings g_{nl_cS} in Eq. (2.28) are computed in accordance with the 3P_0 model for quark-pair creation and the OZI rule, using the formalism of Ref. [48], based on overlaps of HO wave functions. These values were computed by Eef van Beveren in the $SU(3)$ flavor basis and angular momentum basis, with three-meson vertices, and are listed in Ref. [49] for several cases. As the n -dependence may be written as $g_n^2 = r_n^2/4^n$, where r_n is a polynomial with degree below 4 for the lowest angular excitations, in practice convergence of the series is achieved by truncating it after 20 terms.

2.2.1 Redefining the S -matrix

It is straightforward to show that the S -matrix $S(E) \equiv \mathbb{1} + 2iT(E)$ (cf. Eq. (2.17)), where $T(E)$ is the on-energy-shell restriction of the multichannel T -matrix in Eqs. (2.28)–(2.30), is unitary and symmetric, when limited to open channels and real energies. However, it is also easy to see that, for complex masses and so complex relative momenta, the unitarity of S is lost, though not its symmetry. The latter property can be used to redefine the physical S -matrix.

Since S is always a symmetrix matrix, it can be decomposed, via Takagi [50] factorization, as

$$S = VDV^T, \tag{2.33}$$

where V is unitary and D is a real nonnegative diagonal matrix. Then we get

$$S^\dagger S = (V^T)^\dagger DV^\dagger VDV^T = (V^T)^\dagger D^2 V^T = U^\dagger D^2 U, \tag{2.34}$$

where we have defined $U \equiv V^T$, also unitary. So the diagonal elements of $D = \sqrt{US^\dagger SU^\dagger}$ are the square roots of the eigenvalues of the positive Hermitian matrix $S^\dagger S$, which are all real and nonnegative. Moreover, since $S = \mathbb{1} + 2iT$ is manifestly

nonsingular, the eigenvalues of $S^\dagger S$ are even all nonzero and U is unique. Thus, we may define

$$S' \equiv SU^\dagger D^{-1}U. \quad (2.35)$$

Then, using Eq. (2.33) and $V = U^T$, we have

$$S' = U^T D U U^\dagger D^{-1}U = U^T U, \quad (2.36)$$

which is obviously symmetric and, as

$$(U^T U)^\dagger = U^\dagger (U^\dagger)^T = U^{-1} (U^{-1})^T = (U^T U)^{-1}, \quad (2.37)$$

also unitary. So S' has the required properties to be defined as the S -matrix for a scattering process with complex masses in the asymptotic states.

2.3 Two-coupled-channel Schrödinger model

The RSE approach does not allow to obtain wave functions in a straightforward fashion. Here, we resort to the equivalent [42] coordinate-space coupled-channel formalism of Ref. [51], which was used to study the influence of strong decay channels on hadronic spectra and wave functions, besides several more specific phenomenological applications.

Consider now a system composed of a confined $q\bar{q}$ channel coupled to a meson-meson channel $M_1 M_2$. Confinement is still described by Eq. (2.31). In the scattering channel, no direct interactions between the two mesons are considered, with μ_f and l_f being the reduced two-meson mass and orbital angular momenta in the free channel, respectively. Transitions between the two channels are modeled via an off-diagonal delta-shell potential with strength g , which mimics string breaking at a well-defined distance a . The corresponding Hamiltonian, transition potential, and 2×2 matrix Schrödinger equation are given in Eqs. (2.38)–(2.41), with the usual definition $u(r) = rR(r)$, where $R(r)$ is the radial wave function.

$$h_c = \frac{1}{2\mu_c} \left(-\frac{d^2}{dr^2} + \frac{l_c(l_c + 1)}{r^2} \right) + \frac{\mu_c \omega^2 r^2}{2} + m_q + m_{\bar{q}}, \quad (2.38)$$

$$h_f = \frac{1}{2\mu_f} \left(-\frac{d^2}{dr^2} + \frac{l_f(l_f + 1)}{r^2} \right) + m_{M_1} + m_{M_2}, \quad (2.39)$$

$$V = \frac{g}{2\mu_c a} \delta(r - a), \text{ cf. (2.20)} \quad (2.40)$$

$$\begin{pmatrix} h_c & V \\ V & h_f \end{pmatrix} \begin{pmatrix} u_c \\ u_f \end{pmatrix} = E \begin{pmatrix} u_c \\ u_f \end{pmatrix} . \quad (2.41)$$

Once the 1×1 S matrix (cf. Eq. (2.55)) has been constructed from the wave function, possible bound or virtual states as well as resonances can be searched for.

2.3.1 Solving the coupled-channel Schrödinger equation

We twice integrate the Schrödinger equation (2.41) in order to get two sets of boundary conditions, viz. Eqs. (2.42) and (2.43):

$$\begin{aligned} u'_c(r \uparrow a) - u'_c(r \downarrow a) + \frac{g}{a} u_f(a) &= 0 , \\ u'_f(r \uparrow a) - u'_f(r \downarrow a) + \frac{g\mu_f}{a\mu_c} u_c(a) &= 0 ; \end{aligned} \quad (2.42)$$

$$\begin{aligned} u_c(r \uparrow a) &= u_c(r \downarrow a) , \\ u_f(r \uparrow a) &= u_f(r \downarrow a) . \end{aligned} \quad (2.43)$$

A general solution to this problem is the two-component wave function given by Eqs. (2.44) and (2.45), for the confined and meson-meson channel, respectively:

$$u_c(r) = \begin{cases} A_c F_c(r) & r < a , \\ B_c G_c(r) & r > a ; \end{cases} \quad (2.44)$$

$$u_f(r) = \begin{cases} A_f J_{l_f}(kr) , & r < a , \\ B_f \left[J_{l_f}(kr) k^{2l_f+1} \cot \delta_{l_f}(E) - N_{l_f}(kr) \right] , & r > a . \end{cases} \quad (2.45)$$

In Eq. (2.44), the function $F_c(r)$ vanishes at the origin, whereas $G_c(r)$ falls off exponentially for $r \rightarrow \infty$, their explicit expressions being

$$F(r) = \frac{1}{\Gamma(l+3/2)} z^{(l+1)/2} e^{-z/2} \Phi(-\nu, l+3/2, z) , \quad (2.46)$$

$$G(r) = -\frac{1}{2\sqrt{\mu\omega}} \Gamma(-\nu) z^{(l+1)/2} e^{-z/2} \Psi(-\nu, l+3/2, z) , \quad (2.47)$$

where Φ and Ψ are the confluent hypergeometric functions of first and second kind (see Sec. 2.4), respectively, $\Gamma(-\nu)$ is the complex gamma function, ν is given by

$$\nu(E) = \frac{E - m_q - m_{\bar{q}}}{2\omega} - \frac{l_c + 3/2}{2}, \quad \text{cf. (2.31)} \quad (2.48)$$

and $z = \mu\omega r^2$. Note that only in the case of integer ν , i.e., for $g = 0$, do Φ and Ψ reduce to the usual Laguerre polynomials for the three-dimensional HO potential. Furthermore, the functions J and N in Eq. (2.45) are simple redefinitions of the standard spherical Bessel and Neumann functions, i.e., $J_l(kr) = k^{-l}r j_l(kr)$ and $N_l(kr) = k^{l+1}r n_l(kr)$. From the boundary conditions (2.42) and (2.43), as well as the wave-function expressions (2.44) and (2.45), we get, with the definition $\kappa = ka$,

$$\begin{aligned} G'_c(r)F_c(a) - F'_c(a)G_c(a) &= \frac{g}{a}J_{l_f}(\kappa)F_c(a)\frac{A_f}{B_c}, \\ J'_{l_f}(\kappa)N_{l_f}(\kappa) - J_{l_f}(\kappa)N'_{l_f}(\kappa) &= \frac{g}{a}\frac{\mu_f}{\mu_c}J_{l_f}(\kappa)F_c(a)\frac{A_c}{B_f}. \end{aligned} \quad (2.49)$$

Using now the Wronskian relations

$$\begin{aligned} W(F_c(a), G_c(a)) &\equiv F_c(a)G'_c(a) - F'_c(a)G_c(a) = 1, \\ W(N_{l_f}(\kappa), J_{l_f}(\kappa)) &\equiv N_{l_f}(\kappa)J'_{l_f}(\kappa) - N'_{l_f}(\kappa)J_{l_f}(\kappa) = -1, \end{aligned} \quad (2.50)$$

and continuity of the wave function at $r=a$ (cf. Eq. (2.43)), we can solve for three of the four unknowns A_c , B_c , A_f , and B_f . Note that Eqs. (2.42) and (2.43) are not entirely linearly independent, so that solving all four constants is not possible. This is logical, as the overall wave-function normalization does not follow from the Schrödinger equation. Expressing all in terms of A_c then yields

$$\begin{aligned} A_c, \quad A_f &= -\left[\frac{g}{a}J_{l_f}(\kappa)G_c(a)\right]^{-1}A_c, \\ B_c &= \frac{F_c(a)}{G_c(a)}A_c, \quad B_f = \frac{g}{a}\frac{\mu_f}{\mu_c}J_{l_f}(\kappa)F_c(a)A_c. \end{aligned} \quad (2.51)$$

Note that, in order to obtain the $D^0 D^{*0}$ wave function in the outer region, we must substitute $\cot \delta_{l_f}(E) = i$ in Eq. (2.45) (also see below). Finally, the normalization

constant \mathcal{N} of the total wave function is determined by computing

$$\int_0^\infty dr |u(r)|^2 = \int_0^\infty dr (u_c^2(r) + u_f^2(r)) = \mathcal{N}^2 . \quad (2.52)$$

Then, we can also calculate the root-mean-square radius $\bar{r} = \sqrt{\langle r^2 \rangle}$ of the two-component system by

$$\langle r^2 \rangle = \frac{1}{\mathcal{N}^2} \int_0^\infty dr r^2 (u_c^2(r) + u_f^2(r)) . \quad (2.53)$$

As for the S -matrix poles corresponding to resonances, bound states, or virtual bound states, $\cot \delta_{l_f}(E)$ can be solved from continuity of $u_f(r)$ at $r=a$ in Eq. (2.45), resulting in the expression

$$\cot \delta_{l_f}(E) = - \left[g^2 \frac{\mu_f}{\mu_c} k j_{l_f}^2(\kappa) F_c(a) G_c(a) \right]^{-1} + \frac{n_{l_f}(\kappa)}{j_{l_f}(\kappa)} , \quad (2.54)$$

with the 1×1 S -matrix simply given by

$$S_{l_f}(E) = \frac{\cot \delta_{l_f}(E) + i}{\cot \delta_{l_f}(E) - i} . \quad (2.55)$$

Real or complex poles can then be searched for numerically, by using Newton's method to find the energies for which $\cot \delta_{l_f}(E) = i$, on the appropriate Riemann sheet.

2.4 Special functions, numerical methods, and kinematics

The confluent hypergeometric functions Φ and Ψ introduced in Subs. 2.3.1 are defined in Ref. [52], Eqs. (6.1.1) and (6.5.7), respectively. Thus, the function Φ is easily programmed as a rapidly converging power series, while the definition (6.5.7) of Ψ in terms of Φ and the gamma function Γ then also allows straightforward computation, by employing Gauss's multiplication formula for $\Gamma(-\nu)$ (see Ref. [53], Eq. (6.1.20)) so as to map the argument $-\nu$ to lying well inside the unit circle in the complex plane, whereafter a very fast converging power-series expansion of $1/\Gamma(-\nu)$ (see Ref. [53], Eq. (6.1.34)) can be applied.

The integrals for wave-function normalization and computation of r.m.s. radii are carried out by simple Gauss integration, choosing increasing numbers of points on a finite interval for the $c\bar{c}$ channel, and an infinite one for $D^0 D^{*0}$. Note that, in the

former case, the wave function falls off fast enough to allow convergence for a finite cutoff, whereas in the latter a suitable logarithmic mapping is used. In both cases though, because of the wave-function cusp at $r=a$ and in order to avoid numerical instabilities, the domain of integration is split into two pieces, with up to 16 Gauss points in the inner region and 64 in the outer one, thus resulting in a very high precision of the results.

Although the $X(3872)$ bound state can reasonably be considered a nonrelativistic system, we still use relativistic kinematics in the $D^0 D^{*0}$ channel, since parts of the resonance-pole trajectories involve relatively large (complex) momenta. For consistency, the same is done for all energies. The manifest unitarity of the S matrix is not affected by this choice. Thus, the relative $D^0 D^{*0}$ momentum reads

$$k(E) = \frac{E}{2} \left\{ \left[1 - \left(\frac{T}{E} \right)^2 \right] \left[1 - \left(\frac{P}{E} \right)^2 \right] \right\}^{\frac{1}{2}}, \quad (2.56)$$

where T and P are the threshold ($m_{D^{*0}} + m_{D^0}$) and pseudothreshold ($m_{D^{*0}} - m_{D^0}$) energies, respectively. The corresponding relativistic reduced mass is defined as

$$\mu_f(E) \equiv \frac{1}{2} \frac{dk^2}{dE} = \frac{E}{4} \left[1 - \left(\frac{TP}{E^2} \right)^2 \right]. \quad (2.57)$$

Note that in the $c\bar{c}$ channel the reduced mass is defined in the usual way, i.e., $\mu_c = m_c/2$, owing to the inherently nonrelativistic nature of the HO potential and the ensuing wave function.

Chapter 3

Strangeonium: ϕ 's and the $\phi(2170)$

S. Coito, G. Rupp, and E. van Beveren, *PRD* **80**, 094011 (2009).

In 2006, the BABAR Collaboration announced [54] the discovery of a new vector-meson resonance, called $X(2175)$, in the initial-state-radiation process $e^+e^- \rightarrow K^+K^-\pi\pi\gamma$, observed in the channel $\phi(1020)f_0(980)$, with the ϕ meson decaying to K^+K^- and the $f_0(980)$ to $\pi^+\pi^-$ or $\pi^0\pi^0$. Two years later, the BES Collaboration confirmed [55] this resonance, then denoted $Y(2175)$, in the decay $J/\psi \rightarrow \eta[\rightarrow \gamma\gamma]\phi[\rightarrow K^+K^-]f_0(980)[\rightarrow \pi^+\pi^-]$. At present, the new state is included in the PDG listings as the $\phi(2170)$ [39] with average mass $M = (2175 \pm 15)$ MeV and width $\Gamma = (61 \pm 18)$ MeV. However, these resonance parameters are strongly challenged by the Belle [56] results on the $Y(2175)$, alias $\phi(2170)$, observed in the process $e^+e^- \rightarrow \phi\pi^+\pi^-$, yielding $M = (2079 \pm 13_{-28}^{+79})$ MeV and $\Gamma = (192 \pm 23_{-61}^{+25})$ MeV. The observation of this highly excited ϕ -type resonance with (probably) modest width, besides the peculiar, seemingly preferential, decay mode $\phi f_0(980)$, triggered a variety of model explications, most of which proposing exotic solutions. Let us mention first a strangeonium-hybrid ($s\bar{s}g$) assignment, in the flux-tube as well as the constituent-gluon model [57], and a perturbative comparison of $\phi(2170)$ decays in these exotic ansatzes with a standard 2^3D_1 $s\bar{s}$ description from both the flux-tube and the 3P_0 model, by the same authors [58]. Other approaches in terms of exotics, with QCD sum rules, are an $ss\bar{s}\bar{s}$ tetraquark assignment [59], and an analysis [60] exploring both $ss\bar{s}\bar{s}$ and $s\bar{s}s\bar{s}$ configurations. In an effective description based on Resonance Chiral Perturbation Theory [61], the bulk of the experimental data is reproduced except for the $\phi(2170)$ peak. This then led to a 3-body Faddeev calculation [62], with the pair interactions taken from the chiral unitary approach. Indeed, a resonance with parameters reasonably close to those of the $\phi(2170)$ is thus generated, though a little bit too narrow. Finally, a review on several puzzling hadron

states [63] mentions the possibility that the $\phi(2170)$ arises from S -wave threshold effects. In this chapter, we shall study the possibility that the $\phi(2170)$ is a normal excited ϕ meson, by coupling a complete confinement spectrum of $s\bar{s}$ states to a variety of S - and P -wave two-meson channels, composed of pairs of ground-state pseudoscalar (P), vector (V), scalar (S), and axial-vector (A) mesons. The employed formalism is a multichannel generalization of the Resonance-Spectrum Expansion (RSE), Sec. 2.2, which allows for an arbitrary number of confined and scattering channels [64].

3.1 The RSE applied to ϕ recurrences

In the present investigation of strangeonium vector mesons, both the 3S_1 and 3D_1 $s\bar{s}$ confinement channels are included. We could in principle also consider deviations from ideal mixing, by coupling the corresponding two $(u\bar{u} + d\bar{d})/\sqrt{2}$ channels as well, but such fine corrections will be left for possible future studies. For the meson-meson channels, we consider the most relevant combinations of ground-state P, V, S, and A mesons that have nonvanishing coupling to either of the two confinement channels in accordance with the 3P_0 model and the OZI rule. The resulting 17 channels are listed, with all their relevant quantum numbers, in Table 3.1. For the channels containing an η or η' meson, we assume a pseudoscalar mixing angle of 37.3° , in the flavor basis, though our results are not very sensitive to the precise value. Also note that channels with the same particles but different relative orbital angular momentum L or total spin S are considered different. This is only strictly necessary for different L , because of the corresponding wave functions, but is also done when S is different, for the purpose of clarity. All relative couplings are given in Table 3.1 for the lowest recurrences ($n = 0$). As a matter of fact, we list their squares, which are rational numbers, but given as rounded floating-point numbers in the table, also for clarity's sake. For higher n values, the couplings fall off very rapidly. Their n dependence, for the various sets of decay channels, is presented in Table 3.2. The threshold values in Table 3.1 are obtained by taking the meson masses given in the PDG 2008 tables or listings [65], with the exception of the $K_0^*(800)$ (alias κ), for which we choose the real part of the pole position from Ref. [44], as it lies closer to the world average of κ masses. Note that we take sharp thresholds, even when (broad) resonances are involved. We shall come back to this point in Sec. 3.5. Finally, we should notice that a number of channels that also couple to $s\bar{s}$ vector states according to the scheme of Ref. [48], viz. P -wave channels

Channel	$g_{(l_c=0)}^2$ $\times 10^{-3}$	$g_{(l_c=2)}^2$ $\times 10^{-3}$	l_1	l_2	L	S	Threshold (MeV)
KK	27.8	9.26	0	0	1	0	987
KK^*	111	9.26	0	0	1	1	1388
$\eta\phi$	40.8	3.40	0	0	1	1	1567
$\eta'\phi$	70.3	5.86	0	0	1	1	1977
K^*K^*	9.26	3.09	0	0	1	0	1788
K^*K^*	185	0.62	0	0	1	2	1788
$\phi(1020)f_0(980)$	83.3	0	0	1	0	1	1999
$K^*K_0^*(800)$	83.3	0	0	1	0	1	1639
$\phi(1020)f_0(980)$	0	14.7	0	1	2	1	1999
$K^*K_0^*(800)$	0	14.7	0	1	2	1	1639
$\eta h_1(1380)$	10.2	5.67	0	1	0	1	1928
$\eta' h_1(1380)$	17.6	9.76	0	1	0	1	2338
$KK_1(1270)$	83.3	20.6	0	1	0	1	1764
$KK_1(1400)$	0	2.57	0	1	0	1	1894
$K^*K_1(1270)$	167	10.3	0	1	0	1	2164
$K^*K_1(1400)$	0	1.29	0	1	0	1	2294
$\phi f_1(1420)$	111	3.86	0	1	0	1	2439

Table 3.1: Included two-meson channels, their internal and relative angular momenta and spins, couplings squared for $n = 0$, and thresholds. See Ref. [65] for properties of listed mesons, except for the $K_0^*(800)$, discussed in the text.

involving axial-vector mesons as well as some channels with tensor mesons, have not been included in the final calculations presented here. However, their influence has been tested and turned out to be very modest, due to the corresponding small couplings.

Now we evaluate the on-shell components of the T -matrix defined in Eqs. (2.28),(2.29) for the channels given in Tables 3.1–3.3.

3.2 Experimental status of ϕ states

Before adjusting our two free parameters λ and a from Eq. (2.29), let us first have a look at the experimental status of vector ϕ resonances. According to the 2012 PDG listings [39], there are only 3 observed states, viz. the $\phi(1020)$, $\phi(1680)$, and $\phi(2170)$. Their PDG masses and widths are given in Table 3.4. Clearly, this is a very poor status, as several additional states must exist in the energy range 1–

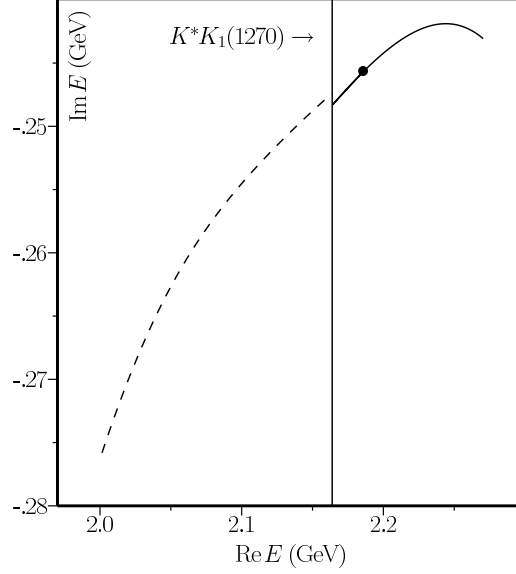


Figure 3.1: Trajectory of first continuum pole, for $2.26 \leq \lambda \leq 5.99$ ($\text{GeV}^{-3/2}$), from left to right. Bullet represents $\lambda = 4 \text{ GeV}^{-3/2}$, while dashed line indicates unphysical Riemann sheet.

2 GeV according to the quark model, and also if we compare with e.g. observed ρ resonances [65] in the same energy interval. Moreover, the $\phi(1680)$ can hardly be the first radial excitation of the $\phi(1020)$, in view of the well established $K^*(1410)$, which is almost 300 MeV lighter, and a typical mass difference of 100–150 MeV between the strange and nonstrange (u, d) constituent quarks [47, 66]. This conclusion is further supported if indeed the $\rho(1250)$ is confirmed as the first radial recurrence of the $\rho(770)$ [67, 47]. So the $\phi(1680)$ is more likely to be the 1^3D_1 state, with a hitherto undetected 2^3S_1 state somewhere in the mass range 1.5–1.6 GeV. As a matter of fact, in Ref. [68] a vector ϕ resonance was reported at roughly 1.5 GeV, though this observation is, surprisingly, included under the $\phi(1680)$ entry [65]. Even more oddly, another ϕ -like state, at ~ 1.9 GeV and reported in the same paper [68], is *also* included under the $\phi(1680)$ [65]. However, a resonance at about 1.9 GeV should be a good candidate for the next radial $s\bar{s}$ recurrence, if we take the observed ρ resonances in Ref. [67] for granted.

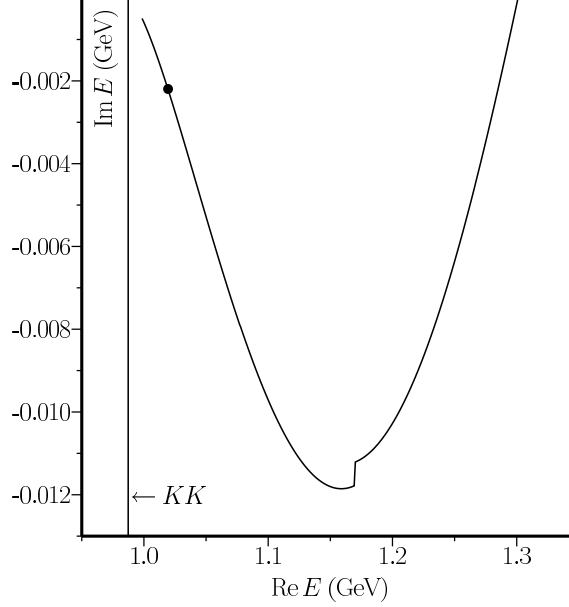


Figure 3.2: 1^3S_1 confinement pole for $4.31 \geq \lambda \geq 0$ ($\text{GeV}^{-3/2}$). Bullet represents $\lambda = 4 \text{ GeV}^{-3/2}$.

Channel	$\tilde{g}_{(l_c=0,n)}^2 \times 4^n$	$\tilde{g}_{(l_c=2,n)}^2 \times 4^n$
PP	$(2n+3)/3$	$n+1$
PV	$(2n+3)/3$	$n+1$
VV	$(2n+3)/3$	$n+1$
SV	$(2n-3)^2/9$	$(n+1)(2n+5)/5$
PA	$(2n-3)^2/9$	$(n+1)(2n+5)/5$
VA	$(2n-3)^2/9$	$(n+1)^2$

Table 3.2: Dependence of couplings squared on recurrency n .

3.3 Hunting after poles

In view of the poor status of excited ϕ states, let us adjust our parameters λ and a to the mass and width of the $\phi(1020)$. Here, we should mention that an additional phenomenological ingredient of our model is an extra suppression of subthreshold contributions, using a form factor, on top of the natural damping due to the spherical Bessel and Hankel functions in Eq. (2.28). Such a procedure is common practice in multichannel phase-shift analyses. Thus, for closed meson-meson channels we make the substitution

$$(g_{(l_c,n)}^i)^2 \rightarrow (g_{(l_c,n)}^i)^2 e^{\alpha k_i^2} \quad \text{for} \quad \Re k_i^2 < 0. \quad (3.1)$$

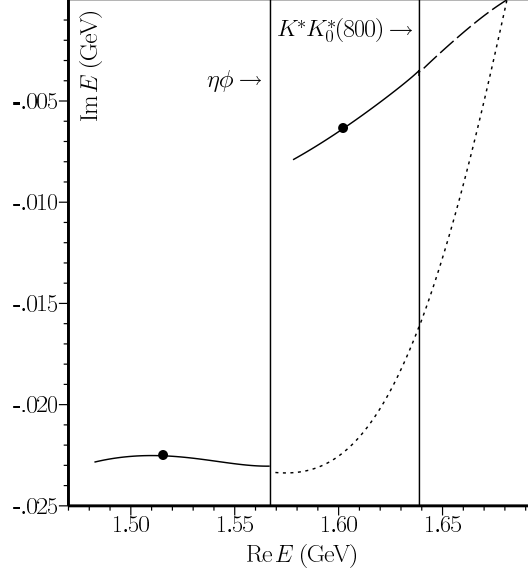


Figure 3.3: 2^3S_1 (lower) and 1^3D_1 (upper) confinement poles for $5.0 \geq \lambda \geq 0$ ($\text{GeV}^{-3/2}$) and $4.76 \geq \lambda \geq 0$ ($\text{GeV}^{-3/2}$), respectively. Bullets represent $\lambda = 4 \text{ GeV}^{-3/2}$, while dotted and dashed lines indicate unphysical Riemann sheets.

The parameter α is chosen at exactly the same value as in previous work [44, 46], viz. $\alpha = 4 \text{ GeV}^{-2}$.

Choosing now $\lambda = 4$ and $a = 4 \text{ GeV}^{-1}$, we manage to reproduce mass and width of the $\phi(1020)$ with remarkable accuracy, namely $M_\phi = 1019.5 \text{ MeV}$ and $\Gamma_\phi = 4.4 \text{ MeV}$. Note that these values of λ and a are of the same order of magnitude as in the work mentioned before [44, 46], which dealt with scalar mesons.

In Table 3.5 we collect all resonance poles encountered on the respective physical Riemann sheets, which correspond to $\Im m k_i > 0$ for closed channels and $\Im m k_i < 0$ for open ones. When the latter conditions are not fulfilled, we call the correspond-

n	$l_c = 0$	$l_c = 2$
0	1301	1681
1	1681	2061
2	2061	2441
3	2441	2821

Table 3.3: Masses of bare $s\bar{s}$ states in MeV, for HO potential with $\omega = 190 \text{ MeV}$ and $m_s = 508 \text{ MeV}$ (see Eqs. (2.31) and (2.32)).

	M (MeV)	Γ (MeV)
$\phi(1020)$	1019.455 ± 0.020	4.26 ± 0.04
$\phi(1680)$	1680 ± 20	150 ± 50
$\phi(2170)$	2175 ± 15	61 ± 18

Table 3.4: Listed $J^{PC} = 1^{--}$ ϕ resonances, with masses and widths [65] (values for $\phi(1680)$ are estimates [65]).

ing Riemann sheets unphysical. Moreover, we also show here the pole positions obtained by taking only the 3S_1 $s\bar{s}$ channel and switching off the 3D_1 , for fixed λ and a . Focusing for the moment on those poles that originate in the states of the

Pole	3S_1 only		$^3S_1 + ^3D_1$		Type of Pole
	\Re	\Im	\Re	\Im	
1	1027.5	-2.7	1019.5	-2.2	conf., $n = 0, 1 \ ^3S_1$
2	1537	-13	1516	-23	conf., $n = 1, 2 \ ^3S_1$
3	-	-	1602	-6	conf., $n = 0, 1 \ ^3D_1$
4	1998	-16	1932	-24	conf. $n = 2, 3 \ ^3S_1$
5	-	-	1996	-14	conf. $n = 1, 2 \ ^3D_1$
6	2397	-214	2186	-246	continuum
7	2415	-6	2371	-29	conf., $n = 3, 4 \ ^3S_1$
8	-	-	2415	-8	conf., $n = 2, 3 \ ^3D_1$
9	2.501	-236	2551	-193	continuum

Table 3.5: Complex-energy poles in MeV, for 3S_1 $s\bar{s}$ channel only, and for both 3S_1 and 3D_1 . See text for further details.

confinement spectrum (indicated by “conf.” in the table), we see good candidates for the resonances at ~ 1.5 GeV and ~ 1.9 GeV reported in Ref. [68], and possibly also for the $\phi(1680)$, though our $1 \ ^3D_1$ state seems somewhat too light. Note, however, that under the $\phi(1680)$ entry [65] in the PDG listings there is a relatively recent observation [69] with a mass of (1623 ± 20) MeV, which is compatible with our pole at 1602 MeV. Furthermore, the imaginary parts of the confinement poles are generally too small, except for the $\phi(1020)$. We shall come back to this point in the conclusions below. Besides the latter poles, also two so-called *continuum* poles are found, often designated as *dynamical* poles, the most conspicuous of which is the one at $(2186 - i246)$ MeV, as the real part is very close to the mass of the $\phi(2170)$ as measured by BABAR [54] and BES [55]. However, in view of the much too large width, even as compared to the Belle [56] value, considerable caution is urged. Also this point will be further discussed in the conclusions.

Some words are in place here about our identification of the 3S_1 and 3D_1 confine-

ment poles in Table 3.5. The point is that, rigorously speaking, these designations only make sense for pure confinement states and, moreover, without any ${}^3S_1 / {}^3D_1$ mixing. Now, in our approach, the very mixing is provided by the coupling to common decay channels. So for any nonvanishing value of the overall coupling λ there are no longer pure 3S_1 and 3D_1 states, while for the physical value of λ the mixing is probably considerable. Moreover, there is no obvious way to tell which pole of a pair originating in a degenerate confinement state stems from either 3S_1 or 3D_1 . Therefore, our identification is partly based on the couplings in Table 3.1, which on the whole suggest larger shifts for 3S_1 than for 3D_1 , partly on a comparison with a perturbative approach employed in Ref. [70] to find poles for small λ .

The designation *continuum* pole becomes clear when plotting a corresponding trajectory as a function of the overall coupling λ . In Fig. 3.1, the first such pole is shown to have an *increasingly* large imaginary part for *decreasing* λ , eventually disappearing in the continuum for $\lambda \rightarrow 0$. Turning now to the $\phi(2170)$ energy region,

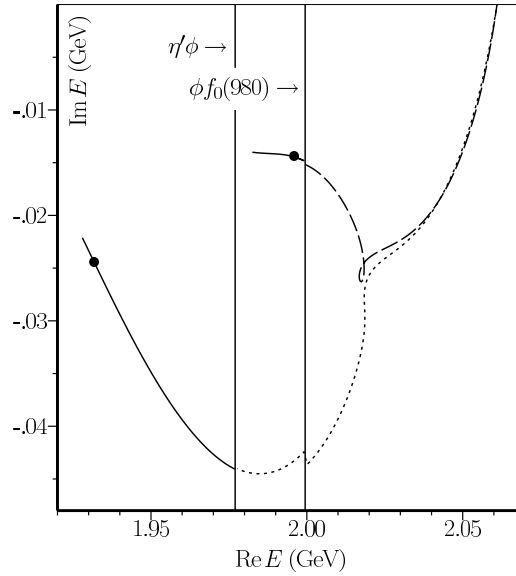


Figure 3.4: $3 {}^3S_1$ (lower) and $2 {}^3D_1$ (upper) confinement poles for $4.2 \geq \lambda \geq 0$ ($\text{GeV}^{-3/2}$) and $5.99 \geq \lambda \geq 0$ ($\text{GeV}^{-3/2}$), respectively. Bullets represent $\lambda = 4 \text{ GeV}^{-3/2}$, while dotted and dashed lines indicate unphysical Riemann sheets.

we show in Fig. 3.6 the elastic S - and D -wave. Note that the small jump at the important S -wave $K^* K_1(1270)$ threshold is due to a minor threshold discontinuity of the damping function in Eq. (3.1) for complex momenta. Figure 3.2 shows a

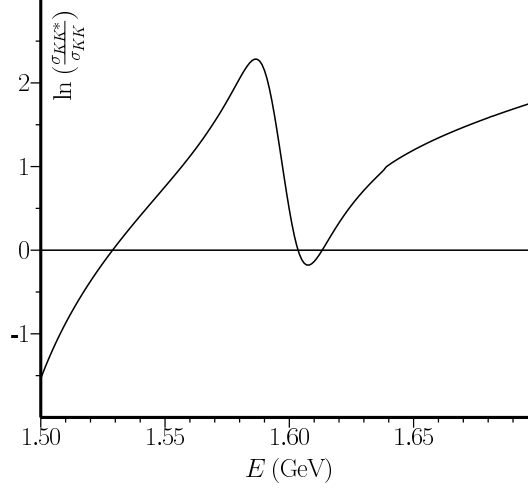


Figure 3.5: Natural logarithm of the ratio of the elastic KK^* and KK cross sections.

similar trajectory, but now for the lowest confinement pole, which ends up as the $\phi(1020)$ resonance. Notice the large negative mass shift (≈ 280 MeV), as well as the way the pole approaches the $K\bar{K}$ threshold, which is typical for P -wave decay channels. Also note that the tiny jump in the trajectory is due to the way relativistic reduced mass is defined below threshold, which in the case of closed channels with highly unequal masses ($KK_1(1270)$ here) requires an intervention to prevent the reduced mass from becoming negative. In Fig. 3.3, we depict the trajectories of the 2^3S_1 and 1^3D_1 confinement poles. Note that the coupling to decay channels lifts the original degeneracy of the 2^3S_1 and 1^3D_1 HO states. The trajectories of the next pair of confinement poles, i.e., 3^3S_1 and 2^3D_1 , are drawn in Fig. 3.4. Note the highly nonlinear behavior of the poles, showing the unreliability of perturbative methods to estimate coupled-channel effects.

3.4 Cross sections

Now we shall show, as mere illustrations, some of the cross sections related to the resonance poles found in the preceding section. In Fig. 3.8, the elastic P -wave KK cross section is depicted in the energy region covering the $\phi(1020)$ as well as the 2^3S_1 and 1^3D_1 resonances. We see that including the 3D_1 $s\bar{s}$ channel has the effect of lowering the 2^3S_1 state, besides the generation of an additional resonance, of course.

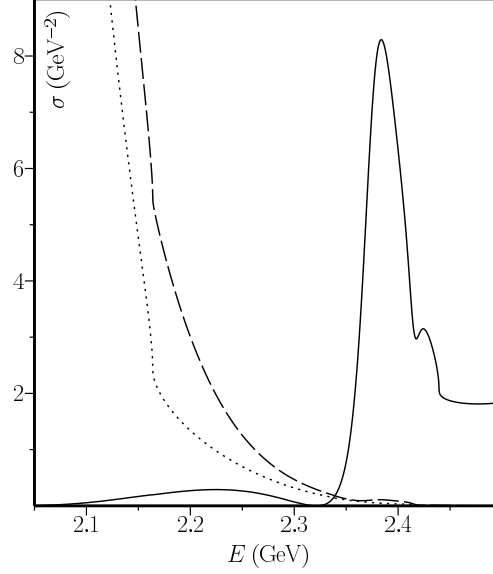


Figure 3.6: Elastic D -wave (solid line) and S -wave (dashed line) $\phi(1020)f_0(980)$ cross section. Dotted line: S -wave cross section for 3S_1 channel only.

This “repulsion” between the 3S_1 and 3D_1 poles is also noticed for the $3{}^3S_1$ and $2{}^3D_1$ states.

Figure 3.5 shows the relative importance of the KK and KK^* channels in the energy interval 1.5–1.7 GeV, which should be relevant for the $\phi(1680)$. The plotted quantity is the logarithm of the ratio of the elastic KK^* and KK cross sections, which shows that the KK^* channel is strongly dominant, except at low energies, because of phase space, and close to the pole at ~ 1.6 GeV, where the two cross sections are comparable. Dominance of the KK^* decay mode is reported under the $\phi(1680)$ PDG entry [65]. $\phi(1020)f_0(980)$ cross sections. The effect of the continuum pole at $(2186 - i246)$ MeV is noticeable as a small and very broad enhancement in the D -wave cross section. In the S -wave case, its effect is completely overwhelmed by the huge cross section at threshold, partly due to the $3{}^3S_1$ pole not far below. Also quite conspicuous are the here predicted $4{}^3S_1$ and $3{}^3D_1$ resonances (see Table 3.5 for the respective pole positions). Of course, all these model *elastic* cross sections have little direct bearing upon the experimentally observed *production* cross sections. The production process of the $\phi(2170)$ may be studied with the RSE production formalism [71], but that lies outside the scope of the present investigation,

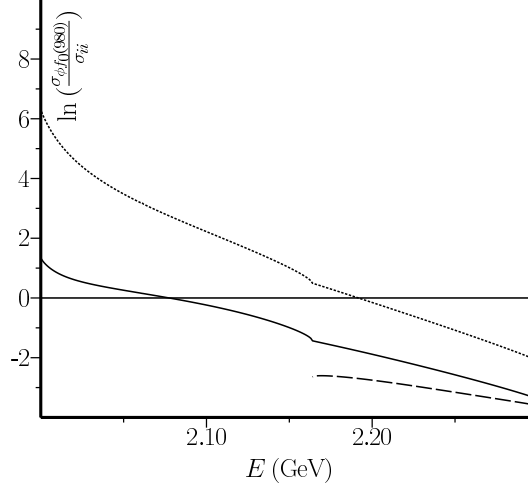


Figure 3.7: Natural logarithm of the ratios of the elastic S -wave $\phi(1020)f_0(980)$ cross section and the elastic K^*K^* (solid line), $\phi(1020)\eta'$ (dotted line), and $K^*K_1(1270)$ (dashed line) cross sections.

which focused on the possibility of generating a $\phi(2170)$ resonance pole through coupled channels.

Finally, in Fig. 3.7 we plot the logarithm of the ratios of the elastic S -wave $\phi(1020)f_0(980)$ cross section and the elastic K^*K^* , $\phi(1020)\eta'$, and $K^*K_1(1270)$ cross sections, in the energy interval 2.0–2.3 GeV. We see that the S -wave $\phi(1020)f_0(980)$ cross section dominates up to about 2.08 GeV, but getting overwhelmed first by the (P -wave) K^*K^* channel, and then even more so by the S -wave $K^*K_1(1270)$ channel, right from its threshold at ≈ 2.16 GeV upwards. Also the $\phi(1020)\eta'$ channel is becoming more important here. As for the K^*K^* channel, it gives rise to a final state with two kaons and two pions, i.e., the same as that for which the $\phi(2170)$ was observed. So the experimental status of the $\phi(2170)$ might be improved if one succeeded in identifying and isolating the $K^*[\rightarrow K\pi]K^*[\rightarrow K\pi]$ decay mode, which should be quite important.

3.5 Summary and conclusions

In this chapter, we have applied the RSE formalism for non-exotic multichannel meson-meson scattering to calculate the resonance spectrum of excited vector ϕ mesons, and to find out whether this way the $\phi(2170)$ can be generated. The in-

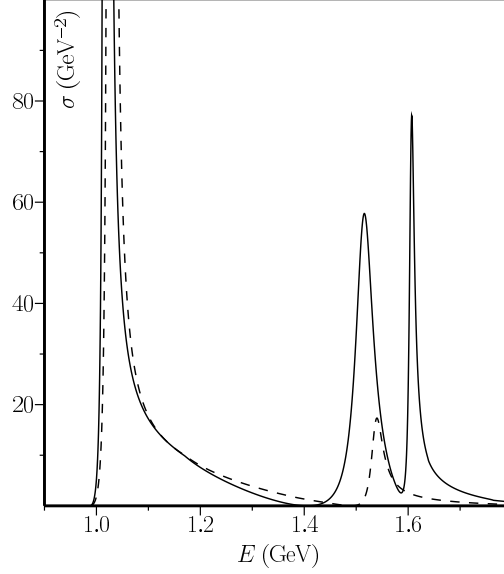


Figure 3.8: Elastic P -wave KK cross section. Full line: both 3S_1 and 3D_1 $s\bar{s}$ channels included; dashed line: only 3S_1 .

clusion of all relevant two-meson channels that couple to the bare 3S_1 and 3D_1 $s\bar{s}$ states should guarantee a reasonable description. Thus, several vector ϕ resonances are predicted, some of which are good candidates for observed states, while others may correspond to others, undetected so far, but quite plausible in view of observed partner states in the excited ρ spectrum. Finally, a very broad ϕ -like resonance pole of a dynamical origin is found, with real part very close to that of the $\phi(2170)$, but a much too large imaginary part, so that its interpretation remains uncertain. On the other hand, the calculated resonances originating in the confinement spectrum are generally too narrow.

These considerations bring us to the main problem of our description, namely the inclusion of sharp thresholds only. The point is that many of the channels in Table 3.1 involve highly unstable particles, several of which are broad to very broad resonances themselves. Treating the corresponding thresholds as sharp is clearly an approximation. In particular, the $f_0(980)$ meson included in the $\phi(1020)f_0(980)$ channels is a very pronounced resonance in the coupled $\pi\pi$ - KK system. This feature is crucial in the three-body calculation of the $\phi(2170)$ in Ref. [62], which indeed produces a clear resonance signal at almost the right energy, and even with a some-

what too *small* width. We believe that in our approach, too, a narrower $\phi(2170)$ might be generated, if we could account for the physical width of the $f_0(980)$ meson, and also for the widths of the K^* and $K_1(1270)$ resonances in the here included $K^*K_1(1270)$ channel. The reason is that the widths effectively cause these channels to act already below their central thresholds, which will strongly influence poles just underneath. Especially the width of very strongly coupling $K^*K_1(1270)$ channel, whose threshold lies only some 25 MeV below the real part of the continuum pole at $(2186 - i \times 246)$ MeV, will surely have a very significant effect on this pole's trajectory. Because of the typical behavior of continuum poles, with decreasing width for increasing coupling, we expect that the width of our $\phi(2170)$ candidate may thus be reduced. Conversely, including the widths of final-state resonances will probably *increase* the widths of the now too narrow excited ϕ resonances stemming from the confinement spectrum.

To account for the nonvanishing widths of mesons in the coupled channels is a very difficult problem, since the simple substitution of the here used real masses by the true complex masses will destroy the manifest unitarity of the S -matrix.

Chapter 4

Axials with open-charm

S. Coito, G. Rupp, and E. van Beveren, *PRD* **84**, 094020 (2011).

The axial-vector (AV) charmed mesons $D_1(2420)$ and $D_{s1}(2536)$ [39] have the puzzling feature that their decay widths are much smaller than one would expect on the basis of their principal S -wave decay modes. Namely, the $D_1(2420)$ decays to $D^*\pi$ (possibly also in a D wave), with a phase space of more than 270 MeV, but has a total width of only 20–30 MeV [39, 72]. On the other hand, the $D_{s1}(2536)$ decays to D^*K in S and D wave with a phase space of about 30 MeV, resulting in an unknown tiny width <2.3 MeV, limited by the experimental resolution [39]. The discovery of the missing two AV charmed mesons, namely the very narrow $D_{s1}(2460)$ and the very broad $D_1(2430)$, first observed by CLEO [73] and Belle [74], respectively, completed an even more confusing picture. While the tiny width of the $D_{s1}(2460)$ can be easily understood, since this meson lies underneath its lowest Okubo-Zweig-Iizuka-allowed (OZIA) and isospin-conserving decay threshold, the huge $D_1(2430)$ width, in $D^*\pi$, is in sharp contrast with that of the $D_1(2420)$. Moreover, the $D_{s1}(2460)$ lies 76 MeV below the $D_{s1}(2536)$, whereas the $D_1(2420)$ and $D_1(2430)$ are almost degenerate in mass, if one takes the central value of the latter resonance.

Quark potential models, with standard spin-orbit splittings, fail dramatically in reproducing this pattern of masses. For instance, in the relativized quark model [21] the $c\bar{s}$ state that is mainly 3P_1 comes out at 2.57 GeV, assuming the already then well-established $D_{s1}(2536)$ to be mostly 1P_1 , though with a very large mixing between 3P_1 and 1P_1 . Reference [21] similarly predicted a too high mass for the dominantly 3P_1 state in the $c\bar{q}$ ($q = u, d$) sector, viz. 2.49 GeV. In the chiral quark model for heavy-light systems of Ref. [75], the result for the mainly 3P_1 $c\bar{q}$ state is also 2.49 GeV, while the discrepancy is even worse in the $c\bar{s}$ sector, with a prediction of 2.605 GeV for the mostly 3P_1 state, now with a small mixing in both sectors.

More recently and after the discovery of the $D_{s1}(2460)$ (and $D_1(2430)$), chiral Lagrangians for heavy-light systems (see e.g. Refs. [76, 77, 78, 79]) have been employed in order to understand the masses of the AV charmed mesons, in particular the mass splittings with respect to the vector (V) mesons with charm D_s^* and D^* , respectively. Reference [77] analyzed in detail the curious experimental [80] observation that the AV-V mass difference is considerably larger in the charm-nonstrange sector than in the charm-strange one, which is not predicted by typical quark potential models [21, 75]. The same discrepancy applies to the scalar-pseudoscalar mass difference in either sector [80, 77]. In Ref. [77], the problem was tackled by calculating chiral loop corrections, but the result turned out to be exactly the opposite of what is needed to remove or alleviate the discrepancy.

An alternative approach to the AV charmed mesons is by trying to generate them as dynamical resonances in chiral unitary theory [81]. Indeed, in the latter paper, describing AV mesons in other flavor sectors as well, several charmed resonances were predicted, including the $D_1(2420)$, $D_1(2430)$, $D_{s1}(2536)$, and $D_{s1}(2460)$, with reasonable results, though the $c\bar{q}$ states came out about 100 MeV off. However, dynamical generation of mesonic resonances, including the ones that are commonly thought to be of a normal quark-antiquark type, may give rise to interpretational difficulties, besides predicting several genuinely exotic and so far unobserved states [81]. Dynamically generated AV charmed as well as bottom mesons can be found in Ref. [82], too.

Finally, in Ref. [83] a coupled-channel calculation of positive-parity $c\bar{s}$ and $b\bar{s}$ was carried out in a chiral quark model, similar to our approach in its philosophy, and with results for the $D_{s1}(2536)$ and $D_{s1}(2460)$ close to the present ones.

4.1 OZI-allowed channels for AV charmed mesons

In order to account for the two possible spectroscopic channels 3P_1 and 1P_1 contributing to a $J^P = 1^+$ state with undefined C -parity, we couple both $q\bar{q}$ channels to the most important meson-meson channels. Now we describe the physical AV charmed resonances by coupling bare 3P_1 and 1P_1 $c\bar{n}$, $c\bar{s}$ channels to all OZI-allowed ground-state pseudoscalar-vector (PV) and vector-vector (VV) channels. It is true that there are also relevant pseudoscalar-scalar (PS) channels (in P -wave), most notably $Df_0(600)$ and $D_0^*(2400)\pi$ [80] in the AV $c\bar{q}$ case, and $DK_0^*(800)$ for $c\bar{s}$. These will contribute to the observed [80] $D\pi\pi$ and $D\pi K$ decay modes, respectively. Although we have developed, Subsec. 2.2.1 an algebraic procedure to deal

with resonances in asymptotic states whilst preserving unitarity, the huge widths of the $D_0^*(2400)$, $f_0(600)$, and $K_0^*(800)$ resonances may lead to fine sensitivities that will tend to obscure the point we want to make, apart from the fact that there will also be nonresonant contributions to the $D\pi\pi$ and $D\pi K$ final states. So we restrict ourselves to the open and closed PV and VV channels in the present investigation, but we shall further discuss this issue below. The here included channels for $c\bar{q}$ and $c\bar{s}$ are given in Tables 4.1 and 4.2, respectively, together with the corresponding orbital angular momenta, threshold energies, and ground-state couplings squared $(\tilde{g}_{(S=1(0),n=0)}^i)^2$, where $S = 1(0)$ refers to the 3P_1 (1P_1) quark-antiquark component.

In Sec. 4.3, we show in more detail how the ground-state coupling constants in

Channel	$(\tilde{g}_{(S=1,n=0)}^i)^2$	$(\tilde{g}_{(S=0,n=0)}^i)^2$	L	Threshold
$D^*\pi$	0.02778	0.01389	0	2146
$D^*\pi$	0.03472	0.06944	2	2146
$D^*\eta$	0.00524	0.00262	0	2556
$D^*\eta$	0.00655	0.01310	2	2556
D_s^*K	0.01852	0.00926	0	2608
D_s^*K	0.02315	0.04630	2	2608
$D\rho$	0.02778	0.01389	0	2643
$D\rho$	0.03472	0.06944	2	2643
$D\omega$	0.00926	0.00463	0	2650
$D\omega$	0.01157	0.02315	2	2650
$D^*\rho$	0	0.01389	0	2784
$D^*\rho$	0.01042	0.06944	2	2784
$D^*\omega$	0	0.00463	0	2791
$D^*\omega$	0.03472	0.02315	2	2791
K^*	0.01852	0.00926	0	2862
K^*	0.02315	0.04630	2	2862
$D^*\eta'$	0.00402	0.00201	0	2996
$D^*\eta'$	0.00502	0.01004	2	2996
$D_s^*K^*$	0	0.00926	0	3006
$D_s^*K^*$	0.06944	0.04630	2	3006

Table 4.1: Included meson-meson channels for $D_1(2420)$ and $D_1(2430)$, with ground-state couplings squared, Sec. 2.2, orbital angular momenta, and thresholds in MeV. For η and η' , a pseudoscalar mixing angle of 37.3° is used, as in Chapter. 3.

Tables 4.1 and 4.2 depend on the isospin and J^{PC} quantum numbers of the various meson-meson channels. The latter squared couplings must be multiplied by $(n+1)/4^n$ for $L = 0$ and by $(2n/5+1)/4^n$ for $L = 2$, so as to obtain the couplings for the radial recurrences n in the RSE sum of Eq. (2.28). A subthreshold suppres-

Channel	$\left(\tilde{g}_{(S=1,n=0)}^i\right)^2$	$\left(\tilde{g}_{(S=0,n=0)}^i\right)^2$	L	Threshold
D^*K	0.03704	0.01852	0	2504
D^*K	0.04630	0.09259	2	2504
$D_s^*\eta$	0.00803	0.00402	0	2660
$D_s^*\eta$	0.01004	0.02009	2	2660
DK^*	0.03704	0.01852	0	2761
DK^*	0.04630	0.09259	2	2761
D^*K^*	0	0.01852	0	2902
D^*K^*	0.01389	0.09259	2	2902
ϕ	0.01852	0.00926	0	2988
ϕ	0.02315	0.04630	2	2988
$D_s^*\eta'$	0.01048	0.00524	0	3069
$D_s^*\eta'$	0.01310	0.02621	2	3069
$D_s^*\phi$	0	0.00926	0	3132
$D_s^*\phi$	0.06944	0.04630	2	3132

Table 4.2: As Table 4.1, but now for $D_{s1}(2536)$ and $D_{s1}(2460)$.

sion of closed channels is used just as in Eq. (3.1).

The energies of the bare AV $c\bar{n}$ and $c\bar{s}$ states we determine from Eqs. (2.31) and (2.32). This yields masses of 2443 MeV and 2545 MeV for the bare AV $c\bar{n}$ and $c\bar{s}$ states, respectively, which are very close to values found in typical single-channel quark models [21, 75].

4.2 Quasi-bound states in the continuum and other poles

Next we search for poles in the S matrix. Starting with the $c\bar{n}$ case, we choose r in the range $3.2\text{--}3.5\text{ GeV}^{-1}$ ($0.64\text{--}0.70\text{ fm}$), which is in between the values of 2.0 GeV^{-1} for an AV $c\bar{c}$ system, Chapter 5, and 4.0 GeV^{-1} for vector $s\bar{s}$ states, Chapter 3. In Fig. 4.1, we plot several pole trajectories in the complex E plane as a function of the overall coupling λ . We see that this pole rapidly acquires a large imaginary part, whereas the real part changes considerably less, especially in the range $r_0 = 3.3\text{--}3.5\text{ GeV}^{-1}$, making it a good candidate for the broad $D_1(2430)$ resonance. For $\lambda = 1.30$ and $r_0 = 3.40\text{ GeV}^{-1}$, the pole comes out at $(2430 - i \times 191)\text{ MeV}$, being thus fine-tuned to the experimental mass and width [80]. However, there should be another pole in the S matrix, since there are 2 quark-antiquark channels and more than 2 MM channels. From the structure of the T -matrix in Eqs. (2.28–2.30), one can algebraically show that the number of poles for each bare state is equal

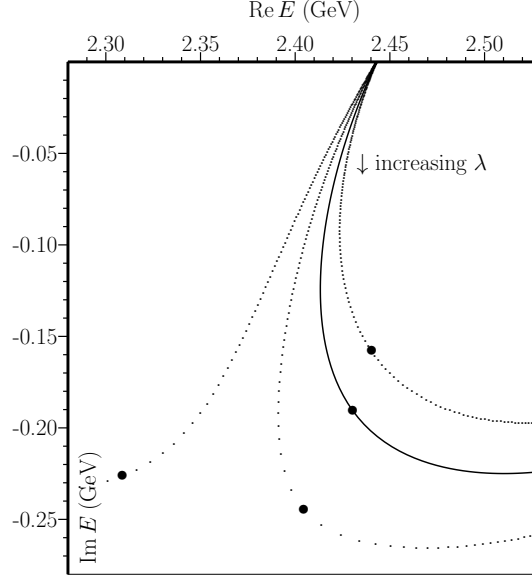


Figure 4.1: $D_1(2430)$ pole trajectories as a function of λ , for $r_0 = 3.2\text{--}3.5 \text{ GeV}^{-1}$ (left to right). Solid curve and bullets correspond to $r_0 = 3.40 \text{ GeV}^{-1}$ and $\lambda = 1.30$, respectively.

to $\min(N_{q\bar{q}}, N_{MM})$, besides possible poles of a purely dynamical nature. Indeed, another pole originating from the bare $c\bar{q}$ state is encountered, with its trajectories depicted in Fig. 4.2. Quite remarkably, this pole moves very little, acquiring an imaginary part that is a factor 55 smaller than in the dd case, for the values $\lambda = 1.30$ and $r_0 = 3.40 \text{ GeV}^{-1}$ (see solid lines and bullets in both figures). So this resonance, with a pole position of $(2439 - i \times 3.5) \text{ MeV}$, almost decouples from the only open OZIA MM channel [84], viz. $D^*\pi$, representing a quasi-bound state in the continuum (QBSC) [82]. Moreover, it is a good candidate for the $D_1(2420)$, though its width of roughly 7 MeV is somewhat too small and its mass 16 MeV too high. These minor discrepancies may be due to the neglect of the PS channels, with broad resonances in the final states, as suggested above. Nevertheless, these encouraging results might be partly due to a fortuitous choice of the parameters λ and r_0 . Therefore, we now check the $c\bar{s}$ system, thereby scaling r_0 and λ with the square root of the reduced quark mass (see Ref. [84], Eq. (13)), so as to respect flavor independence of our equations, which yields the $c\bar{s}$ values $r_0 = 3.12 \text{ GeV}^{-1}$ and $\lambda = 1.19$. The ensuing $c\bar{s}$ pole trajectories are depicted in Fig. 4.3, but now for $r_0 = 3.12 \text{ GeV}^{-1}$ only. Thus, for $\lambda = 1.19$, the strongly coupling state comes out at 2452 MeV, i.e., only 7.5 MeV below the $D_{s1}(2460)$ mass, with a vanishing width, as the pole ends up below the lowest OZIA channel. As for the $c\bar{s}$ QBSC, it

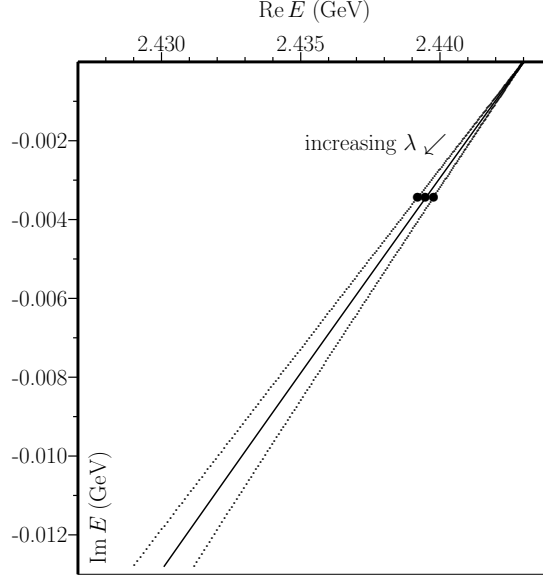


Figure 4.2: $D_1(2420)$ pole trajectories as a function of λ , for $r_0 = 3.3\text{--}3.5 \text{ GeV}^{-1}$ (left to right). Solid curve and bullets correspond to $r_0 = 3.40 \text{ GeV}^{-1}$ and $\lambda = 1.30$, respectively.

indeed shifts very little from the bare state, settling at $(2540 - i \times 0.7) \text{ MeV}$, i.e., only 5 MeV above the $D_{s1}(2536)$ mass, and having a width fully compatible with experiment [80].

Besides the above ground-state AV charmed mesons, the present model of course also predicts higher recurrences of these resonances. However, due caution is necessary so as to account for the most relevant open and closed decay channels at the relevant energy scales. Now, the first radially excited HO levels of the $^3P_1/1P_1$ $c\bar{n}$ and $c\bar{s}$ states lie at 2823 MeV and 2925 MeV, respectively, which allows the corresponding resonances to be reasonably described by the channels included in Tables 4.1, 4.2. Thus, we find again 4 poles, tabulated in Table 4.3, together with those of the ground-state AV charmed mesons. For the radially excited states, we observe a similar pattern as for the ground states, namely two poles that remain close to the bare HO levels, whereas two other poles shift considerably. Note, however, that the difference is not as dramatic as in the $n = 0$ case. This may be due to the fact that several decay channels are open now. As for a possible observation of the here predicted $2P_1$ states, no experimental candidates have been reported so far. Namely, in the nearby $c\bar{q}$ mass region, the two listed [80] resonances $D(2600)$ and $D(2750)$ [80] both decay to $D^*\pi$ and $D\pi$, which excludes an AV assignment. Concerning the $c\bar{s}$ sector, the only listed [80] state around 2.8–2.9 GeV is the

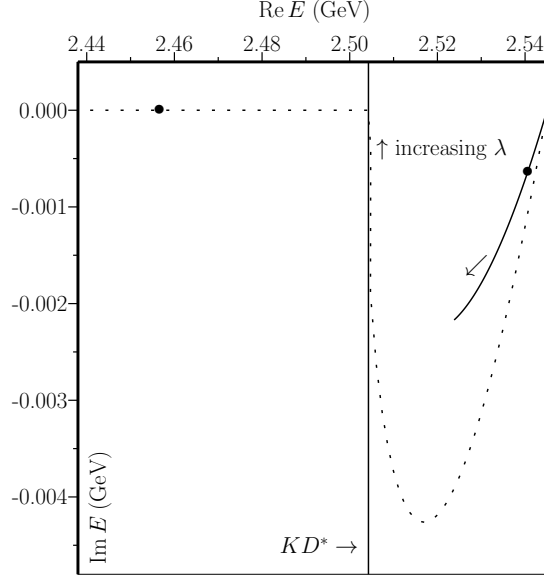


Figure 4.3: $D_{s1}(2460)$ (dashed) and $D_{s1}(2536)$ (solid) pole trajectories as a function of λ , for $r_0 = 3.12 \text{ GeV}^{-1}$. Bullets correspond to $\lambda = 1.19$; vertical line shows D^*K threshold.

$D_{sJ}^*(2860)$ [85], with natural parity and so not an AV, decaying to D^*K and DK , which makes it a good candidate for the 2^3P_2 state, possibly overlapped by the 2^3P_0 [86]. Note that the lower of our two predicted $2P_1$ resonances also practically coincides with the $D_{sJ}^*(2860)$, both in mass and width. This may be a further indication that the $D_{sJ}^*(2860)$ structure corresponds to more than one resonance only.

To conclude this section, we study — for the $c\bar{q}$ system — the dependence of the lowest-lying poles on the number of included quark-antiquark and MM channels. In Table 4.4, besides the $D_1(2420)$ and $D_1(2430)$ poles resulting from the full calculation, with the 20 MM channels from Table 4.1, we first give the pole positions for the cases that only 2 ($D^*\pi$, $L = 0, 2$) or 1 ($D^*\pi$, $L = 0$) MM channels are included. The last two poles then correspond to calculations with the full 20 MM channels but only one quark-antiquark channel, viz. 3P_1 or 1P_1 . Notice that only one pole is found when the number of quark-antiquark or MM channels is equal to 1. This confirms our above conjecture that the number of poles for each bare HO level is given by $\min(N_{q\bar{q}}, N_{MM})$.

Quark Content	Radial Excitation	Pole in MeV
$c\bar{q}$	0	$2439 - i \times 3.5$
$c\bar{q}$	0	$2430 - i \times 191$
$c\bar{s}$	0	$2540 - i \times 0.7$
$c\bar{s}$	0	$2452 - i \times 0.0$
$c\bar{q}$	1	$2814 - i \times 7.8$
$c\bar{q}$	1	$2754 - i \times 47.2$
$c\bar{s}$	1	$2915 - i \times 6.7$
$c\bar{s}$	1	$2862 - i \times 25.7$

Table 4.3: Poles of ground-state ($n = 0$) and first radially-excited ($n = 1$) AV charmed mesons. Parameters: $\lambda = 1.30$ (1.19) and $r_0 = 3.40$ (3.12) GeV^{-1} , for $c\bar{q}$ ($c\bar{s}$) states.

$c\bar{q}$ channels	MM channels	Pole 1 (MeV)	Pole 2 (MeV)
$^3P_1 + ^1P_1$	20	$2430 - i \times 191$	$2439 - i \times 3$
$^3P_1 + ^1P_1$	2	$2402 - i \times 36$	$2441 - i \times 1$
$^3P_1 + ^1P_1$	1	$2431 - i \times 39$	-
3P_1	20	$2409 - i \times 65$	-
1P_1	20	$2425 - i \times 96$	-

Table 4.4: Poles of AV $c\bar{q}$ mesons, for different sets of included channels. Parameters: $\lambda = 1.30$, $r_0 = 3.40$ GeV^{-1} .

4.3 Three-meson couplings

The ground-state couplings in Tables 4.1 and 4.2 are obtained by multiplying the isospin recouplings given in Table 4.5 with the J^{PC} couplings in Table 4.6, for an OZIA process $M_A \rightarrow M_B + M_C$, Sec. 2.2. For clarity, we represent here all couplings by rational numbers. Note that η_n and η_s in Table 4.5 stand for the pseudoscalar $I = 0$ states $(u\bar{u} + d\bar{d})/\sqrt{2}$ and $s\bar{s}$, respectively. Then, we get the couplings to the physical η and η' mesons by applying a mixing angle — in the flavor basis, see Eq. (1.1) — of 41.2° , as in Ref. [46]. For the ω and ϕ we assume ideal mixing.

M_A	M_B	M_C	g_I^2
D_{s1}	D_s, D_s^*	η_s, ϕ	1/3
D_{s1}	D, D^*	K, K^*	2/3
D_1	D_s, D_s^*	K, K^*	1/3
D_1	D, D^*	π, ρ	1/2
D_1	D, D^*	η_n, ω	1/6

Table 4.5: Squared isospin recouplings for the 3-meson process $M_A \rightarrow M_B + M_C$, with $M_A = c\bar{s}$ or $c\bar{q}$.

$J^{PC}(M_A)$	$J^{PC}(M_B)$	$J^{PC}(M_C)$	$L_{M_B M_C}$	$S_{M_B M_C}$	$g_{(n=0)}^2$
1^{++}	0^{-+}	1^{--}	0	1	1/18
1^{++}	0^{-+}	1^{--}	2	1	5/72
1^{++}	1^{--}	1^{--}	0	1	0
1^{++}	1^{--}	1^{--}	2	2	5/24
1^{+-}	0^{-+}	1^{--}	0	1	1/36
1^{+-}	0^{-+}	1^{--}	2	1	5/36
1^{+-}	1^{--}	1^{--}	0	1	1/36
1^{+-}	1^{--}	1^{--}	2	1	5/36

Table 4.6: Squared ground-state coupling constants for the 3-meson process $M_A \rightarrow M_B + M_C$, with $J^{PC}(M_A) = 1^{+\pm}$, and M_A, M_B belonging to the lowest pseudoscalar or vector nonet.

4.4 Summary and conclusions

In the foregoing, we have managed to rather accurately reproduce the masses and widths of the $D_1(2420)$, $D_1(2430)$, $D_{s1}(2536)$, and $D_{s1}(2460)$ with only 2 free parameters, one of which is already constrained by previous model calculations, as well as by reasonable estimates for the size of these mesons. Crucial is the approximate decoupling from the continuum of one combination of 3P_1 and 1P_1 components, which amounts to a mixing angle close to 35° . Namely, if we express a QBSC as $|\text{QBSC}\rangle = -\sin\theta|^3P_1\rangle + \cos\theta|^1P_1\rangle$, it decouples from the $L=0$ $D^*\pi$ channel (for $c\bar{q}$) or D^*K channel (for $c\bar{s}$), if $\theta = \arccos\sqrt{2/3} \approx 35.26^\circ$ (see Tables 4.1, 4.2). Inclusion of the other, practically all closed, channels apparently changes the picture only slightly in our formalism. This result is in full agreement with the findings in Ref. [83]. However, in the present approach this particular mixing [87] comes out as a completely dynamical result, and is not chosen by us beforehand. Moreover, the bare-mass degeneracy of 3P_1 and 1P_1 states is adequately lifted via the decay couplings in Tables 4.1 and 4.2, dispensing with the usual $\vec{S} \cdot \vec{L}$ splitting. Also note that the occurrence of (approximate) bound states in the continuum for AV charmed mesons had already been conjectured by two of us [84], based on more general arguments.

The puzzling discrepancy between the AV-V mass splittings in the $c\bar{q}$ and $c\bar{s}$ sectors is resolved in our calculation by dynamical, nonperturbative coupled-channel effects. A similar phenomenon we have observed before [43] for the $D_0^*(2300\text{--}2400)$ [80] resonance, and may be related to an effective Adler-type zero [40, 88] in the $D^*\pi$ and $D\pi$ channels in the AV and scalar $c\bar{n}$ cases, respectively, owing to the small pion mass.

Summarizing, we have reproduced the whole pattern of masses and widths of the AV charmed mesons dynamically, by coupling the most important open and closed two-meson channels to bare $c\bar{q}$ and $c\bar{s}$ states containing both 3P_1 and 1P_1 components. The dynamics of the coupled-channel equations straightforwardly leads to one pair of strongly shifted states and another pair of QBSCs. Ironically, the state that shifts most in mass, namely the $D_{s1}(2460)$, ends up as the narrowest resonance. This emphasizes the necessity [89] to deal with unquenched meson spectroscopy in a fully nonperturbative framework.

One might argue that these conclusions will depend on the specific model employed. Admittedly, our numerical results could change somewhat if slightly different bare masses for the AV charmed mesons were chosen, non- S -wave decay channels were included as well, or a different scheme was used to calculate the decreasing couplings of the higher recurrences. Nevertheless, we are convinced the bulk of our results will not change, most notably the appearance of QBSCs and the large shifts of their partner states, as the almost inevitable consequence of exact nonperturbative coupled-channel dynamics.

Chapter 5

The charmonium $X(3872)$

S. Coito, G. Rupp, and E. van Beveren, *EPJC* **71**, 1762 (2011).

The $X(3872)$ charmonium-like state was discovered in 2003 by the Belle Collaboration [90], as a $\pi^+\pi^-J/\psi$ enhancement in the decay $B^\pm \rightarrow K^\pm\pi^+\pi^-J/\psi$. The same structure was then observed, again in $\pi^+\pi^-J/\psi$, by CDF II [91], D0 [92], and BABAR [93]. Moreover, CDF [94] showed that the $\pi^+\pi^-$ mass distribution favors decays via a ρ^0 resonance, implying positive C -parity for the $X(3872)$. The $X(3872)$ has also been observed in the $\bar{D}^0 D^0 \pi^0$ and $\bar{D}^{*0} D^{*0}$ channels, by Belle [95] and BABAR [96], respectively. CDF [97] measured the $X(3872)$ mass with even higher precision, viz. $3871.61 \pm 0.16 \pm 0.19$ MeV, with a width fixed at 1.34 ± 0.64 MeV, while BABAR [98] presented evidence for the long-awaited $\omega J/\psi$ decay mode (also see Ref. [99]), and a surprising preference for the 2^{-+} assignment. At last, LHCb unequivocally determined the quantum numbers $J^{PC} = 1^{++}$, based on angular correlations in $B^\pm \rightarrow X(3872)K^\pm$ decays [100]. The $X(3872)$ resonance is listed in the 2012 PDG tables [39], with a mass of 3871.68 ± 0.17 MeV, a width < 1.2 MeV.

On the theoretical side, the first to foresee a narrow 1^{++} state close to the DD^* threshold was Törnqvist [101], arguing on the basis of strongly attractive one-pion exchange for S -wave meson-meson systems, which he called deusons. For further molecular descriptions and studies, see Ref. [102], as well as the reviews by Swanson [103] and Klempt & Zaitsev [104]. In Ref. [105], a few exotic model descriptions can be found, such as a hybrid or a tetraquark; also see the reviews [103, 104]. For further reading, we recommend the very instructive analyses by Bugg [106] and Kalashnikova & Nefediev [107]. Much more in the spirit of our own calculation is the coupled-channel analysis by Danilkin and Simonov [108], which studies resonances and level shifts of conventional charmonium states due to the most important open and closed decay channels. We shall come back to their results below.

According to the PDG 2010 [80], the $X(3872)$ could be either a 1^{++} or a 2^{-+} state, which implied 2^3P_1 or 1^1D_2 , as other radial excitations would be much too far off (see e.g. Ref. [21]). In the present chapter, we study the 1^{++} scenario, despite the conclusion by BABAR [98], the last result by the time this study was performed, from the $\omega J/\psi$ mode, that 2^{-+} was more likely. Indeed, the latter assignment appeared to be at odds with radiative-transition data [109]. For a further discussion of electromagnetic decays, see e.g. the molecular description of Ref. [110]. But more importantly, in all charmonium models we know of, the 1^1D_2 $c\bar{c}$ state lies well below 3.872 GeV, i.e., in the range 3.79–3.84 GeV (see e.g. Ref. [111]). Our own *bare* 1^1D_2 state comes out at 3.79 GeV, just as the corresponding single-channel state in Ref. [108]. Now, the crucial point is that loops from closed meson-meson channels are *always* attractive [51]. Hence, since DD^{*1} at 3.872–3.880 GeV is the lowest OZIA channel that couples to a 1^1D_2 $c\bar{c}$ state, the coupled-channel mass shift will inexorably be further downwards (also see Ref. [111]).

The present sections aims to show that the mass and width of the $X(3872)$, as well as the corresponding observed amplitudes in the $D^0 D^{*0}$, $\rho^0 J/\psi$, and $\omega J/\psi$ channels, are compatible with a description in terms of a regular 2^3P_1 charmonium state, though mass-shifted and unitarized via open and closed decay channels.

5.1 The RSE applied to charmonium 1^{++}

Sticking to the 1^{++} scenario, we employ again the RSE in order to couple one $c\bar{c}$ channel, with $l_c = 1$, to several OZIA pseudoscalar-vector (PV) and vector-vector (VV) channels, just as in our preliminary study [112] of the $X(3872)$. However, we now also couple the OZI-suppressed (OZIS) $\rho^0 J/\psi$ and $\omega J/\psi$ channels, to account for the bulk of the observed $\pi^+\pi^- J/\psi$ and $\pi^+\pi^-\pi^0 J/\psi$ decays, respectively. Although the former channel is isospin breaking as well, the extreme closeness of its central threshold at 3872.4 MeV to the $X(3872)$ structure makes it absolutely nonnegligible, despite a very small expected coupling. A complication, though, is the large ρ width, which does not allow the $\rho^0 J/\psi$ channel to be described through a sharp threshold. Effects in the $X(3872)$ from nonzero ρ and ω widths were already estimated in Ref. [113]. We tackle this problem by taking a complex mass for the ρ , from its pole position [114], and then apply the novel, empirical yet rigorous, unitarization procedure to the S -matrix, derived in Subsec. 2.2.1. The analyticity and causality implications of complex masses in asymptotic states were already studied

¹Henceforth, we omit the bar in $D\bar{D}^*$, for notational simplicity.

a long time ago [115].

For consistency, we apply the same procedure to the ω meson, despite the fact that its width is a factor 17.5 smaller than that of the ρ . Nevertheless, the ω width of about 8.5 MeV is very close to the energy difference between the $\omega J/\psi$ and $D^0 D^{*0}$ thresholds, and therefore not negligible. Finally, we shall neglect the unknown small (< 2.1 MeV [80]) D^{*0} width [107], because of the relatively large error bars on the $D^0 D^{*0}$ data, though this width may have some influence on the precise $X(3872)$ pole position. Nevertheless, reasonable estimates of the D^{*0} width yield values clearly smaller than 100 keV [116], so that its effect should be largely negligible as compared to that of the ρ and ω widths.

Let us now proceed with our RSE calculation of a bare 2^3P_1 (with $n=1$, $J=1$, $L=1$, $S=1$) $c\bar{c}$ state, coupled to a number of MM channels. The resulting closed-form T -matrix is given, one more, in Sec. 2.2. In Table 5.1 we list the considered PV

Channel	$\left(g_{(l_c=1, n=0)}^i\right)^2$	L	Threshold (MeV)
$\rho^0 J/\psi$	variable	0	$3872.406 - i 74.7$
$\omega J/\psi$	variable	0	$3879.566 - i 4.25$
$D^0 D^{*0}$	1/54	0	3871.81
$D^0 D^{*0}$	5/216	2	3871.81
$D^\pm D^{*\mp}$	1/54	0	3879.84
$D^\pm D^{*\mp}$	5/216	2	3879.84
$D^* D^*$	5/36	2	4017.24
$D_s^\pm D_s^{*\mp}$	1/54	0	4080.77
$D_s^\pm D_s^{*\mp}$	5/216	2	4080.77

Table 5.1: Included meson-meson channels, with thresholds and ground-state couplings. For simplicity, we omit the bars over the anti-charm mesons; also note that $D^* D^*$ stands for the corresponding mass-averaged charged and uncharged channels.

and VV channels, including $\rho^0 J/\psi$ and $\omega J/\psi$. Besides the latter two OZIS channels and the also observed OZIA $D^0 D^{*0}$ channel, we furthermore account for the OZIA PV and VV channels $D^\pm D^{*\mp}$, $D^* D^*$, and $D_s D_s^*$, whose influence on the $X(3872)$ pole position is not negligible, in spite of being closed channels. The $D_s^* D_s^*$ channel, with threshold about 350 MeV above the $X(3872)$ mass, we do not include.

The relative couplings of the OZIA channels have been computed as discussed in Sec. 2.2.

Couplings calculated in the latter scheme for ground-state mesons generally coincide with the usual recouplings of spin, isospin, and orbital angular momentum. Moreover, for excited states the formalism yields clear predictions as well, contrary to other approaches. In Table 5.1, the squares of the ground-state ($n=0$) couplings

are given, which have to be multiplied by $(n+1)/4^n$ for the S -wave PV channels, and by $(2n/5+1)/4^n$ for the others, so as to obtain the couplings in the RSE sum of Eq. (2.28). Also note that the two (closed) D^*D^* channels have been lumped together, with their average threshold value and sum of squared couplings. As for the couplings of the $\rho^0 J/\psi$ and $\omega J/\psi$ channels, the formalism of Ref. [48], based on OZIA decay via 3P_0 quark-pair creation, cannot make any prediction. However, we know from experiment that the couplings of OZIS channels are considerably smaller than those of OZIA channels. Moreover, isospin-breaking channels are even further suppressed. Thus, in the following we shall employ the values $g_{\rho^0 J/\psi} = 0.07 \times g_{D^0 D^{*0}}$ and $g_{\omega J/\psi} = 0.21 \times g_{D^0 D^{*0}}$, which correspond to effective relative strengths of 0.49% and 4.41%, respectively, which seem reasonable to us. These values may also be compared to the corresponding relative probabilities of about 0.65% ($\approx 0.006/0.92$) and 4.5% ($\approx 0.041/0.92$), respectively, employed in Ref. [110]. Furthermore, we shall also test coupling values twice as large, namely $g_{\rho^0 J/\psi} = 0.14 \times g_{D^0 D^{*0}}$ and $g_{\omega J/\psi} = 0.42 \times g_{D^0 D^{*0}}$. Note that our coupling for the isospin-breaking channel $\rho^0 J/\psi$ is also in rough agreement with estimates from the rate of the observed [80] isospin-violating $\omega \rightarrow \pi^+ \pi^-$ decay, which amounts to about 1.5% of the total width. Another difference between OZIA and OZIS channels is the average distance r_i (see Eqs. (2.29,2.30)) at which a light $q\bar{q}$ pair is created before decay, which in the OZIA case we believe to take place in the core region and in the OZIS case more in the periphery. Thus, we employ a larger value for $r_1 \equiv r_{\rho^0 J/\psi} = r_{\omega J/\psi}$ than for r_0 , the single radius used for all OZIA channels. Concretely, we take $r_0 = 2 \text{ GeV}^{-1} \simeq 0.4 \text{ fm}$ and $r_1 = 3 \text{ GeV}^{-1} \simeq 0.6 \text{ fm}$, while we also test the case $r_1 = r_0$.

For the bare $c\bar{c}$ energy levels $E_n^{(l_c)}$ in the RSE sum of Eq. (2.28), we take the equidistant harmonic oscillator (2.31) with the parameters in Eq. (2.32), as previously. The only parameter we adjust freely is the overall coupling constant λ in Eqs. (2.29,2.30), which is tuned to move the bare 2^3P_1 state from 3979 MeV down to the $D^0 D^{*0}$ threshold, requiring a λ value of the order of 3, i.e., not far from the values used in e.g. Chapter 3 and Ref. [44]. At the same time, the bare 1^3P_1 state shifts from 3599 MeV down to about 3.55 GeV, though depending quite sensitively on the precise form of the used subthreshold suppression of closed channels Chapter 3. Anyhow, for the purpose of the present study, an accurate reproduction of the $\chi_{c1}(1P)$ mass of 3511 MeV is not very relevant.

5.2 $X(3872)$ poles and amplitudes vs. data

In Table 5.2, we give some pole positions in the vicinity of the $D^0 D^{*0}$ and $\rho^0 J/\psi$

Label	λ	$\tilde{g}_{\rho^0 J/\psi}$	$\tilde{g}_{\omega J/\psi}$	Pole (MeV)
1	3.028	0.07	0.21	$3872.30 - i 0.71$
2	3.066	0.07	0.21	$3871.83 - i 0.40$
3	3.083	0.07	0.21	$3871.56 - i 0.11$
a	2.981	0.14	0.42	$3872.30 - i 0.75$
b	3.017	0.14	0.42	$3871.82 - i 0.48$
c	3.033	0.14	0.42	$3871.57 - i 0.28$

Table 5.2: Pole positions of the dots and stars in Fig. 5.1. In all cases, $r_1 = 3.0 \text{ GeV}^{-1}$. Note that the OZIS couplings $\tilde{g}_{\rho^0 J/\psi}$ and $\tilde{g}_{\omega J/\psi}$ are given relative to the coupling of the OZIA $D^0 D^{*0}$ channel.

thresholds, with the chosen values of λ and r_1 . In Fig. 5.1, third-sheet pole trajectories in the complex energy plane (relative to the $D^0 D^{*0}$ threshold) are plotted, as

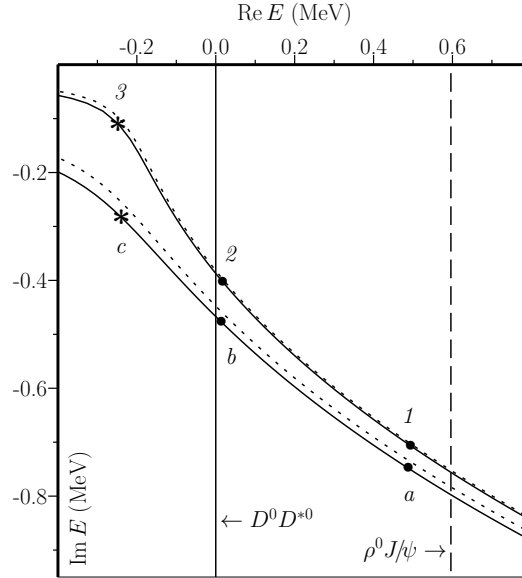


Figure 5.1: Pole trajectories for $r_1 = 3.0 \text{ GeV}^{-1}$ (solid curves) and $r_1 = 2.0 \text{ GeV}^{-1}$ (dotted curves); $g_{\rho^0 J/\psi} / g_{D^0 D^{*0}} = 0.07$ and $g_{\omega J/\psi} / g_{D^0 D^{*0}} = 0.21$ (upper two curves), $g_{\rho^0 J/\psi} / g_{D^0 D^{*0}} = 0.14$ and $g_{\omega J/\psi} / g_{D^0 D^{*0}} = 0.42$ (lower two curves). Note that the CM energy E is relative to the $D^0 D^{*0}$ threshold in all figures. Also see Table 5.2.

a function of λ , with the pole positions of Table 5.2 marked by bullets and stars. The solid curves represent the case $r_1 = 3.0 \text{ GeV}^{-1}$, while the dotted ones stand for $r_1 = 2.0 \text{ GeV}^{-1}$, showing little sensitivity to the precise decay radius. Figure 5.1

shows that the $X(3872)$ resonance pole may come out below the $D^0 D^{*0}$ threshold with a nonvanishing width, which is moreover of the right order of magnitude, viz. < 1 MeV. The recent CDF [97] mass determination of the $X(3872)$ might suggest that the pole positions '3' or 'c' (see Table 5.2 and Fig. 5.1) are favored. However, one should realize that the differences amount to mere fractions of an MeV, while experimental uncertainties are at least of the same order.

Now we compare the corresponding $D^0 D^{*0}$ amplitudes to Belle [117] data, for the six cases labeled '1, 2, 3', and 'a, b, c' in Table 5.2 and Fig. 5.1. The results are depicted in Figs. 5.2 and 5.2, respectively. Note that we allow for an arbitrary nor-

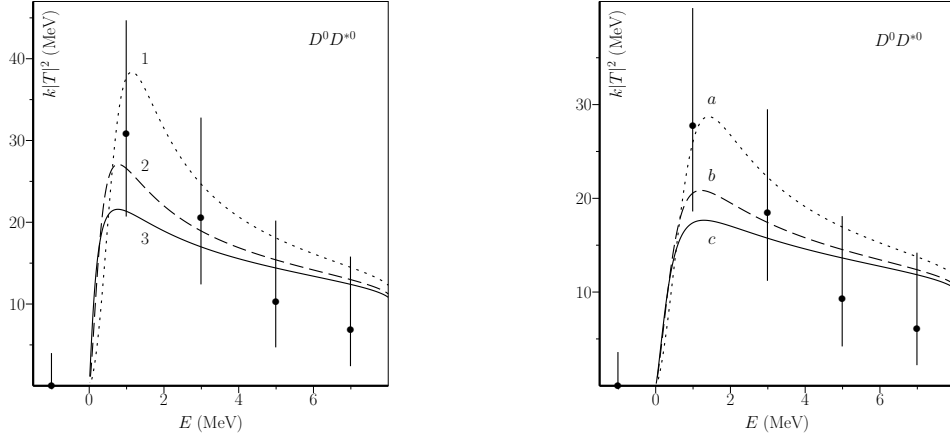


Figure 5.2: $D^0 D^{*0}$ elastic amplitude for poles 1, 2, 3 in Table 5.2 and Fig. 5.1; arbitrarily normalized data are from Ref. [117]. Elastic T -matrix elements follow from Eqs. (2.29–2.28); k is on-shell relative momentum. (b) for poles a, b, c.

malization of the data, which is inevitable as we are dealing with production data, which cannot be directly compared with our scattering amplitudes, also because of the finite experimental mass bins. From these figures we see that the best agreement with data is obtained in case '2', though 5 out of the 6 curves pass through all error bars. Nevertheless, in view of the large errors, one should be very cautious in drawing definite conclusions on the precise pole position as well as the preferred OZIS couplings $g_{\rho^0 J/\psi}$ and $g_{\omega J/\psi}$.

Next we show, in Fig. 5.3, the elastic amplitudes in the $\rho^0 J/\psi$ and $\omega J/\psi$ channels, corresponding to the pole positions 1, 2, 3, i.e., for the smaller values of the OZIS couplings. We see that both amplitudes are very sensitive to the precise pole position, which is logical, as the OZIS channels couple much more weakly to $c\bar{c}$ than $D^0 D^{*0}$, so that the latter channel will strongly deplete the former ones, as soon as it acquires some phase space. This is in line with our analysis in e.g. Ref. [118]. Also

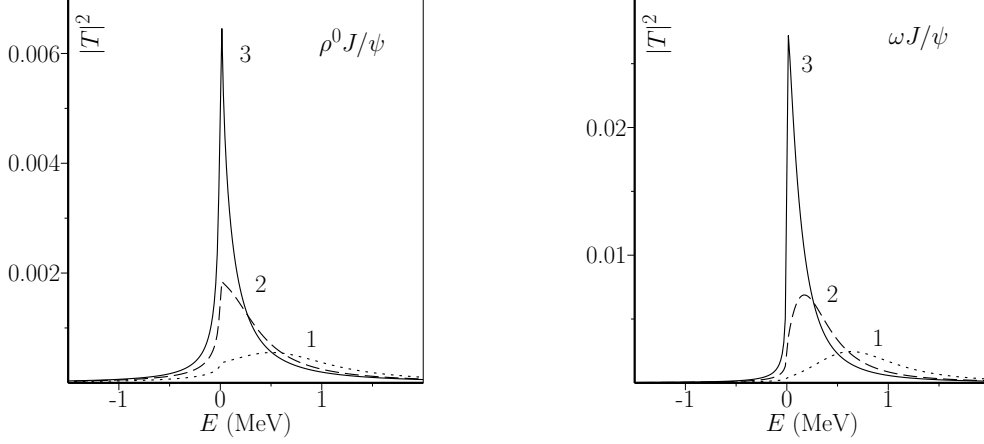


Figure 5.3: $\rho^0 J/\psi$ (left) and $\omega J/\psi$ (right) elastic amplitudes for poles 1, 2, 3. Also see Fig. 5.1 and Table 5.2.

note the strongly cusp-like structure of the amplitude in the cases 2 and 3 for $\rho^0 J/\psi$, and 3 for $\omega J/\psi$, which is a manifestation of the depletion due to the opening of the $D^0 D^{*0}$ channel. Such a cusp makes the experimental determination of the $X(3872)$ width very difficult.

In Fig. 5.4 we take a closer look at the $\omega J/\psi$ and $\rho^0 J/\psi$ amplitudes, in particular how they compare to one another. Now, the effective strength of the $\omega J/\psi$ elastic T -matrix element is 9 times that of $\rho^0 J/\psi$, as its coupling has been chosen 3 times as large (see Table 5.2 and Eqs. (2.29–2.28)). For the corresponding square amplitudes plotted in Fig. 5.4, this amounts to a factor as large as 81. However, the central $\omega J/\psi$ threshold lies more than 7 MeV above that of $\rho^0 J/\psi$, while the full ω width is only 8.49 MeV. On the other hand, the central $\rho^0 J/\psi$ threshold lies much closer to $D^0 D^{*0}$, while the large physical ρ width strongly boosts the associated amplitude, as demonstrated below. Qualitative arguments in agreement with our calculation were already presented in Ref. [119]. These effects make the maximum $\omega J/\psi$ square amplitude to be only a factor 3.5–4 larger than that of $\rho^0 J/\psi$, both in case 2 and 3, as can be read off from Fig. 5.4. Moreover, at the precise energy of the respective pole position, the two amplitudes are almost equal in size. Therefore, the observed branching ratio $\mathcal{B}(X(3872) \rightarrow \omega J/\psi)/\mathcal{B}(X(3872) \rightarrow \pi^+ \pi^- J/\psi) \sim 1$ [98, 99] is compatible with the present model calculation. Finally, in order to study the effect of using a complex mass for the ρ^0 in the $\rho^0 J/\psi$ channel, we vary the ρ width from 0% to 100% of its PDG [80] value and plot the corresponding amplitudes in Fig. 5.5. We see that the maximum $|T|^2$ increases by almost 3 orders of magnitude when going from the 0% case (dotted curve in left-hand plot) to the 100% case (solid curve in

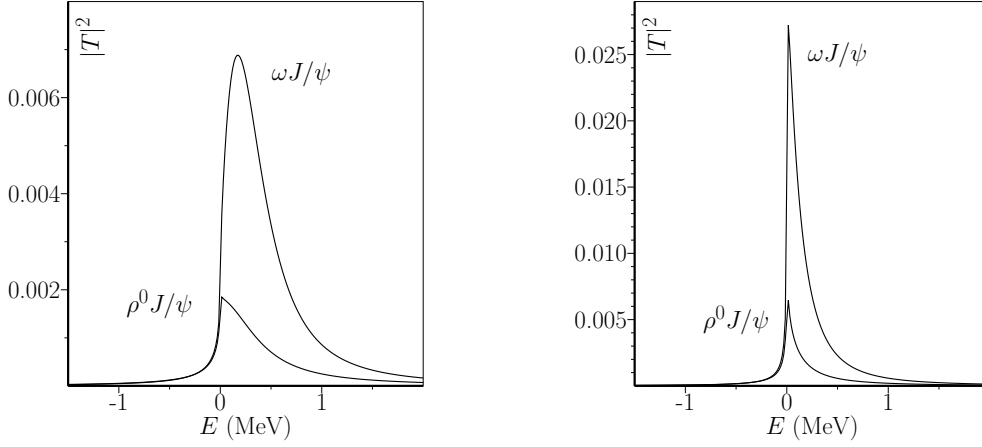


Figure 5.4: $\rho^0 J/\psi$ and $\omega J/\psi$ elastic amplitudes, for poles 2 (left) and 3 (right). Also see Fig. 5.1 and Table 5.2.

right-hand plot). Furthermore, the 0% curve only starts out at the central $\rho^0 J/\psi$ threshold, of course. Thus, it becomes clear that no realistic description of the $\rho^0 J/\psi$ channel is possible without smearing out somehow its threshold, so that its influence kicks in before the $D^0 D^{*0}$ channel opens and depletes the signal. Naturally, similar conclusions apply in principle to the $\omega J/\psi$ channel, though there the effects are less pronounced because of the small ω width and the somewhat higher threshold. These results show that our unitarization procedure for complex masses in the asymptotic states performs as expected in accounting for thresholds involving resonances. To conclude our discussion, we should mention that our results are qualitatively in agreement with those of Danilkin & Simonov [108], in the sense that a single resonance pole originating from the 2^3P_1 $c\bar{c}$ state is capable of describing the $X(3872)$ data. However, we disagree with their conclusions on the 2^3P_0 state. In an earlier, single-channel description [120], we found a resonance at 3946 MeV with a width of 58 MeV, and we do not believe a detailed multichannel calculation will change these values dramatically. Thus, the listed $X(3945)$ [80] resonance, with mass 3916 MeV, width 40 MeV, and positive C -parity, appears to be a good candidate. As for the 2^1P_1 state, the $X(3940)$ [80] resonance, with mass 3942 MeV, width 37 MeV, and principal decay mode DD^* , seems the obvious choice. With the old $Z(3930)$ meanwhile identified as the 2^3P_2 ($\chi_{c2}(2P)$ [80]) state, we might so understand all 4 charmonium states in the range 3.87–3.95 MeV.

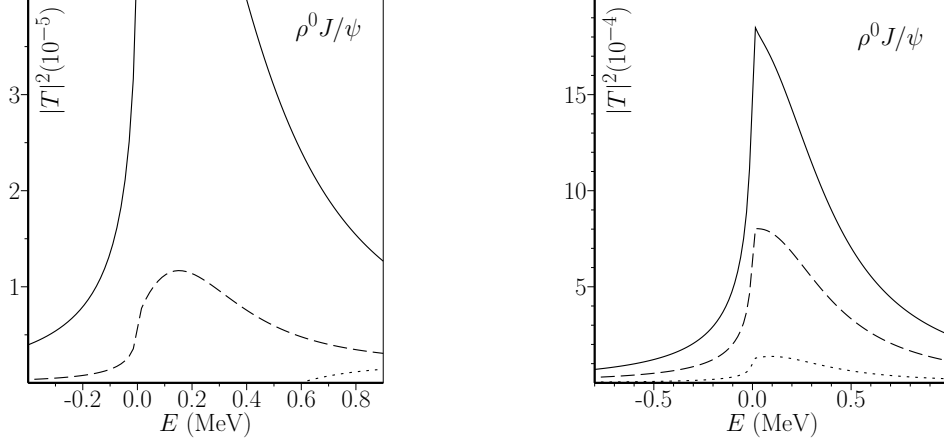


Figure 5.5: $\rho^0 J/\psi$ elastic amplitude for reduced ρ^0 width. Left: 0% (dots), 1% (dashes), 5% (full); right: 10% (dots), 50% (dashes), 100% (full). Studied case: pole 2 in Table 5.2. Also see Fig. 5.1.

5.3 Summary and conclusions

Summarizing, we have investigated the 1^{++} charmonium scenario for the $X(3872)$ resonance, by analyzing in detail the influence of the $D^0 D^{*0}$, $\rho^0 J/\psi$, and $\omega J/\psi$ channels on pole positions and amplitudes. In order to describe the latter OZIS channels in a realistic way, we have used complex masses for the ρ^0 and ω , and then restored unitarity of the S -matrix by a new and rigorous algebraic procedure, albeit physically heuristic. It is true that the redefined S -matrix may have some unusual analyticity properties [115], but in our amplitudes no sign was found of any nearby spurious singularities. Moreover, the behaviour of the $\rho^0 J/\psi$ amplitude as a function of the ρ^0 width gives us confidence in our approach. Concretely, we have shown that our scenario is compatible with the $D^0 D^{*0}$ and $\pi^+ \pi^- J/\psi$ data, with a single resonance pole on top of or slightly below the $D^0 D^{*0}$ threshold. Moreover, our treatment of the $\rho^0 J/\psi$ and $\omega J/\psi$ channels has proven compatible with the observed branching ratio of these decays.

Thus, the data do not seem to require a molecular or tetraquark interpretation of the $X(3872)$, also in view of so far unobserved [121] charged partner states.

Nevertheless, only further improved measurements and theoretical calculations will in the end allow to draw a definitive conclusion on the scenario preferred by nature. In conclusion, we must stress that the $X(3872)$, whatever its assignment, is an extraordinary structure, because of its coincidence — to an accuracy of less than 1 MeV — with the central thresholds of the principal decay modes. This circumstance is at the same time a blessing and a curse. To start with the latter, no model can

ambition to quantitatively describe the $X(3872)$ with present-day state-of-the-art in strong interactions, while experiment will have an extremely hard time to reduce the bin sizes to less than 1 MeV and simultaneously keep statistics sufficiently high. On the other hand, with a strengthened effort of both theory and experiment, a wealth of knowledge on charmonium spectroscopy and strong decay — OZI-allowed as well as OZI-suppressed — may be gathered by further studying this peculiar resonance.

Chapter 6

$X(3872)$ is not a true molecule

S. Coito, G. Rupp, and E. van Beveren, *EPJC* **73**, 2531 (2013).

On the theory side, the discussion about the nature of $X(3872)$ continues most vivid. Even before the recent result of LHCb [100], most model builders described the state as an axial vector. For instance, model calculations of semi-inclusive $B \rightarrow \eta_{c2} + X$ processes [122] as well as electromagnetic η_{c2} decays [123] have been shown to disfavor the 2^{-+} scenario. The same conclusion was reached in a tetraquark description of $X(3872)$ [124], while pion exchange in a molecular picture would be repulsive in this case [125] and so inhibitive of a bound state. Finally, unquenching a 1^1D_2 $c\bar{c}$ state by including meson-meson loops could only further lower the bare mass, which lies in the range 3.79–3.84 GeV for all quenched quark models we know of, thus making a 2^{-+} charmonium resonance at 3.872 GeV very unlikely. For further information and more references concerning $X(3872)$, see e.g. a recent review [126], as well as our previous coupled-channel analysis in Chapter 5.

The first suggestion of possible meson-meson molecules bound by pion exchange, in particular a DD^* state with quantum numbers 1^{++} or 0^{-+} , was due to Törnqvist [125]. With the discovery of $X(3872)$ just below the D^0D^{*0} threshold, this idea was revived, of course. In the present chapter, we intend to study the issue, not from Törnqvist’s pion-exchange point of view, but rather as regards its possible implications for models based on quark degrees of freedom. In this context, it is worthwhile to quote from Ref. [116], in which a molecular interpretation is advocated (also see Ref. [127]):

“Independent of the original mechanism for the resonance, the strong coupling transforms the resonance into a bound state just below the two-particle threshold if $a > 0$ or into a virtual state just above the two-particle threshold if $a < 0$. If $a > 0$, the bound state has a molecular structure,

with the particles having a large mean separation of order a ."

(Note that, here, a is the S -wave scattering length.) Also:

"In this case $[1^{++}]$, the measured mass M_X implies unambiguously that X must be either a charm meson molecule or a virtual state of charm mesons."

In face of these peremptory claims about the molecular picture, it is of utmost importance to study in detail the $X(3872)$ wave function for a model in which the *mechanism* generating the meson is quark confinement combined with strong decay. Thus, we employ the simplified, coordinate-space version of RSE, defined in Sec. 2.3, to describe $X(3872)$ as a unitarized and mass-shifted 2^3P_1 charmonium state. The model's exact solvability then allows to obtain analytic expressions for the wave-function components, and follow bound-state as well as resonance poles on different Riemann sheets.

6.1 The coupled $c\bar{c}$ - D^0D^{*0} system

Now we apply the formalism to the coupled $c\bar{c}$ - D^0D^{*0} system. The $c\bar{c}$ channel is assumed to be in a 3P_1 state, i.e., with $l_c = 1$, implying the D^0D^{*0} channel to have $l_f = 0$ or 2. Nevertheless, we shall restrict ourselves here to the S -wave channel only, which will be strongly dominant, especially near threshold. The fixed parameters are given in Table 6.1, where the meson masses are from the PDG [39],

Param.	ω	m_c	m_{D^0}	$m_{D^{*0}}$	$m_{D^0} + m_{D^{*0}}$
(MeV)	190	1562	1864.86	2006.98	3871.84

Table 6.1: Fixed parameters.

while ω and the constituent charm quark mass m_c are defined in (2.32). Thus, from Eq. (2.31) we get the lowest two harmonic oscillator states at $E_0 = 3599$ MeV and $E_1 = 3979$ MeV, respectively. The former should give rise — after unquenching — to the 1^3P_1 charmonium state $\chi_{c1}(1P)$ [39], with mass 3511 MeV, while the latter is the bare 2^3P_1 state, which cannot so easily be linked to resonances in the PDG tables, though both $X(3940)$ and $X(3872)$ are possible candidates, in view of their mass and dominant DD^* decay mode [39]. However, $X(3940)$ may just as well be the, so far unconfirmed, 2^1P_1 (1^{+-}) state $h_c(2P)$, cf. Sec. 5.2.

The two remaining parameters, viz. the string-breaking distance a and the global

coupling g , have to be adjusted to the experimental data. Nevertheless, these parameters are not completely free, as they both have a clear physical interpretation, albeit of an empirical nature. Thus, a is the average interquark separation at which 3P_1 quark-pair creation/annihilation is supposed to take place, while g is the overall coupling strength for such processes. Note that we do not assume a particular microscopic model for string breaking inspired by QCD, like e.g. in a very recent paper [128]. Still, the values of a found in the present work are in rough agreement with our prior model findings, and even compatible [129] with a lattice study of string breaking in QCD [130]. Concretely, we have been obtaining values of a in the range $1\text{--}4\text{ GeV}^{-1}$ ($0.2\text{--}0.8\text{ fm}$), logically dependent on quark flavor, since the string-breaking distance will scale with the meson's size, being smallest for bottomonium. As for the coupling parameter g , its empirical value will depend on a , but also on the set of included decay channels. In realistic calculations, values of the order of 3 have been obtained (see e.g. Table 5.2, where $g \equiv \lambda$).

6.2 Poles

The crucial test the present model must pass is its capability of generating a pole near the $D^0 D^{*0}$ threshold. Indeed, a dynamical pole is found slightly below threshold for different combinations of the free parameters a and g , several of which are listed in Table 6.2. Examples are here given of bound states, virtual bound states, and below-threshold resonances, the latter ones only occurring for S -wave thresholds as in our case. Note that poles of both virtual bound states and resonances lie on the second Riemann sheet, i.e., the relative momentum has a negative imaginary part. From this table we also observe that larger and larger couplings are needed to generate a pole close to threshold when a approaches the value 3.5 GeV^{-1} . We shall see below that this is due to the nodal structure of the bound-state wave function.

Although a dynamical pole shows up near the $D^0 D^{*0}$ threshold, there still should be a confinement pole connected to the first radial 3P_1 excitation at 3979 MeV . Well, we do find such a pole, for each entry in Table 6.2. In Table 6.3 a few cases are collected, with the parameters tuned to generate a dynamical pole at precisely the $X(3872)$ PDG [39] mass of 3871.68 MeV . Note, however, that the associated confinement pole is not necessarily of physical relevance, since at the corresponding energy several other strong decay channels are open, which no doubt will have a very considerable influence and possibly even change the nature of both poles. As a matter of fact, in Chapter 5, with all relevant two-meson channels included, the $X(3872)$ resonance

a (GeV $^{-1}$)	g	pole (MeV)	type
2.0	1.149	3871.84	VBS
2.5	1.371	3871.84	VBS
3.0	2.142	3871.84	VBS
3.1	2.503	3871.84	VBS
3.2	2.531	$3871.84 - i12.01$	resonance
3.3	3.723	$3871.84 - i 4.45$	resonance
3.4	7.975	$3871.84 - i 0.39$	resonance
3.5	∞		-
2.0	1.152	3871.84	BS
2.5	1.373	3871.84	BS
3.0	2.145	3871.84	BS
3.1	2.507	3871.84	BS
3.2	3.083	3871.84	BS
3.3	4.194	3871.84	BS
3.4	8.254	3871.84	BS
3.5	∞		-

Table 6.2: Bound states (BS), virtual bound states (VBS), and resonances closest to threshold, for various g and a combinations.

a (GeV $^{-1}$)	g	dynamical pole	confinement pole
2.0	1.172	3871.68	$4030.50 - i136.51$
2.5	1.403	3871.68	$4063.27 - i124.07$
3.0	2.204	3871.68	$4101.48 - i 88.03$
3.4	8.623	3871.68	$4185.85 - i 20.63$

Table 6.3: Pole doubling: pairs of poles (in MeV) for some sets of a and g values, chosen such that the dynamical pole settles at the $X(3872)$ PDG [39] mass.

was found as a confinement pole, whereas dynamical poles were only encountered very deep in the complex energy plane, without any observable effect at real energies. So here we show these results only to illustrate that pole doubling may occur when strongly coupling S -wave thresholds are involved, as we have observed in the past in the case of e.g. the light scalar mesons [131] and $D_{s0}^*(2317)$ [43]. The issue of confinement vs. dynamical poles will be further studied in Sec. 6.5.

In order to better understand the dynamics of the different poles, we plot in Fig. 6.1 pole trajectories in the complex energy plane as a function of the coupling constant g , and for three different values of a . For vanishing g , the dynamical pole acquires a negative infinite imaginary part and so disappears in the continuum, whereas the confinement pole moves to the real energy level of the bare 2^3P_1 state, i.e., 3979 MeV.

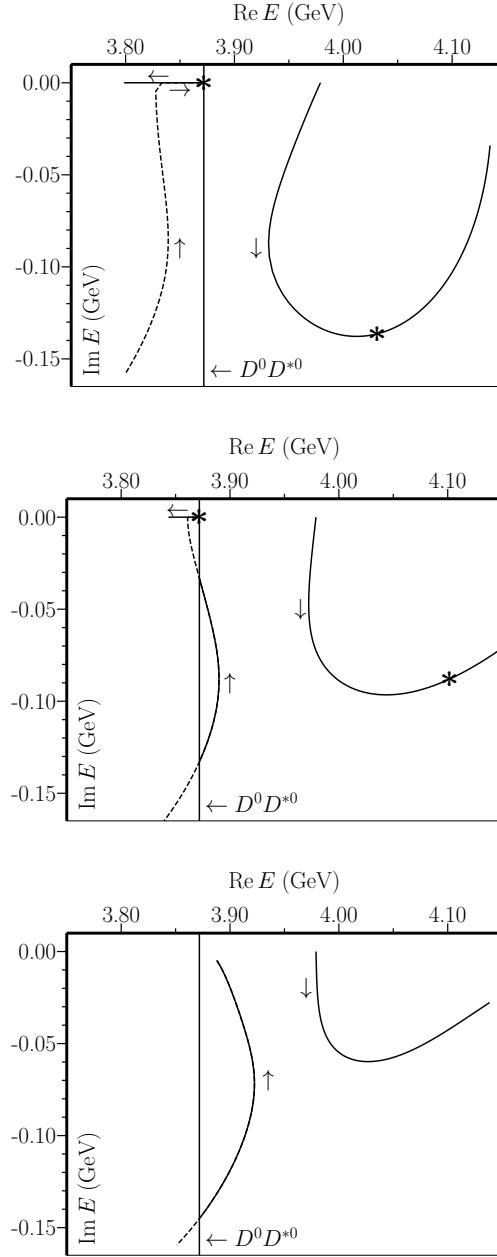


Figure 6.1: Pole trajectories of dynamical (left) and confinement (right) poles as a function of g , for $a=2.0 \text{ GeV}^{-1}$ (top), 3.0 GeV^{-1} (middle), and 3.5 GeV^{-1} (bottom), respectively. In the last case, there is no bound state near threshold. Note: (i) poles in Table. 6.3 are here marked by $*$; (ii) arrows along curves indicate increasing g .

As g increases, and for both $a = 2.0 \text{ GeV}^{-1}$ and $a = 3.0 \text{ GeV}^{-1}$, the dynamical pole moves to the real axis below threshold, becoming first a virtual bound state and then a genuine bound state. Note that, in the latter case, the real part twice attains

the $X(3872)$ mass even before the pole reaches the real axis, but the corresponding imaginary parts are much too large as compared with experiment [39], so only the bound state can be considered physical. Finally, for $a = 3.5 \text{ GeV}^{-1}$ the pole does never reach the real axis, which would require an infinite coupling. For the other parameter sets listed in Table 6.2, we find intermediate situations. Another feature we can observe for all trajectories is an initial attraction and subsequent repulsion between the dynamical and the confinement poles.

6.3 Wave function

Now we are in a position to study the $X(3872)$ bound-state wave function in several situations. We choose two values for the string-breaking parameter, viz. $a = 2.0 \text{ GeV}^{-1}$ and $a = 3.0 \text{ GeV}^{-1}$. In Table 6.4 five different binding energies (BEs) are chosen with respect to the $D^0 D^{*0}$ channel, including the PDG [39] value labeled by X . We have computed and normalized (see Subsec. 2.3.1) the two-component radial wave function $R(r)$ for each of the five cases. In Fig. 6.2 we depict the cases labeled by A , X and D , the other two representing intermediate situations. General features we immediately observe are the typical S -wave behavior of the $D^0 D^{*0}$ wave-function component R_f , while the $c\bar{c}$ wave function R_c is in a P state, the latter also having a node, as it is dominantly a first radial excitation. Furthermore, $|R_f|$ is larger than $|R_c|$ in most situations, for all r , except for unphysically large BEs (cf. plot D). Nevertheless, the two components are of comparable size for intermediate r values. Then, as the BE becomes smaller, the tail of R_f grows longer, as expected, whereas R_c always becomes negligible for distances larger than roughly $11\text{--}12 \text{ GeV}^{-1}$. Now, the increased R_f tail affects the normalization of *both* R_c and R_f . Thus, the ratio $|R_f(r)|/|R_c(r)|$ is quite robust for most r values, as it does not significantly change with the BE.

$a \text{ (GeV}^{-1}\text{)}$		2.0		3.0	
label	BE (MeV)	g	pole	g	pole
A	0.00	1.152	3871.84	2.145	3871.84
B	0.10	1.167	3871.74	2.191	3871.74
X	0.16	1.172	3871.68	2.204	3871.68
C	1.00	1.207	3870.84	2.311	3870.84
D	10.00	1.373	3861.84	2.899	3861.84

Table 6.4: Five chosen binding energies (BE) in the $D^0 D^{*0}$ channel, for two different a values and the corresponding couplings g .

a	channel	A	B	X	C	D
2.0	$c\bar{c}$	0.63	6.00	7.48	16.98	39.68
2.0	$D^0 D^{*0}$	99.37	94.00	92.52	83.02	60.32
3.0	$c\bar{c}$	0.97	9.01	11.18	24.65	55.54
3.0	$D^0 D^{*0}$	99.03	90.99	88.82	75.35	44.46

Table 6.5: Probabilities (in %) of the two wave-function components, for the cases specified in Table 6.4 (a in GeV^{-1}).

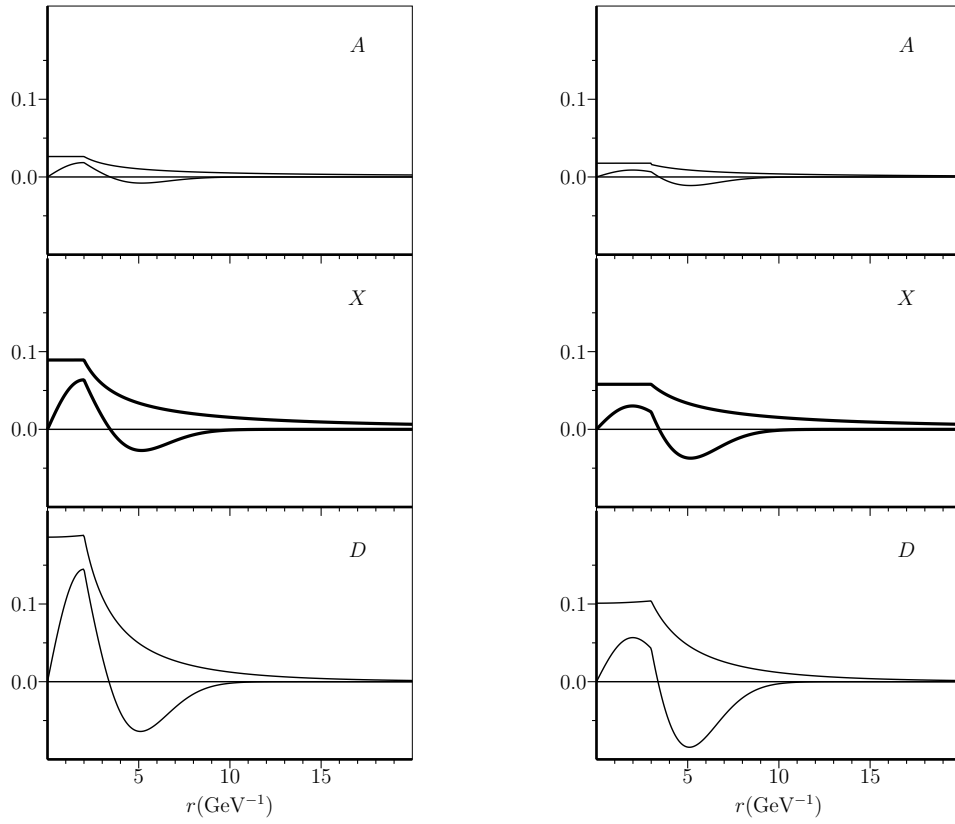


Figure 6.2: Normalized two-component radial wave function $R(r)$ for three BEs, corresponding to labels A, X, D in Table 6.4, and two a values. Upper curves: $R_f(r)$; lower curves: $R_c(r)$. Left: $a = 2 \text{ GeV}^{-1}$; right: $a = 3 \text{ GeV}^{-1}$.

6.4 Probabilities and r.m.s. radii

Having derived the $X(3872)$ wave function for several scenarios, we can now straightforwardly compute the relative probabilities of the $c\bar{c}$ and $D^0 D^{*0}$ components (see Subsec. 2.3.1), with the results given in Table 6.5, for the five BEs and two a values

a (GeV $^{-1}$)	a (fm)	A	B	X	C	D
2.0	0.39	100.22	9.92	7.82	3.10	1.15
3.0	0.59	100.14	9.85	7.76	3.05	1.23

Table 6.6: R.m.s. radii of the wave function, expressed in fm, for the cases specified in Table 6.4.

from Table 6.4. Note that the probability in the $D^0 D^{*0}$ channel is only computed for normalization purposes, since in a more realistic calculation at least the $D^\pm D^{*\mp}$ component would acquire a nonnegligible probability as well, as the corresponding threshold lies only 8 MeV higher. Nevertheless, our simplification is unlikely to have an appreciable effect on the $c\bar{c}$ probability and will only increase that of the $D^0 D^{*0}$ component accordingly. Also note that the $c\bar{c}$ probability includes all 3P_1 states, with the 2^3P_1 being dominant, because the corresponding bare eigenstate lies only 100 MeV higher. However, also the 1^3P_1 state is nonnegligible in the physical $X(3872)$ wave function. In the coupled-channel approach of Ref. [132], a 1^3P_1 admixture of about 15% was found. Notice that — inevitably — unquenching not only mixes meson-meson components into the total bound-state wave function, but also quark-antiquark components of confinement states other than the one under consideration (also see Ref. [51]). Here, for a BE of 0.16 MeV, corresponding to the physical [39] $X(3872)$, case **X** in Table 6.5, has a 7.48% $c\bar{c}$ probability for $a = 2.0$ GeV $^{-1}$ and 11.18% for $a = 3.0$ GeV $^{-1}$. For smaller BEs, the $c\bar{c}$ probability decreases as expected, because of the growing weight of the $D^0 D^{*0}$ tail. On the other hand, for a BE of 10 MeV and $a = 3.0$ GeV $^{-1}$, the charmonium probability becomes even larger than that of the meson-meson component. Now, the experimental errors in the average mass of the $X(3872)$ and the $D^0 D^{*0}$ threshold allow for a maximum BE of 0.57 MeV, i.e., somewhere in between cases **X** and C . This would then correspond to a $c\bar{c}$ probability roughly midway in the range 7.48%–16.98% ($a = 2.0$ GeV $^{-1}$) or 11.18%–24.65% ($a = 3.0$ GeV $^{-1}$). In the limiting case of zero binding, the $c\bar{c}$ probability would eventually vanish. Also notice that, in all five cases of Table 6.5, the $c\bar{c}$ probability rises by about 50% when a is increased from 2.0 to 3.0 GeV $^{-1}$. Nevertheless, if we take $a = 2.0$ GeV $^{-1}$ as in Chapter 5, we get a $c\bar{c}$ probability of 7.48%, very close the 7% found in Refs. [133, 134].

Next we use the normalized wave functions and Eq. (2.53) to compute the $X(3872)$ r.m.s. radius for the five cases discussed before (see Table 6.4), with the results presented in Table 6.6. It is interesting to observe that the r.m.s. radius, which in principle is an observable, is much less sensitive to the choice of a than de wave-function probabilities. Furthermore, the large to very large r.m.s. radii in the various

situations are hardly surprising, in view of the small binding energies and the resulting very long tails of the $D^0 D^{*0}$ wave-function components (see Fig. 6.2 above). Using Eq. (2.54), we now also evaluate the S -wave scattering length

$$a_S = - \lim_{E \rightarrow 0} [k(E) \cot \delta_0(E)]^{-1}.$$

In case **X** and for $a = 2.0 \text{ GeV}^{-1}$ we thus find $a_S = 11.55 \text{ fm}$, which is large yet of the expected order of magnitude for a BE of 0.16 MeV. For even smaller BEs, the scattering length will further increase, roughly like $\propto 1/\sqrt{\text{BE}}$. Let us here quote from Ref. [127]:

*“Low-energy universality implies that as the scattering length a increases, the probabilities for states other than $D^0 \bar{D}^{*0}$ or $\bar{D}^0 D^{*0}$ decrease as $1/a$...”*

Indeed, we verify from our Table 6.5 that — very roughly — the $c\bar{c}$ probability decreases as $\propto \sqrt{\text{BE}}$, and so like $\propto 1/a_S$.

6.5 Stability of results and nature of poles

In this section we are going to study the stability of our results, as well as the nature of the found solutions. So let us vary the two usually fixed parameters, viz. ω and m_c , in such a way that the bare 1^3P_1 mass remains unaltered at 3599 MeV, whereas that of the 2^3P_1 changes as shown in Table. 6.7. Thus, in case *I* E_1 is lowered by

	<i>I</i>	standard	<i>II</i>
E_1 (MeV)	3954	3979	4079
m_c (MeV)	1577.63	1562	1499.5
ω (MeV)	177.5	190	240
g	1.034	1.172	1.572
$c\bar{c}$ (%)	9.49	7.48	6.51
$r_{\text{r.m.s.}}$ (fm)	7.72	7.82	8.83

Table 6.7: Probability of $c\bar{c}$ component and $X(3872)$ r.m.s. radius for varying ω, m_c , with bare E_0 fixed at 3599 MeV, $X(3872)$ pole at 3871.68 MeV, and $a = 2.0 \text{ GeV}^{-1}$.

25 MeV, while in case *II* it rises by 100 MeV. The trajectories for these two new situations are plotted in Fig. 6.3. For *I* we observe that, just as in the standard case depicted in Fig. 6.1, two poles are found relatively close to the real axis, of a dynamical and a confinement origin, respectively. However, now it is the 2^3P_1 confinement

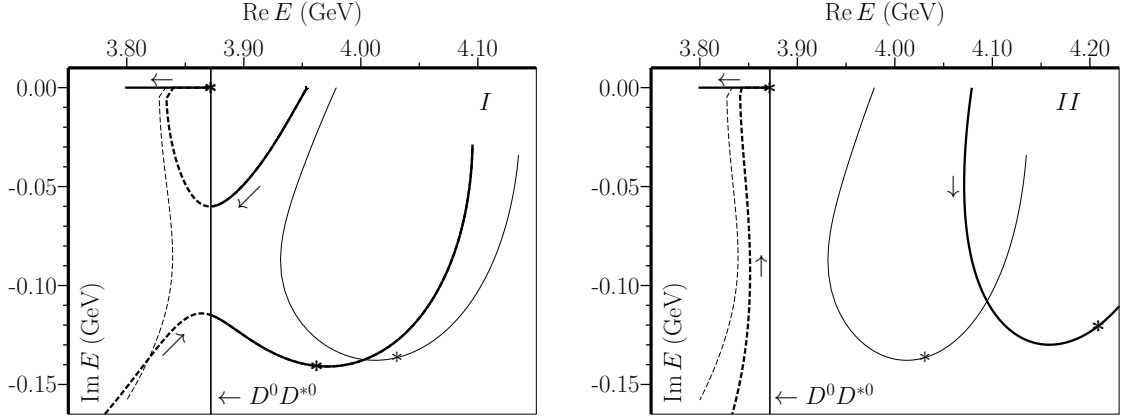


Figure 6.3: Trajectories of dynamical and confinement poles. The bold curves represent cases *I* (top graph) and *II* (bottom graph) defined in Table 6.7, and the others the standard case of Fig. 6.1; the solid (dashed) lines stand for normal (below-threshold) resonances. All trajectories lie on the second Riemann sheet. The pole positions for the g values in Table 6.7 are marked by *.

pole that moves steadily downwards and settles on the real axis below threshold, whereas the dynamical pole moves to higher energies and eventually approaches the real axis. So the poles interchange their roles when going from the standard case to case *I*. Nevertheless, the values of g needed to get a bound state at 3871.68 MeV are not very different in the two cases, viz. 1.172 vs. 1.034. Such a behavior was already observed almost a decade ago, namely for $D_{s0}^*(2317)$ [39] charmed-strange meson. In a first, two-channel model calculation [43] the $D_{s0}^*(2317)$ showed up as a dynamical resonance, settling below the S -wave DK threshold, whereas the 1^3P_0 $c\bar{s}$ state turned out to move to higher energies, with a large width, similarly to the standard $X(3872)$ case in Figs. 6.1 and 6.3 above. However, in a more complete, multichannel approach [46] the situations got reversed, just as in the present case *I*. Also in previous Chapter 5, with nine coupled channels, we reproduced the meson as a confinement pole. What appears to happen in the present case *I* is that shifting the bare 2^3P_1 state to somewhat lower energies is just enough to deflect the confinement pole to the left and not the right when approaching the continuum pole. Clearly, there will be an intermediate situation for which the left/right deflection will hinge upon only marginal changes in the parameters, but resulting in two completely different trajectories. Therefore, identifying one pole as dynamical and the other as linked to a confinement state is entirely arbitrary, the whole system being dynamical because of unquenching. At the end of the day, the only thing that really

counts is where the poles end up for the final parameters. The trajectories themselves are not observable and only serve as an illustration how a coupled-channel model as the one employed here mimics the physical situation. Suffice it to say that the lower pole, representing the $X(3872)$, is quite stable with respect to variations in the parameters, owing to its proximity to the only and most relevant OZI-allowed decay channel. The higher pole, on the other hand, should not be taken at face value, since a more realistic calculation should include other important decay channels, such as D^*D^* , with threshold just above 4 GeV.

Concerning the other scenario with changed parameters, labeled *II* in Table 6.7 and depicted in the lower graph of Fig. 6.3, we see that the trajectories do not change qualitatively when going from the standard case to *II*. There is a displacement of the right-hand branch, about 100 MeV to the right on average, in accordance with the same shift of the bare 2^3P_1 state. But the change in the lower, dynamical branch, is much less significant, though the value of g needed to produce a bound state at 3871-68 MeV now increases to 1.572 (see Table 6.7). We also notice from Fig. 6.3 that the two pole-trajectory branches hardly move towards one another, signaling less attraction between the poles due to a larger initial separation.

Inspecting again Table 6.7 as for the $c\bar{c}$ probability in cases *I* and *II* compared to the standard situation, we observe an increased value for case *I* and a decreased one for *II*. This is logical, since in case *I* the bare 2^3P_1 state lies closer to the $X(3872)$, whereas in case *II* it lies farther away. Nevertheless, the difference in $c\bar{c}$ probability between *I* and *II* is only about 3%, i.e., less than the variation with a in the standard case. These comparisons lend further support to the stability of our results.

Finally, in Fig. 6.4 we compare the wave function for case *II* with the standard one. We see there is no visible change in the R_f component. As for R_c , the first maximum gets somewhat reduced, but the secondary, negative bump even becomes a bit larger, owing to an inward shift of the node, lying now at about 3 GeV^{-1} . Yet, also in case *II* the $c\bar{c}$ component is still very significant, despite the large separation of more than 200 MeV between the $X(3872)$ bound state and the bare 2^3P_1 state. From the latter and all previous results we may safely conclude that the $c\bar{c}$ component of the $X(3872)$ wave function remains nonnegligible in a variety of scenarios, being even of comparable size as the D^0D^{*0} component in the inner region, save at very short distances.

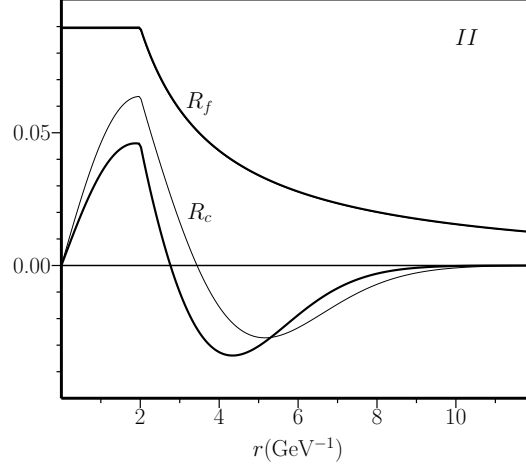


Figure 6.4: Normalized two-component radial wave function $R(r)$, for cases II and "standard", corresponding to parameters in Table 6.7. Bold curves refer to case II , normal curve to R_c for standard case. Note: R_f is indistinguishable within graphical accuracy for the two cases.

6.6 Summary and conclusions

In the present chapter, we have employed a simple and solvable Schrödinger model to study the wave function of the $X(3872)$ meson, by treating it as a coupled $c\bar{c}-D^0D^{*0}$ system with $J^{PC} = 1^{++}$ quantum numbers. Transitions between the two channels are described with the 3P_0 mechanism, through string breaking at a sharp distance a . The exact solutions to the equations allow us to easily study the trajectories of \mathcal{S} -matrix poles as a function of the decay coupling constant g . Thus, a dynamical pole is found, becoming a bound state just below the D^0D^{*0} threshold, for different string-breaking distances a , and an appropriate coupling g . On the other hand, the pole arising from the bare 2^3P_1 confinement state moves to higher energies and acquires a large imaginary part. However, the latter pole may not be very relevant physically, because of neglected additional meson-meson channels which will become important in that energy region.

As for the $X(3872)$ radial wave function, the $c\bar{c}$ component R_c turns out to be of significant size as compared to the D^0D^{*0} component R_f , especially for intermediate r values. Moreover, even for other trial BEs, the global shape of R_c and its relative magnitude vis-à-vis R_f in the central region is remarkably stable. But the corresponding $c\bar{c}$ probability is relatively low, due to the very long tail of the D^0D^{*0} wave function at small binding. These results are along the lines of the analysis based

on general arguments presented in Ref. [135]. Quantitatively, for the average [39] $X(3872)$ binding of 0.16 MeV, a $c\bar{c}$ probability of 7.5–11.2% is found, for a in the range 0.4–0.6 fm, which is compatible with other recent approaches [133, 134]. The corresponding r.m.s. radius turns out to be quite stable at about 7.8 fm, for the latter range of a values, while the S -wave scattering length of 11.6 fm, for $a \approx 0.4$ fm, is in agreement with expectations for a BE of 0.16 MeV.

Finally, we have studied the nature of the \mathcal{S} -matrix pole giving rise to $X(3872)$, by varying some of the otherwise fixed parameters. Thus, a drastic modification of pole trajectories is observed, for relatively small parameter variations, making the $X(3872)$ pole transform from a dynamical pole into one directly connected to the 2^3P_1 bare confinement state. However, the corresponding changes in the $c\bar{c}$ probability and r.m.s. radius, as well as the coupling g needed to reproduce $X(3872)$, are quite modest.

In conclusion, we should revisit the claims about $X(3872)$ made in Ref. [116], quoted in the Introduction above, namely about the inevitability of $X(3872)$ being a charm-meson molecule or virtual state, independently of the mechanism generating the state. Now, it is true that our analysis has confirmed some of the quantitative predictions in Ref. [116], viz. concerning the vanishing probability of wave-function components other than $D^0 D^{*0}$ as the BE approaches zero, and the related behavior of the $D^0 D^{*0}$ scattering length. However, we have also shown that the $c\bar{c}$ component is certainly not negligible and quite stable, in a variety of scenarios. Especially in electromagnetic processes, the prominence of this component for relatively small as well as intermediate r values will no doubt result in a significant contribution to the amplitudes. Moreover, as already mentioned above, the very unquenching of a 2^3P_1 $c\bar{c}$ state will not only introduce meson-meson components into the wave function, but also a contribution of the 1^3P_1 $c\bar{c}$ state, which can change predictions of electromagnetic transition rates very considerably [132]. We intend to study such processes for $X(3872)$ in future work, on the basis of a model as the one used in the present paper, by employing the formalism developed and successfully applied in Ref. [136]. However, in a detailed and predictive calculation of electromagnetic $X(3872)$ decays, the inclusion of the charged $D^\pm D^{*\mp}$ channel will be indispensable [137].

For all these reasons, we do not consider $X(3872)$ a charm-meson molecule, but rather a very strongly unitarized charmonium state. As a matter of fact, we do not believe *any* non-exotic mesonic resonance — whatever its origin — qualifies as a true meson-meson molecule, simply because such a state will inexorably mix

with the nearest $q\bar{q}$ states having the same quantum numbers. Indeed, we have demonstrated above that, even with a bare $c\bar{c}$ state 200 MeV higher in mass, the resulting $c\bar{c}$ component in the wave function is still appreciable. So let us conclude this discussion by quoting and fully endorsing the following statement from Ref. [116]:

“Any model of the $X(3872)$ that does not take into account its strong coupling to charm meson scattering states should not be taken seriously.”

Summary and Conclusions

The RSE coupled-channel model defined in Sec. 2.2 was applied to three different meson sectors, namely the isoscalar vector ϕ , the axial-vectors - pseudovectors with open-charm D_1 and D_{s1} , and the charmonium-like axial-vector $X(3872)$. A harmonic-oscillator (HO) confining potential was used with fixed parameters for frequency and constituent quark masses (c.q.m.), Eq. (2.32), values defined in Ref. [47]. The frequency of 190 MeV has been used in all RSE applications, and the c.q.m. are in agreement with other spectroscopy models. Only two free parameters are left, the dimensionless global coupling λ and the “string-breaking” distance a . For the present RSE applications their range is between 2 and 4 GeV^{-1} , and between 1.2 and 4, respectively for a and λ . We see these values are pretty close, considering a likely c.q.m. dependence of the parameters, as well as the set of included decay channels.

This work may shed light on the excited $J^{PC} = 1^{--}$ ϕ states and on the classification of the $\phi(2170)$ resonance, originally denoted $X(2175)$. Among the model’s S -matrix poles, there are good candidates for observed resonances, as well as other ones that should exist according to the quark model. Besides the expected resonances as unitarized confinement states, a dynamical resonance pole is found at $(2186 - i246)$ MeV. The huge width makes its interpretation as the $\phi(2170)$ somewhat dubious. On the other hand, the calculated resonances originating in the confinement spectrum are generally too narrow. We consider the inclusion of sharp thresholds only as the main problem of our description. Including the widths of final-state resonances could probably *increase* the widths of the now too narrow excited ϕ resonances stemming from the confinement spectrum. Since a simple substitution of the here used real masses by the true complex masses destroys the manifest unitarity of the S -matrix, to account for the nonvanishing widths of mesons in the coupled channels is a very difficult problem. The formalism described in Subsec. 2.2.1 was developed *a posteriori* and has not been applied to the ϕ vectors.

We dynamically reproduced the whole pattern of masses and widths of the axial-vector - pseudovector charmed mesons, by coupling the most important open and closed two-meson channels to bare $J^P = 1^+ c\bar{n}$ and $c\bar{s}$ states containing both 3P_1 and 1P_1 components. The coupling to two-meson channels dynamically mixes and lifts the mass degeneracy of the spectroscopic 3P_1 and 1P_1 states, as an alternative to the usual spin-orbit splitting. Of the two resulting S -matrix poles in either case, one stays very close to the energy of the bare state, as a quasi-bound state in the continuum, whereas the other shifts considerably. This is in agreement with the experimental observation that the $D_1(2420)$ and $D_{s1}(2536)$ have much smaller widths than one would naively expect. Predictions for pole positions of radially excited axial-vector charmed mesons are presented.

The nature of the $X(3872)$ enhancement was analyzed in the framework of the RSE, by studying it as a regular $J^{PC} = 1^{++}$ charmonium state, though strongly influenced and shifted by open-charm decay channels. The observed but OZI-suppressed $\rho^0 J/\psi$ and $\omega J/\psi$ channels were coupled as well, but effectively smeared out by using complex ρ^0 and ω masses, in order to account for their physical widths, followed by a rigorous algebraic procedure to restore unitarity. A very delicate interplay between the $D^0 D^{*0}$, $\rho^0 J/\psi$, and $\omega J/\psi$ channels was observed. The data clearly suggest that the $X(3872)$ is a very narrow axial-vector $c\bar{c}$ resonance, with a pole at or slightly below the $D^0 D^{*0}$ threshold.

A solvable coordinate-space model was employed to study the $c\bar{c}$ component of the $X(3872)$ wave function, by coupling a confined $^3P_1 c\bar{c}$ state to the almost unbound S -wave $D^0 \bar{D}^{*0}$ channel via the 3P_0 mechanism. The two-component wave function was calculated for different values of the binding energy and the transition radius a , always resulting in a significant $c\bar{c}$ component. However, the long tail of the $D^0 \bar{D}^{*0}$ wave function, in the case of small binding, strongly limits the $c\bar{c}$ probability, which roughly lies in the range 7–11%, for the average experimental binding energy of 0.16 MeV and a between 2 and 3 GeV⁻¹. Furthermore, a reasonable value of 7.8 fm was obtained for the $X(3872)$ r.m.s. radius at the latter binding energy, as well as an S -wave $D^0 \bar{D}^{*0}$ scattering length of 11.6 fm. Finally, the S -matrix pole trajectories as a function of coupling constant show that $X(3872)$ can be generated either as a dynamical pole or as one connected to the bare $c\bar{c}$ confinement spectrum, depending on details of the model. From these results we conclude that $X(3872)$ is not a genuine meson-meson molecule, nor actually any other mesonic system with non-exotic quantum numbers, due to inevitable mixing with the corresponding quark-antiquark states.

All the studied resonances are controversial, with $X(2175)$, alias $\phi(2170)$, and $X(3872)$ often thought to be exotics, while the open-charm axials exhibit an unexpected pattern of masses and widths. Within the unquenched and unitarized RSE model we are able to reproduce all the main features of these resonances as observed in experiments. Furthermore, we have shown, with a simplified Schrödinger model, the importance of a charmonium component in $X(3872)$. The relevance of “dressing” the bare states is well known in spectroscopy, and so we consider the $X(3872)$ is indeed the $\chi_{c1}(2P)$ resonance, strongly influenced by the $D^0 D^{*0}$ threshold, and strongly deviated from its bare energy due to the unquenching.

∴

Future research work following the present thesis will include the development of unquenched models, such as the RSE but not only, to approach enigmatic resonances. In particular, we plan to clarify the nature of mesonic structures observed in experimental data, and help to disentangle peaks from resonance poles and nonresonant enhancements due to threshold openings. Also, we aim to distinguish between intrinsic resonances, directly linked to a confinement spectrum, and dynamically generated ones. Another goal is the development of a unitarization scheme for quenched tetraquark states. At last, the ultimate purpose of meson spectroscopy is to understand confinement and decay mechanisms, i.e., the strong interaction itself.

Bibliography

- [1] Hideki Yukawa, *Proc. Phys. Math. Soc. Jpn.* **17**, 48 (1935).
- [2] Homi J. Bhabha, *Nature* **141**, 117 (1938).
- [3] G. P. S. Occhialini and C. F. Powell, *Nature* **159**, 186 (1947).
- [4] C. M. G. Lattes, G. P. S. Occhialini and C. F. Powell, *Nature* **160**, 453 (1947).
- [5] M. Gell-Mann, Caltech Report CTSL-20.
- [6] Y. Ne'eman, *Nuc. Phys.* **26**, 222 (1961).
- [7] E. Abers, C. Zemach, *Phys. Rev.* **132**, 1831 (1963).
- [8] M. Gell-Mann, *Phys. Lett.* **8**, 214 (1964).
- [9] G. Zweig, CERN-TH-401, CERN-TH-412.
- [10] E. D. Bloom *et al.*, *Phys. Rev. Lett.* **23**, 930 (1969); M. Breidenbach *et al.*, *Phys. Rev. Lett.* **23**, 935 (1969).
- [11] J. D. Bjorken and E. A. Paschos, *Phys. Rev.* **185**, 1975 (1969); Sidney D. Drell, Donald J. Levy, and Tung-Mow Yan, *Phys. Rev. Lett.* **22**, 744 (1969).
- [12] Aubert *et al.*, *Phys. Rev. Lett.* **33**, 1404 (1974); Augustin *et al.*, *Phys. Rev. Lett.* **33**, 1406 (1974).
- [13] David J. Gross, Frank Wilczek, *Phys. Rev. D* **8**, 3633 (1973).
- [14] H. Fritzsch, M. Gell-Mann, H. Leutwyler, *Phys. Lett. B* **47**, 365 (1973); D. J. Gross and F. Wilczek, *Phys. Rev. D* **9**, 980 (1974); S. Weinberg *Phys. Rev. Lett.* **31**, 494 (1973).
- [15] S. Okubo, *Phys. Lett.* **5**, 165 (1963); J. Iizuka, *Prog. Theor. Phys. Supp.* **37**, 21 (1966).
- [16] Henry P. Stapp, *Rev. Mod. Phys.* **34**, 390 (1962).
- [17] Geoffrey F. Chew, *Rev. Mod. Phys.* **34**, 394 (1962); Geoffrey F. Chew and Steven C. Frautschi *Phys. Rev.* **124**, 264 (1961); F. G. Chew and S. C. Frautschi, *Phys. Rev. Lett.* **7**, 394 (1961).
- [18] John A. Wheeler, *Phys. Rev.* **52**, 1107 (1937).

- [19] T. Regge, *Il Nuov. Cim.* **14**, 951 (1959), **18**, 947 (1960).
- [20] Geoffrey F. Chew, *S-Matrix Theory of Strong Interactions*, W. A. Benjamin, inc., 1961.
- [21] S. Godfrey and N. Isgur, *Phys. Rev. D* **32**, 189 (1985).
- [22] S. Capstick *et al.*, *Eur. Phys. J. A* **35**, 253 (2008).
- [23] Dmitri Antonov, *Nonperturbative methods in gauge theories*, PISA University Press, 2013.
- [24] Y. Nambu, G. Jona-Lasinio, *Phys. Rev.* **122**, 345 (1961); **124**, 246 (1961).
- [25] M. Gell-Mann, M. Lévy, *Nuov. Cim.* **16**, 705 (1960).
- [26] R. Delbourgo and M. D. Scadron, *Mod. Phys. Lett. A* **10**, 251 (1995); R. Delbourgo and M. D. Scadron, *Jour. Mod. Phys. A* **13**, 657 (1998); M. D. Scadron, G. Rupp, and R. Delbourgo, *Fortschr. Phys.* **61**, 994 (2013).
- [27] P. J. A. Bicudo and J. E. F. T. Ribeiro *Phys. Rev. D* **42**, 1611 (1990); 1625 (1990); 1635 (1990); R. F. Wagenbrunn and L. Ya. Glozman, *Phys. Rev. D* **75**, 036007 (2007); A. P. Szczepaniak, E. S. Swanson, *Phys. Rev. Lett.* **87**, 072001 (2001).
- [28] Stephen L. Adler, *Phys. Rev.* **137**, B1 B1022 (1965); **139**, B1638 (1965).
- [29] V. Elias, M. Tong, M. D. Scadron, *Phys. Rev. D* **40**, 3670 (1989).
- [30] S. Godfrey and J. Napolitano, *Rev. Mod. Phys.* **71**, 1411 (1999).
- [31] A. Le Yaouanc, L. Olivier, O. Pène, and J.-C. Raynal, *Phys. Rev. D* **8**, 2223 (1973); *Phys. Rev. D* **9**, 1415 (1974); *Phys. Rev. D* **11**, 1272 (1975).
- [32] Paul Geiger, Eric S. Swanson, *Phys. Rev. D* **50**, 6855 (1994).
- [33] N. Isgur and H. B. Thacker, *Phys. Rev. D* **64**, 094507 (2001).
- [34] G. Breit and E. Wigner, *Phys. Rev.* **49**, 519 (1936).
- [35] M. Ablikim *et al.*, arXiv:0807.0494v1 [hep-ex].
- [36] S. Ceci, M. Korolija, and B. Zauner, *Phys. Rev. Lett.* **111**, 112004 (2013).
- [37] D. V. Bugg, *J. Phys. G: Nucl. Part. Phys.* **37**, 055002 (2010); *J. Phys. G: Nucl. Part. Phys.* **35**, 075005 (2008).
- [38] E. van Beveren, G. Rupp, and J. Segovia, *Phys. Rev. Lett.* **105**, 102001 (2010).
- [39] J. Beringer *et al.* (Particle Data Group), *Phys. Rev. D* **86**, 010001 (2012).
- [40] D. V. Bugg, *Phys. Rep.* **397**, 257 (2004).
- [41] E. van Beveren and G. Rupp, *Annals Phys.* **324**, 1620 (2009).
- [42] E. van Beveren and G. Rupp, *Int. J. Theor. Phys. Group Theor. Nonlin. Opt.* **11**, 179 (2006).

- [43] E. van Beveren and G. Rupp, *Phys. Rev. Lett.* **91**, 012003 (2003)
- [44] E. van Beveren, D. V. Bugg, F. Kleefeld, and G. Rupp, *Phys. Lett. B* **641**, 265 (2006)
- [45] E. van Beveren and G. Rupp, *Eur. Phys. J. A* **31**, 468 (2007)
- [46] E. van Beveren and G. Rupp, *Phys. Rev. Lett.* **97**, 202001 (2006)
- [47] E. van Beveren, G. Rupp, T. A. Rijken and C. Dullemond, *Phys. Rev. D* **27**, 1527 (1983).
- [48] E. van Beveren, *Z. Phys. J. C* **21** 291 (1984); **17** 135 (1983).
- [49] E. van Beveren, G. Rupp, *Eur. Phys. C* **11** 717 (1999).
- [50] T. Takagi, *Japan J. Math.* **1**, 82 (1924)
- [51] E. van Beveren, C. Dullemond, and T.A. Rijken, *Z. Phys. C* **19**, 275 (1983) 275.
- [52] Bateman Manuscript Project, *Higher Transcendental Functions*, edited by A. Erdelyi *et al.*, (McGraw-Hill, New York, 1953), Vol. 1, Chap. VI
- [53] M. Abramowitz, I. A. Stegun, editors, *Handbook of mathematical functions, with formulas, graphs, and mathematical tables*, (Dover, New York, 1970), ninth printing, Chap. 6
- [54] B. Aubert *et al.* [BABAR Collaboration], *Phys. Rev. D* **74** (2006) 091103.
- [55] M. Ablikim *et al.* [BES Collaboration], *Phys. Rev. Lett.* **100** (2008) 102003.
- [56] C. P. Shen *et al.* [Belle Collaboration], *Phys. Rev. D* **80**, 031101(R) (2009).
- [57] G. J. Ding and M. L. Yan, *Phys. Lett. B* **650**, 390 (2007)
- [58] G. J. Ding and M. L. Yan, *Phys. Lett. B* **657**, 49 (2007)
- [59] Z. G. Wang, *Nucl. Phys. A* **791**, 106 (2007)
- [60] H. X. Chen, X. Liu, A. Hosaka, and S. L. Zhu, *Phys. Rev. D* **78**, 034012 (2008)
- [61] M. Napsuciale, E. Oset, K. Sasaki, and C. A. Vaquera-Araujo, *Phys. Rev. D* **76**, 074012 (2007)
- [62] A. Martinez Torres, K. P. Khemchandani, L. S. Geng, M. Napsuciale, and E. Oset, *Phys. Rev. D* **78**, 074031 (2008)
- [63] S. L. Zhu, *Int. J. Mod. Phys. E* **17**, 283 (2008) [arXiv:hep-ph/0703225].
- [64] G. Rupp, S. Coito, and E. van Beveren, *Acta Phys. Polon. Suppl.* **2**, 437 (2009).
- [65] C. Amsler *et al.* [Particle Data Group], *Phys. Lett. B* **667**, 1 (2008).
- [66] R. Delbourgo and M. D. Scadron, *Int. J. Mod. Phys. A* **13**, 657 (1998)
- [67] Yu. S. Surovtsev and P. Bydzovsky, *Nucl. Phys. A* **807**, 145 (2008).

- [68] N. N. Achasov and A. A. Kozhevnikov, *Phys. Rev. D* **57**, 4334 (1998) [*Phys. Atom. Nucl.* **60**, 2029 (1998 YAFIA,60,2212-2223.1998)]
- [69] R. R. Akhmetshin *et al.*, *Phys. Lett. B* **551**, 27 (2003).
- [70] E. van Beveren, C. Dullemond, and G. Rupp, *Phys. Rev. D* **21**, 772 (1980) [Erratum-ibid. **22**, 787 (1980)].
- [71] E. van Beveren and G. Rupp, *Annals Phys.* **323**, 1215 (2008).
- [72] H. Abramowicz *et al.* (ZEUS collaboration), *Nuc. Phys. B* **866**, 229 (2013).
- [73] D. Besson *et al.* [CLEO Collaboration], *Phys. Rev. D* **68**, 032002 (2003) [Erratum-ibid. **75**, 119908 (2007)].
- [74] K. Abe *et al.* [Belle Collaboration], *Phys. Rev. D* **69**, 112002 (2004).
- [75] M. Di Pierro and E. Eichten, *Phys. Rev. D* **64**, 114004 (2001).
- [76] W. A. Bardeen, E. J. Eichten, and C. T. Hill, *Phys. Rev. D* **68**, 054024 (2003).
- [77] D. Becirevic, S. Fajfer, and S. Prelovsek, *Phys. Lett. B* **599**, 55 (2004).
- [78] P. Colangelo, F. De Fazio, and R. Ferrandes, *Mod. Phys. Lett. A* **19**, 2083 (2004).
- [79] T. Mehen and R. P. Springer, *Phys. Rev. D* **72**, 034006 (2005).
- [80] K. Nakamura *et al.* (Particle Data Group), *J. Phys. G* **37**, 075021 (2010)
- [81] D. Gamermann and E. Oset, *Eur. Phys. J. A* **33**, 119 (2007).
- [82] F. K. Guo, P. N. Shen, and H. C. Chiang, *Phys. Lett. B* **647**, 133 (2007).
- [83] A. M. Badalian, Yu. A. Simonov, and M. A. Trusov, *Phys. Rev. D* **77**, 074017 (2008).
- [84] E. van Beveren and G. Rupp, *Eur. Phys. J. C* **32**, 493 (2004).
- [85] B. Aubert *et al.* [BABAR Collaboration], *Phys. Rev. D* **80**, 092003 (2009).
- [86] E. van Beveren and G. Rupp, *Phys. Rev. D* **81**, 118101 (2010).
- [87] Z. Y. Zhou and Z. Xiao, *Phys. Rev. D* **84**, 034023 (2011).
- [88] G. Rupp, F. Kleefeld, and E. van Beveren, *AIP Conf. Proc.* **756**, 360 (2005).
- [89] K. P. Khemchandani, E. van Beveren, and G. Rupp, *Prog. Theor. Phys.* **125**, 581 (2011).
- [90] S. K. Choi *et al.* (Belle collaboration), *Phys. Rev. Lett.* **91**, 262001 (2003).
- [91] D. E. Acosta *et al.* (CDF II collaboration), *Phys. Rev. Lett.* **93**, 072001 (2004).
- [92] V. M. Abazov *et al.* (D0 collaboration), *Phys. Rev. Lett.* **93**, 162002 (2004).

- [93] B. Aubert *et al.* (BABAR collaboration), *Phys. Rev. D* **71**, 071103(R) (2005); **73**, 011101(R) (2006); **77**, 111101(R) (2008).
- [94] A. Abulencia *et al.* (CDF collaboration), *Phys. Rev. Lett.* **96**, 102002 (2006)
- [95] G. Gokhroo *et al.* (Belle collaboration), *Phys. Rev. Lett.* **97**, 162002 (2006)
- [96] B. Aubert *et al.* (BABAR collaboration), *Phys. Rev. D* **77**, 011102(R) (2008)
- [97] T. Aaltonen *et al.* (CDF collaboration), *Phys. Rev. Lett.* **103**, 152001 (2009).
- [98] P. del Amo Sanchez *et al.* (BABAR collaboration), *Phys. Rev. D* **82**, 011101(R) (2010).
- [99] K. Abe *et al.* (Belle collaboration), BELLE-CONF-0540, arXiv:hep-ex/0505037
- [100] R. Aaij *et al.* (LHCb collaboration), *Phys. Rev. Lett.* **110**, 22201 (2013).
- [101] N. A. Tornqvist, *Z. Phys. C* **61**, 525 (1994)
- [102] M. B. Voloshin, *Phys. Lett. B* **579**, 316 (2004);
M. T. AlFiky, F. Gabbiani, A. A. Petrov, *Phys. Lett. B* **640**, 238 (2006);
M. Suzuki, *Phys. Rev. D* **72**, 114013 (2005);
S. Fleming, M. Kusunoki, T. Mehen, U. van Kolck, *Phys. Rev. D* **76**, 034006 (2007);
Y. R. Liu, X. Liu, W. Z. Deng, S. L. Zhu, *Eur. Phys. J. C* **56**, 63 (2008);
C. E. Thomas, F. E. Close, *Phys. Rev. D* **78**, 034007 (2008);
C. Bignamini, B. Grinstein, F. Piccinini, A. D. Polosa, C. Sabelli, *Phys. Rev. Lett.* **103**, 162001 (2009);
R. D. Matheus, F. S. Navarra, M. Nielsen, C. M. Zanetti, *Phys. Rev. D* **80**, 056002 (2009);
I. W. Lee, A. Faessler, T. Gutsche, V. E. Lyubovitskij, *Phys. Rev. D* **80**, 094005 (2009);
B. K. Wang, W. Z. Deng, X. L. Chen, arXiv:0910.4787 [hep-ph];
P. G. Ortega, J. Segovia, D. R. Entem, F. Fernandez, *Phys. Rev. D* **81**, 054023 (2010).
- [103] E. S. Swanson, *Phys. Rept.* **429**, 243 (2006)
- [104] E. Klempt, A. Zaitsev, *Phys. Rept.* **454**, 1 (2007)
- [105] B. A. Li, *Phys. Lett. B* **605**, 306 (2005);
L. Maiani, F. Piccinini, A. D. Polosa, V. Riquer, *Phys. Rev. D* **71**, 014028 (2005);
R. D. Matheus, S. Narison, M. Nielsen, J. M. Richard, *Phys. Rev. D* **75**, 014005 (2007);
K. Terasaki, *Prog. Theor. Phys.* **122**, 1285 (2010);
S. Dubnicka, A. Z. Dubnickova, M. A. Ivanov, J. G. Korner, *Phys. Rev. D* **81**, 114007 (2010);
M. Karliner, H. J. Lipkin, arXiv:1008.0203 [hep-ph].
- [106] D. V. Bugg, *Phys. Rev. D* **71**, 016006 (2005); *J. Phys. G* **35**, 075005 (2008); arXiv:1101.1659 [hep-ph].
- [107] Yu. S. Kalashnikova, A. V. Nefediev, *Phys. Rev. D* **80**, 074004 (2009)

- [108] I. V. Danilkin, Yu. A. Simonov, *Phys. Rev. Lett.* **105**, 102002 (2010); *Phys. Rev. D* **81**, 074027 (2010)
- [109] Y. Jia, W. L. Sang, J. Xu, arXiv:1007.4541 [hep-ph].
- [110] Y. Dong, A. Faessler, T. Gutsche, S. Kovalenko, V. E. Lyubovitskij, *Phys. Rev. D* **79**, 094013 (2009)
- [111] C. Yang, B. F. Li, X. L. Chen, W. Z. Deng, *Chin. Phys. C* **35**, 797 (2011). arXiv:1011.6124 [hep-ph]
- [112] S. Coito, G. Rupp, E. van Beveren, *Acta Phys. Polon. Supp.* **3**, 983 (2010).
- [113] C. Hanhart, Yu. S. Kalashnikova, A. E. Kudryavtsev, A. V. Nefediev, *Phys. Rev. D* **76**, 034007 (2007).
- [114] J. Gegelia, S. Scherer, *Eur. Phys. J. A* **44**, 425 (2010).
- [115] R. E. Cutkosky, P. V. Landshoff, D. I. Olive, J. C. Polkinghorne, *Nucl. Phys. B* **12**, 281 (1969).
- [116] E. Braaten, M. Lu, *Phys. Rev. D* **76**, 094028 (2007); C. Hanhart, Yu. S. Kalashnikova, A. V. Nefediev, *Phys. Rev. D* **81**, 094028 (2010).
- [117] T. Aushev *et al.* (Belle collaboration), *Phys. Rev. D* **81**, 031103 (2010);
- [118] E. van Beveren, G. Rupp, J. Segovia, *Phys. Rev. Lett.* **105**, 102001 (2010).
- [119] D. Gamermann, E. Oset, *Phys. Rev. D* **80**, 014003 (2009.)
- [120] E. van Beveren, J. E. G. Costa, F. Kleefeld, G. Rupp, *Phys. Rev. D* **74**, 037501 (2006).
- [121] B. Aubert *et al.* (BaBar collaboration), *Phys. Rev. D* **71**, 031501 (2005).
- [122] Y. Fan, J. -Z. Li, C. Meng, K. -T. Chao, *Phys. Rev. D* **85**, 034032 (2012).
- [123] T. Wang, G. -L. Wang, Y. Jiang, W. -L. Ju, arXiv:1205.5725 [hep-ph].
- [124] C. -Y. Cui, Y. -L. Liu, G. -B. Zhang, M. -Q. Huang, *Commun. Theor. Phys.* **57**, 1033 (2012).
- [125] N. A. Tornqvist, *Phys. Lett. B* **590**, 209 (2004); *Z. Phys. C* **61**, 525 (1994); *Phys. Rev. Lett.* **67**, 556 (1991).
- [126] K. K. Seth, *Prog. Part. Nucl. Phys.* **67**, 390 (2012).
- [127] E. Braaten, M. Kusunoki, *Phys. Rev. D* **69**, 074005 (2004).
- [128] A. M. Badalian, V. D. Orlovsky, Y. A. Simonov, arXiv:1210.4674 [hep-ph].
- [129] E. van Beveren, G. Rupp, arXiv:0712.1771 [hep-ph].
- [130] G. S. Bali *et al.* (SESAM Collaboration), *Phys. Rev. D* **71**, 114513 (2005).

- [131] E. van Beveren, T. A. Rijken, K. Metzger, C. Dullemond, G. Rupp, J. E. Ribeiro, *Z. Phys. C* **30**, 615 (1986).
- [132] A. M. Badalian, V. D. Orlovsky, Y. .A. Simonov, B. L. G. Bakker, *Phys. Rev. D* **85**, 114002 (2012).
- [133] P. G. Ortega, J. Segovia, D. R. Entem, F. Fernandez, *Phys. Rev. D* **81**, 054023 (2010).
- [134] M. Takizawa, S. Takeuchi, *Prog. Theor. Exp. Phys.* **2013**, 093D01. arXiv:1206.4877 [hep-ph].
- [135] M. B. Voloshin, *Prog. Part. Nucl. Phys.* **61**, 455 (2008).
- [136] A. G. M. Verschuren, C. Dullemond, E. van Beveren, *Phys. Rev. D* **44**, 2803 (1991).
- [137] D. Gamermann, J. Nieves, E. Oset, E. Ruiz Arriola, *Phys. Rev. D* **81**, 014029 (2010);
F. Aceti, R. Molina, E. Oset, *Phys. Rev. D* **86**, 113007 (2012).